UNIVERSITÀ DEGLI STUDI DI TRIESTE

XXXII CICLO DEL DOTTORATO DI RICERCA IN EARTH SCIENCE AND FLUID MECHANICS

MODELLING AND APPLICATION OF MITRAL VALVE DYNAMICS FOR REPRODUCING THE FLOW IN THE LEFT VENTRICLE OF THE HUMAN HEART

Settore scientifico-disciplinare: ING-IND/34

Ph.D. Student
DARIO COLLIA

Ph.D. Program Coordinator
PROF. PIERPAOLO OMARI

Thesis Supervisor
PROF. GIANNI PEDRIZZETTI

Academic Year 2018/2019

Endings are never easy;
I always build them up so much in my head they can't possibly live up to my expectations, and I just end up disappointed.
I'm not even sure why it matters to me so much how things end here...
I guess it's because we all want to believe that what we do is very important, that people hang onto our every word, that they care what we think.
The truth is: you should consider yourself lucky if you even occasionally get to make someone, anyone, feel a little better.
After that it's all about the people that you let into your life.
And as my mind drifted to faces I've seen here before, I was taken to memories of family, of coworkers, of lost loves, even of those who've left us.
And as I rounded that corner, they all came at me in a wave of shared experience...
And even though it felt warm and safe, I knew it had to end.
It's never good to live in the past too long.
As for the future, thanks to Giusy, it didn't seem so scary anymore.
It could be whatever I wanted it to be...

[Scrubs]

List of publications

(1) D. Collia, M. Vukicevic, V. Meschini, L. Zovatto & G. Pedrizzetti.
Simplified mitral valve modelling for prospective clinical application of left ventricular fluid dynamics. *Journal of Computational Physics,2019, 398:108895.* doi:10.1016/j.jcp.2019.108895.

(2) D. Collia, L. Zovatto & G. Pedrizzetti.
Analysis of Mitral Valve Regurgitation by Computational Fluid Dynamics left ventricular fluid dynamics. *APL Bioengineering, 2019, 3:036105.* doi:10.1063/1.5097245. *(Editor's Pick, Featured, Scilight)*

(3) C. Celotto, L. Zovatto, D. Collia, & G. Pedrizzetti.
Influence of mitral valve elasticity on flow development in the left ventricle. *Eur. J. Mech. B/Fluids, 2019, 75:110-118.*
doi:10.1016/j.euromechflu.2018.11.018.

(4) M. Dal Ferro, V. De Paris, D. Collia, D. Stolfo, T. Caiffa, G. Brabati, R. Korcova, B. Pinamonti, L. Zovatto, M. Zecchin, G. Sinagra & G. Pedrizzetti.
Left Ventricular Response to Cardiac Resynchronization Therapy: Insights From Hemodynamic Forces Computed by Speckle Tracking.
Frontiers in Cardiovascular Medicine, 2019, 6:59.
doi: 10.3389/fcvm.2019.00059.

(5) M. Dal Ferro, D. Stolfo, V. De Paris, P. Lesizza, R. korcova, D. Collia, G. Tonti, G. Sinagra & G. Pedrizzetti.
Cardiac fluid dynamics meets deformation imaging. *Cardiovascular Ultrasound, 2018, 16:4.* doi 10.1186/s12947-018-0122-2

Abstract

The fluid dynamics in the left ventricle of the human heart is considered an important marker of long-term cardiovascular outcome. To this end, numerical simulations represent an important tool for integrating the existing cardiovascular medical imaging modalities and uncover physical flow phenomena. This study presents a computational method for the fluid dynamics inside the left ventricle, designed to be efficiently integrated in clinical scenarios. It includes an original model of the mitral valve dynamics, which describes an asymptotic behavior for tissues with no elastic stiffness other than the constrain of the geometry obtained from medical imaging; in particular, the model provides an asymptotic description without requiring details of tissue properties that may not be measurable in vivo. The advantages of this model with respect to a valveless orifice and its limitations with respect to a complete tissue modeling are verified. Its performance is then analysed in detail to ensure correct interpretation of the results. The proposed computational model represents a potential option when information about tissue mechanical properties is insufficient for the implementation of a full fluid-structure interaction approach. Geometries of the left ventricle (LV) and mitral valve (MV) are extracted from 4D-transesophageal echocardiography. MV geometries are extracted in open and closed configurations and the intraventricular fluid dynamics pattern is reproduced by a dedicated approach to direct numerical simulation (DNS) which includes flow-tissue interaction for the MV leaflet [23]. This approach is applied to both normal and pathologic ventricles, respectively, to investigate the dynamics of the MV during the cardiac cycle: how it interacts with the ventricular flow and how it affects clinical measurements. The dynamics of mitral leaflet opening at the onset of diastole, as well as closure at the transition between diastole and systole, is governed by the increased transmitral pressure gradient associated with the bulk cardiac flow. However, during flow diastasis in the middle of diastolic filling phase, mitral leaflet motion is primarily influenced by the intraventricular circulation which gives rise to an increased tendency to close the valve in dilated ventricles. This observation provides a physical interpretation to echocardiographic measurements commonly employed in the clinical diagnostic process. Our findings demonstrated the properties of false regurgitation, blood that did not cross the open MV orifice and returns into the atrium during the systolic retrograde motion of the MV leaflets, whose entity should be accounted when evaluating small regurgitation [24]. The regurgitating volume is found to be proportional to the effective orifice area, with the limited dependence of the LV geometry and type of prolapse. These affect the

percentage of old blood returning to the atrium which may be associated with thrombogenic risk. This non-invasive method is useful for the assessment of blood flow, to improve early detection of cardiac dysfunctions and for provide a concrete helpful in clinical routines.

Contents

1. Introduction

Fluid dynamics is gaining increasing attention in cardiology for the influence it may have on the long-term outcome of several cardiac dysfunctions [80, 87]. Numerous studies in literature reported how stresses due to the interaction between flow and tissue play a primary role in the development of embryonic hearts [4, 25, 55], and flow-mediated forces participate in the progression or regression of cardiac pathologies in adult hearts [38, 88]. Given its potential importance, it is foreseeable that measurements of intra-cardiac fluid dynamics will soon become an integral part of the clinical evaluation process. Recent advances in cardiovascular imaging permit, to some extent, measurement of cardiac fluid dynamics in vivo [76, 98]; especially in the left ventricle (LV), which represents the most energetic and clinically relevant cardiac chamber. However, the imaging technologies able to quantify blood flow, like Magnetic Resonance Imaging (MRI) and Echocardiography, present limitations in this respect and applications to clinical practice are still limited. Direct numerical simulation (DNS) of intraventricular fluid dynamics represents another possible approach to analyse cardiac flow in individual patients. DNS can be performed in LV geometries extracted from clinical images, such as Computed Tomography (CT), MRI or Echocardiography, to reproduce the flow under realistic conditions. Recent advances in DNS of cardiac fluid dynamics were mostly based on the immersed boundary method (IBM). That method was originally introduced from the 1970s [89, 91, 90], and underwent numerous developments and improvements since then [30, 71, 72]. In the IBM, the flow equations are resolved in a regular Cartesian grid with a distribution of fictitious forces concentrated at the immersed solid boundaries whose intensity is matched to ensure fulfilment of the boundary conditions. IBM is particularly well suited for integration with medical imaging because the extracted moving geometries are simply immersed inside the fluid domain without the need for specific mesh-generation procedures. It also allows a relatively straightforward management of closure and opening of the valves avoiding problems associated with extreme grid deformation or collapse. Recent reviews outlined the reliability of computational approaches to analyze LV fluid dynamics [73, 85]. An open challenge in LV flow simulations is represented by modeling the dynamics of the mitral valve (MV) that separates the left atrium from the LV and whose dynamics influences the flow inside the LV. The MV is a bi-leaflet valve with a longer anterior leaflet side (on the aortic side, separating inflow and outflow tracts) and a shorter one next to the posterior LV wall. The opening and closure motion of the asymmetric MV leaflets is mainly driven by the flow with a minimal elastic resistance from the loose tissue (under normal conditions)

other than the support of chordae tendineae that avoid retrograde leaflet displacement and ensure unidirectional flow. In the same vein, the dynamics of the MV leaflets influence vortex formation and the flow that develops inside the LV during filling phase (diastole), which indirectly affects several diagnostic markers used in clinical practice as the effective regurgitant orifice area (EROA), stroke volume (SV), regurgitated volume (V_{reg}) and more. In general, the knowledge of the relationship between MV dynamics and LV flow is very limited because the motion of the valvular leaflets excursion is too fast for the available time resolution properties of contemporary medical imaging modalities to allow direct evaluation. The complexity and lack of reliable in-vivo measurement also make simulations of MV dynamics difficult; indeed, most numerical studies of LV fluid dynamics are performed using orifice-like valves, with a fully-open/fully-closed behavior, and do not include the dynamics of valvular leaflets. Other models of MV dynamics, after the pioneering numerical studies in the 80's [91, 90], avoided dealing with the complexity of a real general fluid-structure interaction (FSI) and considered a prescribed motion for the leaflets with the main objective of verifying the differences with valveless orifices [7, 100]. Realistic FSI model are challenging and are becoming progressively feasible since recently; here, valve motion obeys the equation for the finite deformation of the elastic material under the action of a distribution of flow-driven pressure difference between the two sides of the leaflets [45, 70, 59, 63, 43, 109, 11]. Such a rigorous approach is best suited for prosthetic valves whose mechanical properties are known in detail; however, its application in a clinical context may fall short of the knowledge of the (visco-)elastic properties for the valvular tissues that are not easily quantifiable in-vivo. Indeed, the mitral leaflets present an inhomogeneous structure with variable thickness, made of a non-isotropic fibrous texture near the annulus which becomes looser and thinner closer to the leaflet's free edge [92, 18, 64]. In subject-specific clinical applications elastic properties are not directly measurable and imaging tools allow extracting the geometry of the mitral valve with moderate accuracy and limited to a few instances (typically fully-closed and fully-open configurations, that last somewhat longer). This limited availability of information is commonly overcome by using average geometric models and parameters that are representative of a population, an approach that can be appropriate when investigating properties common to pathological classes. On the other hand, in individual clinical applications and in the presence of subject-specific pathological conditions, it is necessary to develop relatively simple models that can best integrate the few available data for providing information that can be included in the clinical process. An asymptotic model for MV dynamics was previously introduced to reproduce the flow-driven motion of valvular leaflets

in the absence of elastic resistance [31]. That model was intrinsically limited to valvular dynamics described by one-degree-of-freedom and was evaluated in an idealized valvular geometry. The present study, inspired from that model, introduces an original mathematical framework that permits the assessment of MV dynamics described by an arbitrary number of degrees of freedom. In principle, the proposed approach may find application to additional specialty fields where the motion of structural elements is similarly driven by fluid flows in the asymptotic limit of negligible elastic or inertial effects. The internal forces are replaced by an intrinsic stiffness associated with the description in terms of a limited number of degrees of freedom. In the present application, this approach is integrated with imaging technology for the numerical solution of MV leaflets motion with geometry effectively obtained from individual recordings. Mitral valve prolapse (MVP) due to myxomatous leaflet degeneration is the most prevalent cause of the mitral regurgitation (MR) [78, 36]. To-date several markers are used routinely in clinical practice for the integrated evaluation of MR severity, including qualitative (i.e., colour flow jet area, flow convergence), semi-quantitative Doppler (i.e., vena contracta width) and quantitative Doppler (effective regurgitant orifice area, regurgitant volume and fraction) parameters [110]. The vena contracta method [105, 46] estimates the size of the regurgitant orifice by measuring the minimum diameter of the regurgitant flow jet distal to (or at) the plane of the anatomic regurgitant orifice; and while this direct relationship is relatively independent of flow rate and pressure gradient in less dynamic orifice areas (as in holosystolic MR), measurement errors may lead to overestimation when MR is limited to mid or late systole, or is biphasic (i.e., secondary MR) or transient (secondary MR, ventricular ectopy or delay). The Proximal Isosurface Velocity Area (PISA) method may overcome this limitation by evaluating the regurgitant volume instead, based on the 2D color-Doppler signal of the converging flow proximal to the anatomic orifice. The flow velocity is shown with different colors, and the assumption of hemispheric converging flow allows estimating the flow rate based on the value of one isovelocity contour. This method is the most utilized for its simplicity, but remains prone to error because the PISA area is not always hemispheric when the regurgitant orifice is non cicrcular,often, as with functional MR which may exhibit a crescent or elliptical shape; moreover, PISA calculation relies on instantaneous measures that are averaged to the cardiac cycle for a volumetric estimation (typically assuming a proportion with the velocity trace measured with Doppler at the LV outflow) [96]. In recent years, the increasing spread of 3D echocardiography and cardiac magnetic resonance (CMR) allows more accurate evaluations of MR. High quality phase-contrast CMR with velocity-encoded imaging is used for estimating the aortic flow

and calculates the absolute regurgitant volume from the volume rate difference in the left ventricle (LV). This approach is considered the most reliable although it calculates MR from a difference, rather than directly on the mitral valve (MV), presenting some degree of variability [76]. The effective orifice area (EOA) [35, 53, 57] represents a more anatomic marker of MR severity; this approach also presents various limitations partly imputable to the difficulty of measuring the EOA directly from images of the MV orifice (MVO). Although these methods provide surrogate markers for MR severity in the routine clinical environment, the description of the flow phenomena involved in MR remains unclear, further compounded by the wide variability in loading conditions, timing of MR and pathoanatomic stigmata of disease seen with different MR etiologies, indirectly impacting the flow dynamics associated with the MV despite similar degrees of MR severity and comparable EROA sizes. Through this study is possible to get deeper insight into the flow phenomena associated with MR. This is achieved by reproducing, using direct numerical simulation (DNS), the fluid dynamics in the LV in correspondence with pathologic MVPs obtained from clinical images. This approach allows estimating the cardiac fluid dynamics associated with different types and gravity of MVPs and how the actual regurgitant volume is correlated with EOA. The primary objective of this non-invasive method is to provide a novel, sensitive and reproducible marker of subtle, subclinical myocardial dysfunction particularly in asymptomatic patients without class-I indications of surgical intervention, that is, prior to the advent of overt LV remodeling in the presence of moderate to severe MR through the assessment of blood flow dynamics.

2. The cardiovascular system

The cardiovascular system is composed of: heart, blood vessels (also known as the vasculature), cells and plasma of the blood. Blood vessels that carry blood away from the heart are called arteries. Blood vessels that return blood to the heart are called veins. As blood moves through the cardiovascular system, a system of valves in the heart and veins ensures that the blood flows in one direction only. Figure 1 is a schematic diagram that shows these components and the route that blood follows through the body. The heart is divided by a central wall, or septum, into left and right halves. Each half functions as an independent pump that consists of an atrium and a ventricle. The atrium receives blood returning to the heart from the blood vessels, and the ventricle pumps blood out into the blood vessels. The right side of the heart receives blood from the tissues and sends it to the lungs for oxygenation. The left side of the heart receives newly oxygenated blood from the lungs and pumps it to tissues throughout the body. Starting in the right atrium in Figure 1, trace the path taken by blood as it flows through the cardiovascular system. Note that blood in the right side of the heart is colored blue. This is a convention used to show blood from which the tissues have extracted oxygen. Although this blood is often described as deoxygenated, it is not completely devoid of oxygen. It simply has less oxygen than blood going from the lungs to the tissues. From the right atrium, blood flows into the right ventricle of the heart. From there it is pumped through the pulmonary arteries to the lungs, where it is oxygenated. Note the color change from blue to red in Figure 1, indicating higher oxygen content after the blood leaves the lungs. From the lungs, blood travels to the left side of the heart through the pulmonary veins. The blood vessels that go from the right ventricle to the lungs and back to the left atrium are known collectively as the pulmonary circulation. Blood from the lungs enters the heart at the left atrium and passes into the left ventricle from mitral valve. Blood pumped out of the left ventricle enters the large artery known as the aorta. The aorta branches into a series of smaller and smaller arteries that finally lead into networks of capillaries. Notice at the top of Figure 1 the color change from red to blue as the blood passes through the capillaries, indicating that oxygen has left the blood and diffused into the tissues.

After leaving the capillaries, blood flows into the venous side of the circulation, moving from small veins into larger and larger veins. The veins from the upper part of the body join to form the superior vena cava. Those from the lower part of the body form the inferior vena cava. The two venae cavae empty into the right atrium. The blood vessels that carry blood from the left side of the heart to the tissues and back to the right side of the heart are

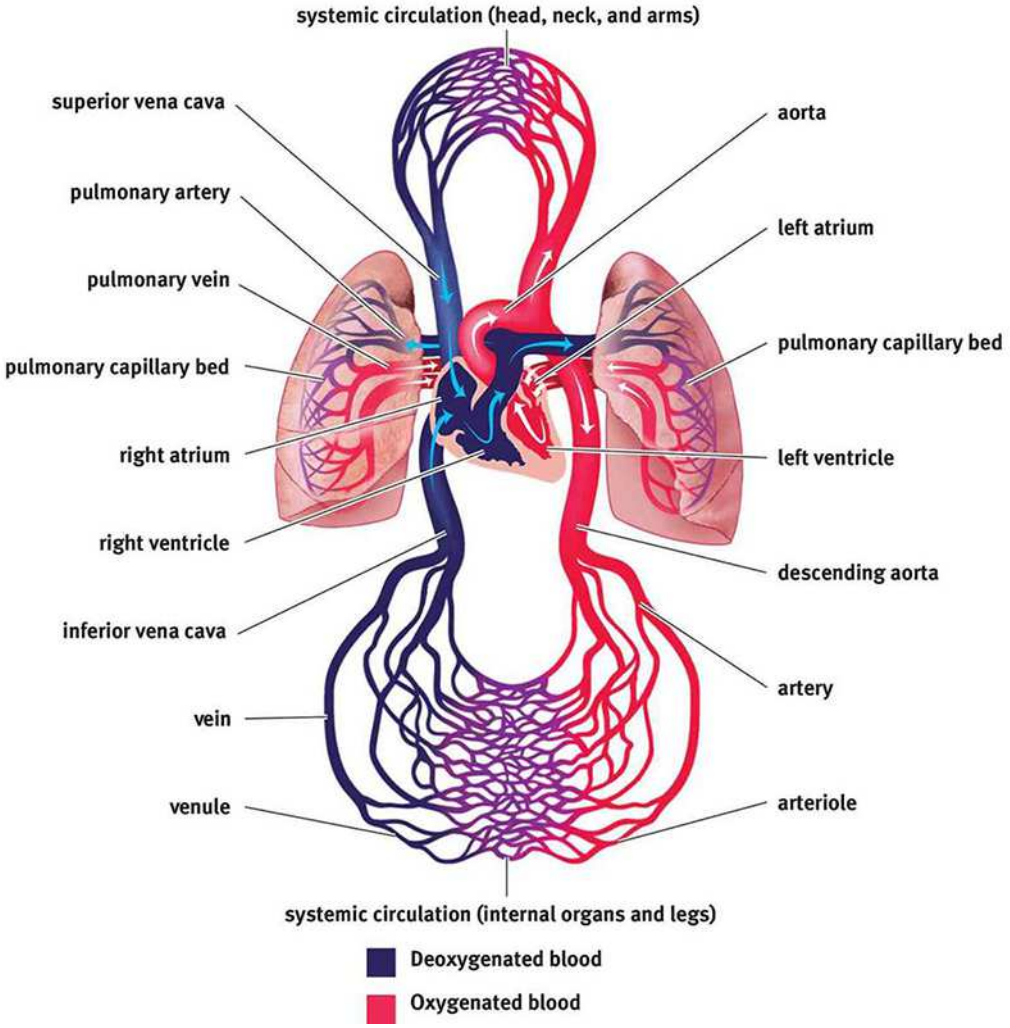

Figure 1: Blood flow in the human heart

collectively known as the systemic circulation.

2.1. Cardiac muscle of the heart

The heart is a muscular organ, about the size of a fist. It lies in the center of the thoracic cavity. Within the thoracic cavity, the heart lies on the ventral side, sandwiched between the two lungs, with its apex resting on the diaphragm. The heart is encased in a tough membranous sac, the pericardium. A thin layer of clear pericardial fluid inside the pericardium lubricates the external surface of the heart as it beats within the sac. The heart itself is composed mostly of cardiac muscle, or myocardium, covered by thin outer and inner layers of epithelium and connective tissue. The

major blood vessels all emerge from the base of the heart. The aorta and pulmonary trunk (artery) direct blood from the heart to the tissues and lungs, respectively. The venae cavae and pulmonary veins return blood to the heart. Blood flows from veins into the atria and from there through one-way valves into the ventricles, the pumping chambers. Blood leaves the heart via the pulmonary trunk from the right ventricle and via the aorta from the left ventricle. A second set of valves guards the exits of the ventricles so that blood cannot flow back into the heart once it has been ejected.

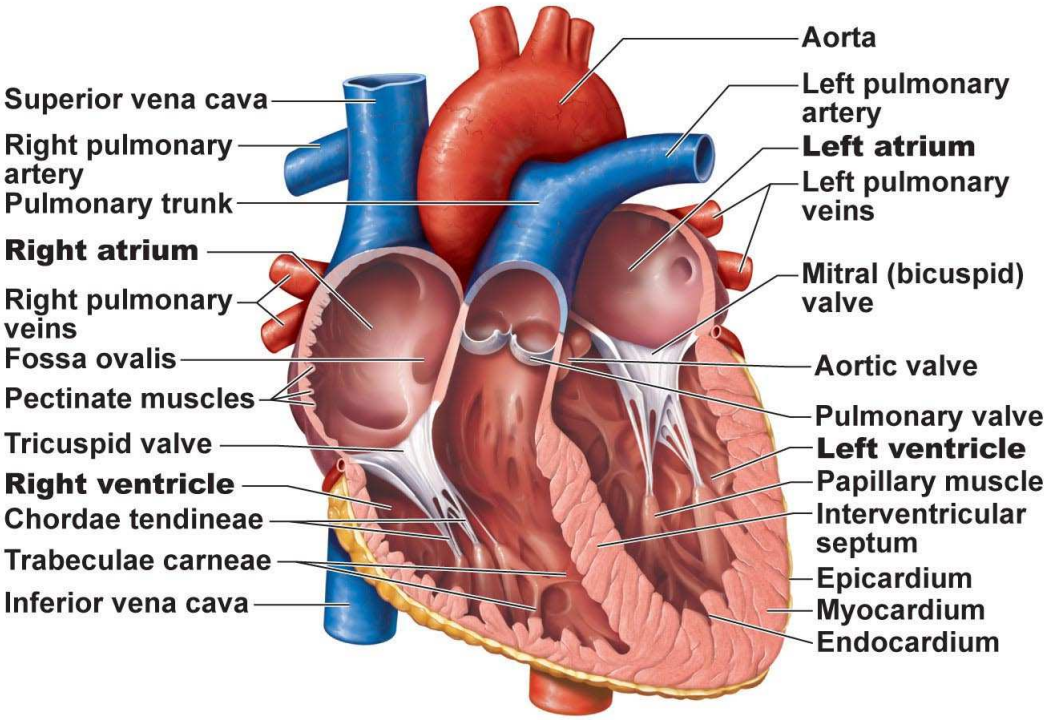

Figure 2: Structure of the heart

Notice in Figure 2 that blood enters each ventricle at the top of the chamber but also leaves at the top. This is because during development, the tubular embryonic heart twists back on itself. This twisting puts the arteries (through which blood leaves) close to the top of the ventricles. Functionally, this means that the ventricles must contract from the bottom up so that blood is squeezed out of the top. Four fibrous connective tissue rings surround the four heart valves (Figure 2). These rings form both the origin and insertion for the cardiac muscle, an arrangement that pulls the apex

and base of the heart together when the ventricles contract. In addition, the fibrous connective tissue acts as an electrical insulator, blocking most transmission of electrical signals between the atria and the ventricles. This arrangement ensures that the electrical signals can be directed through a specialized conduction system to the apex of the heart for the bottom-to-top contraction.

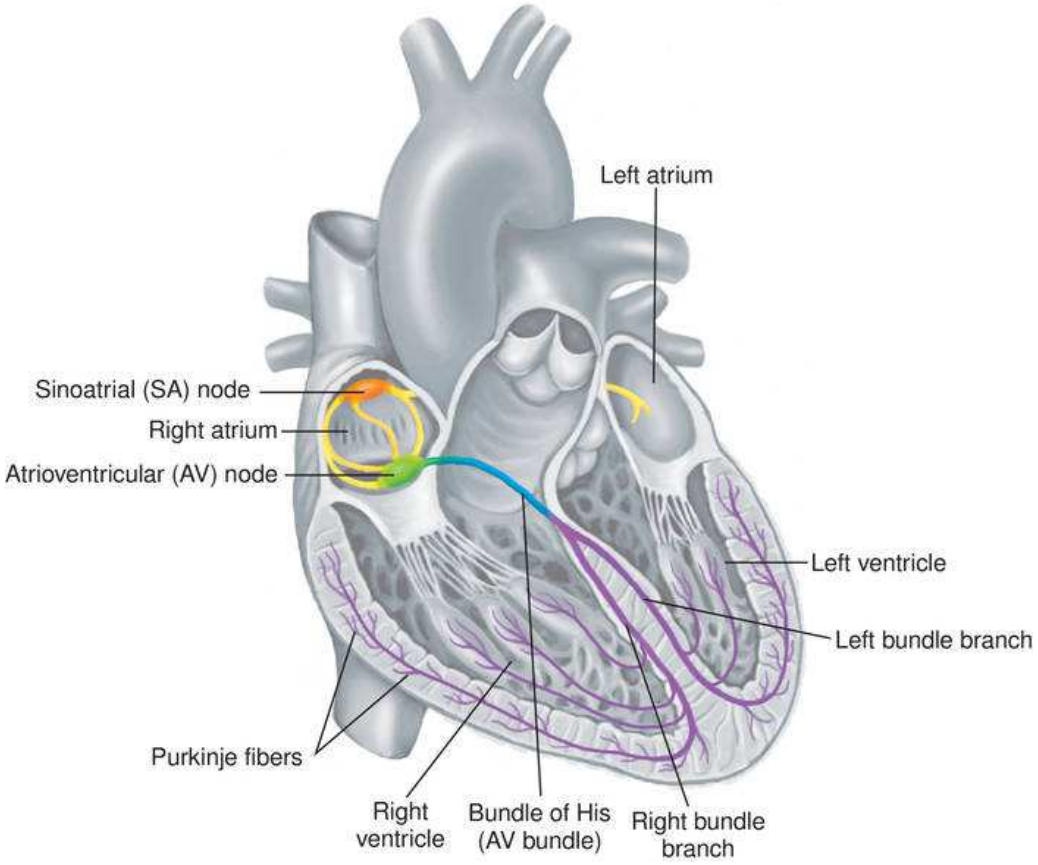

Figure 3: The heart conduction system

The bulk of the heart is composed of cardiac muscle cells, or myocardium. Most cardiac muscle is contractile, but about 1% of the myocardial cells are specialized to generate action potentials spontaneously. These cells account for a unique property of the heart: its ability to contract without any outside signal. The signal for myocardial contraction comes from specialized myocardial cells known as autorhythmic cells. The autorhythmic cells are also called pacemakers because they set the rate of the heartbeat. Electrical communication in the heart begins with an action potential in an autorhythmic cell. The depolarization spreads rapidly to adjacent cells through gap junctions

in the intercalated disks. The depolarization wave is followed by a wave of contraction that passes across the atria, then moves into the ventricles. The depolarization begins in the sinoatrial node (SA node), autorhythmic cells in the right atrium that serve as the main pacemaker of the heart (Figure 3). The depolarization wave then spreads rapidly through a specialized conducting system of noncontractile autorhythmic fibers. A branched internodal pathway connects the SA node to the atrioventricular node (AV node), a group of autorhythmic cells near the floor of the right atrium. From the AV node, the depolarization moves into the ventricles. Purkinje fibers, specialized conducting cells, transmit electrical signals very rapidly down the atrioventricular bundle (AV bundle, also called the bundle of His) in the ventricular septum. A short way down the septum, the AV bundle fibers divide into left and right bundle branches. The bundle branch fibers continue downward to the apex of the heart, where they divide into smaller Purkinje fibers that spread outward among the contractile cells. The heart conduction can be registrated by electrocardiogram (ECG) and a typical trace is reported in figure 4. The QRS complex in the ECG indicates the polarization of the ventricular myocardial fibers, after which the ventricular contraction develops. The ventricular contraction, or systole, pushes blood in the circulation. When contraction is completed the muscular fibers depolarize, revealed by the T-wave in the ECG, and relax allowing the blood to fill the ventricle during diastole. Diastole is then completed by the following atrial contraction. The heart conduction system have a parallel mechanical cycle of ventrivular filling and ejection.

With reference to figure 4 during systole the LV contracts, the mitral valve is closed, its volume decreases and flow is ejected (S-wave) at systolic pressure through the Aorta, during the early filling the myocardium relaxes, pressure decreases below that of the left atrium, aortic valve closes, mitral valve opens and blood flows into the LV that increases its volume; when the E-wave terminates the atrial and ventricular pressure become comparable and flow into the ventricle is very small during diastasis. The atrial contraction completes with the LV filling (A-wave) and the diastolic phase.

2.2. The cardiac cycle

Each cardiac cycle has two phases: diastole, the time during which cardiac muscle relaxes, and systole, the time during which the muscle contracts diastole, dilation; systole, contraction. Because the atria and ventricles do not contract and relax at the same time, we discuss atrial and ventricular events separately. The flow of blood through the heart is governed by the same principle that governs the flow of all liquids and gases: flow proceeds from areas of higher pressure to areas of lower pressure. When the heart

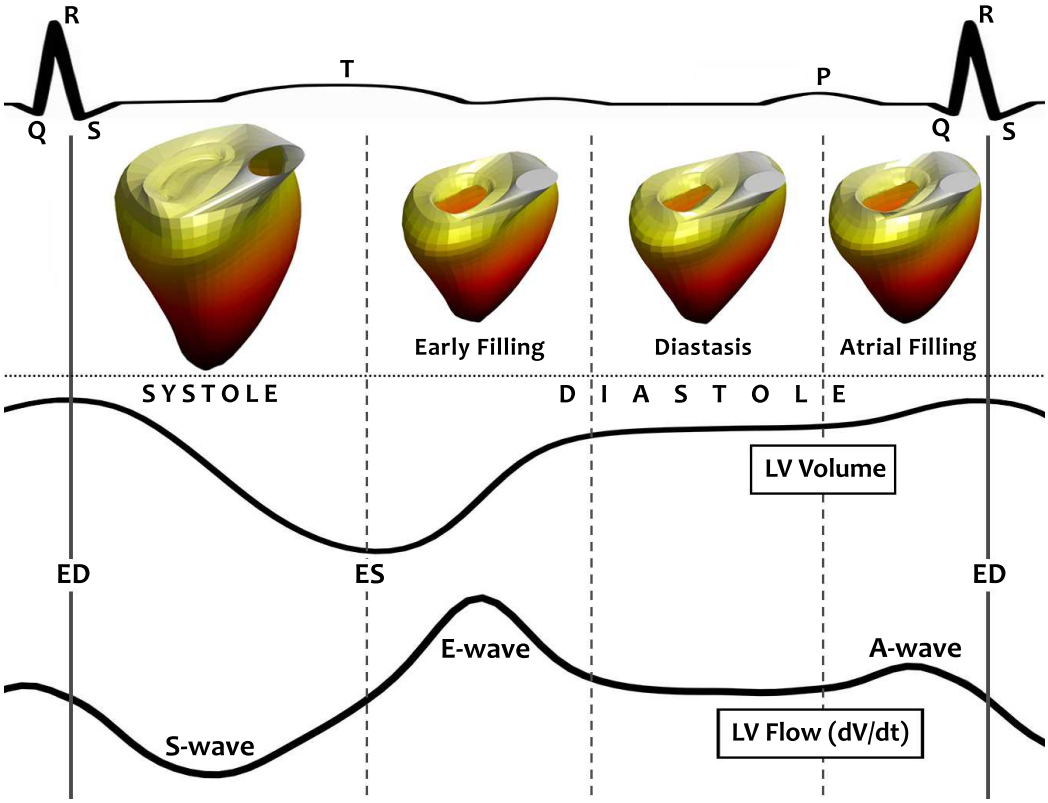

Figure 4: The electro-mechanical cycle

contracts, the pressure increases and blood flows out of the heart into areas of lower pressure. Figure 5 represents pressure and volume changes in the left ventricle, which sends blood into the systemic circulation. The left side of the heart creates higher pressures than the right side, which sends blood through the shorter pulmonary circuit.

The cycle begins at point A. The ventricle has completed a contraction and contains the minimum amount of blood that it will hold during the cycle. It has relaxed, and its pressure is also at its minimum value. Blood is flowing into the atrium from the pulmonary veins. Once pressure in the atrium exceeds pressure in the ventricle, the mitral valve between the atrium and ventricle opens (Figure 5, point A). Atrial blood now flows into the ventricle, increasing its volume (point A to point B). As blood flows in, the relaxing ventricle expands to accommodate the entering blood. Consequently, the volume of the ventricle increases, but the pressure in the ventricle goes up very little. The last portion of ventricular filling is completed by atrial contraction (point A' to B). The ventricle now contains the maximum volume of blood that it will hold during this cardiac cycle (point B). Because maximum

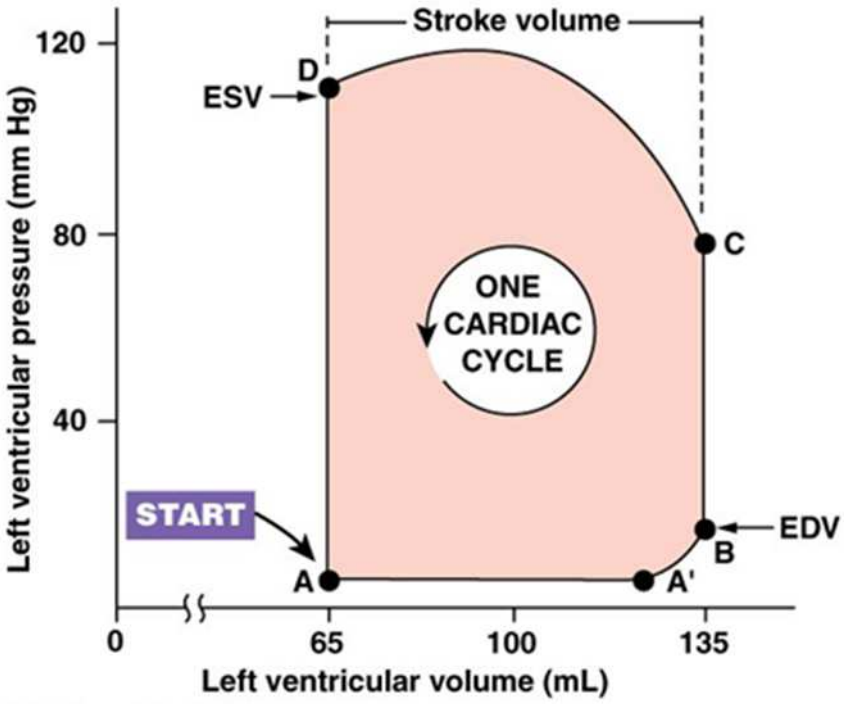

Figure 5: LV Pressure-Volume curve [2013, Person Education, Inc.]

filling occurs at the end of ventricular relaxation (diastole), this volume is called the end-diastolic volume (EDV). When ventricular contraction begins, the mitral valve closes. With both the AV valve and the semilunar valve closed, blood in the ventricle has nowhere to go. Nevertheless, the ventricle continues to contract, causing the pressure in this chamber to increase rapidly during isovolumic contraction (B $\longrightarrow$ C in Figure 5). Once ventricular pressure exceeds the pressure in the aorta, the aortic valve opens (point C). Pressure continues to increase as the ventricle contracts further, but ventricular volume decreases as blood is pushed out into the aorta (C $\longrightarrow$ D). The heart does not empty itself completely of blood each time the ventricle contracts. The amount of blood left in the ventricle at the end of contraction is known as the end$-$systolic volume (ESV). The ESV (point D) is the minimum amount of blood the ventricle contains during one cycle. At the end of each ventricular contraction, the ventricle begins to relax. As it does so, ventricular pressure decreases. Once pressure in the ventricle falls below aortic pressure, the semilunar valve closes, and the ventricle again becomes a sealed chamber. The remainder of relaxation occurs without a change in blood volume, and so this phase is called isovolumic relaxation (Figure 5, D $\longrightarrow$ A). When ventricular pressure finally falls to the point at which

atrial pressure exceeds ventricular pressure, the mitral valve opens and the cycle begins again. Cardiac output (CO) can be calculated by multiplying heart rate (beats per minute, bpm) by stroke volume (mL per beat, or per contraction):

$$Cardiac\ output = Heart\ rate \times Stroke\ volume \tag{1}$$

A physiological value of CO is about 5 L/min. For instance, for an average resting heart rate of 72 beats per minute and a stroke volume of 70 mL per beat, we have 5 L/min. Average total blood volume is about 5 liters. This means that, at rest, one side of the heart pumps all the blood in the body through it in only one minute. Normally, cardiac output is the same for both ventricles. However, if one side of the heart begins to fail for some reason and is unable to pump efficiently, cardiac output becomes mismatched. In that situation, blood pools in the circulation behind the weaker side of the heart. Stroke volume, the volume of blood pumped per ventricle per contraction, is directly related to the force generated by cardiac muscle during a contraction. Normally, as contraction force increases, stroke volume increases. In the isolated heart, the force of ventricular contraction is affected by two parameters: the length of muscle fibers at the beginning of contraction and the contractility of the heart. The volume of blood in the ventricle at the beginning of contraction (the end-diastolic volume) determines the length of the muscle. The length-tension relationship observed in isolated muscles can also be seen in the intact heart: as stretch of the ventricular wall increases, so does the stroke volume. If additional blood flows into the ventricles, the muscle fibers stretch, then contract more forcefully, ejecting more blood. The degree of myocardial stretch before contraction begins is called the preload on the heart because this stretch represents the load placed on cardiac muscles before they contract. The stroke volume is calculated as SV=EDV-ESV and it's usually normalized with the EDV to provide a dimensionless measure of the entity of the contraction relative to the available volume. This measure is defined ejection fraction

$$EF = \frac{V_{ED} - V_{ES}}{V_{ED}} = \frac{SV}{V_{ED}} \tag{2}$$

which represents the most common clinical parameter to assess the LV function. Evaluation of EF requires the evaluation of LV volumes, which can be performed with numerous methods based on imaging, from echocardiography to MRI and others. In normal hearts the EF is usually about 65%, and considered abnormal when it falls below 55% (although exact figures depend on the measurement method). The reduction of the EF commonly reveal the

presence of a cardiac dysfunction, although there are also few pathologies that present a preserved EF.

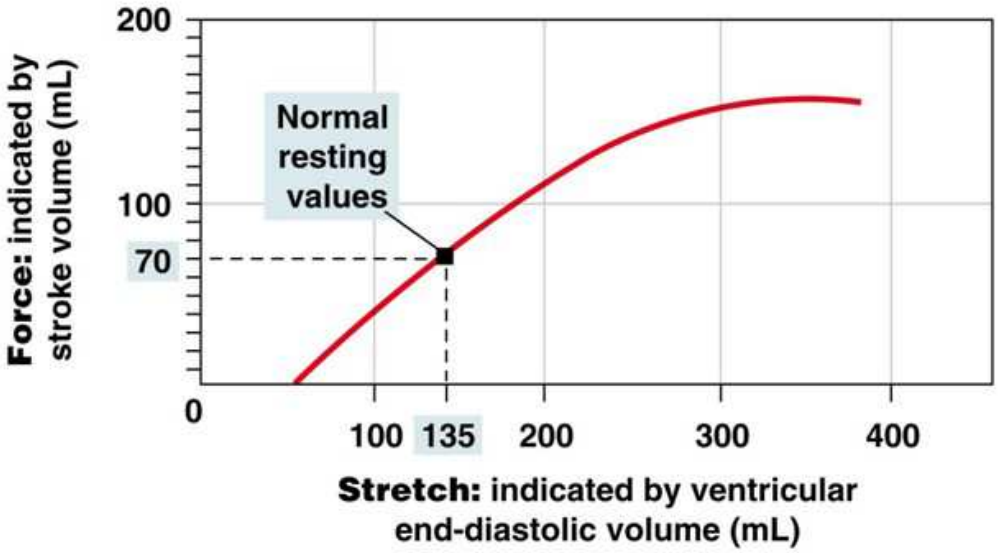

Figure 6: Starling curve

The relationship between stretch and force in the intact heart is plotted on a Starling curve (Figure 6). The x-axis represents the end-diastolic volume. This volume is a measure of stretch in the ventricles, which in turn determines sarcomere length. The y-axis of the Starling curve represents the stroke volume and is an indicator of the force of contraction. The graph shows that stroke volume is proportional to EDV. As additional blood enters the heart, the heart contracts more forcefully and ejects more blood. This relationship is known as the Frank-Starling law of the heart. It means that within physiological limits, the heart pumps all the blood that returns to it. According to the Frank-Starling law, stroke volume increases as end-diastolic volume increases. End-diastolic volume is normally determined by venous return, the amount of blood that enters the heart from the venous circulation. Three factors affect venous return: (1) contraction or compression of veins returning blood to the heart (the skeletal muscle pump); (2) pressure changes in the abdomen and thorax during breathing (the respiratory pump); (3) sympathetic innervation of veins. The combined load of EDV and arterial resistance during ventricular contraction is known as afterload. Increased afterload is found in several pathological situations, including elevated arterial blood pressure and loss of stretchability (compliance) in the aorta. To maintain constant stroke volume when afterload increases, the ventricle must increase its force of contraction, which then increases the muscle's need for

oxygen and ATP production. If increased afterload becomes a chronic situation, the myocardial cells hypertrophy, resulting in increased thickness of the ventricular wall. Clinically, arterial blood pressure is often used as an indirect indicator of afterload. Cardiac output varies with both heart rate and stroke volume. Heart rate is modulated by the autonomic division of the nervous system and by epinephrine.

3. Left ventricular disease

Pathologies of the left ventricle can be roughly classified, by a mechanical viewpoint, as those due to a reduced myocardial contraction (perfusion defect) or to a general inability to properly deliver an appropriate contraction/relaxation rhythm that can progressively lead to the syndrome of heart failure. Further pathologies are imputable to dysfunctions of electrical conduction; some of these can be purely neurological defects, like fibrillations, some others can lead to improper contraction or relaxation and, either mechanically or therapeutically, are included in the class of heart failure. Other dysfunctions are imputable to pathologies of cardiac valves, which are discussed later in dedicated sections. It should altogether keep in mind that many such pathologies are inter-related and the present classification is driven by discussion on intraventricular fluid dynamics more than on clinical scenarios.

3.1. Myocardial ischemia

The most known pathology of the left ventricle is ischemia, whose extreme is the myocardial infarction, that is a consequence of the reduction of myocardial perfusion due to coronary stenosis. This is, therefore, a consequence of vascular disease; when a coronary reduces blood flow, the myocardial territory perfused by that vessel receives less oxygen allowance and reduces its contractile ability. The ischemic disease is commonly considered a systolic dysfunction because the myocardium is unable to properly contract during systole. Ischemic diseases present a reduction of the EF; this reduction is mostly due to regional contractile defect, in the poorly perfused myocardial region, that can be recognized by cardiac imaging methods allowing visualization and quantification of myocardial motion. When this defect is small, it can be hidden and may become appreciable only under stress condition, thus requiring imaging performed under exercise of pharmacologic stress. In alternative, perfusion defects can be evaluated by perfusion imaging techniques, available in nuclear imaging, MRI and, sometime, echocardiography. When recognized, they are eventually evaluated by coronary angiography to assess the actual coronary stenosis as discussed previously. Intraventricular fluid dynamics is also affected by myocardial ischemia. Blood near a segment that presents a reduced motility is more stagnant, especially when this is near the LV apex. This gives a reduction of wash-out and increased risk of thrombi. It also creates an imbalance in the intraventricular forces with overstresses in some regions, even distant from the infarcted zone. Over-stresses, or anomalous stresses, can progressively induce a feedback and ventricular adaptation that alters the LV geometry with potential further pathological

implications. Ischemia is typically solved by coronary endovascular surgery. However, when the solution is not complete, for example when one or few are treated among multiple stenosis, some ischemia may remain and give ventricular imbalances. Similarly, when the ischemia has lasted for too long time, some regions of the myocardium may not be able to fully recover its contractile ability. In presence of such remaining imbalances may induce ventricular adaptation and progressive dysfunction.

3.2. Heart failure

Heart failure (HF) is the principal social threatening cardiac progressive dysfunction. It presents either as a primary pathology or as a consequence of numerous primary diseases. It can be a consequence of partly recovered ischemia; it can follow electrical dysfunctions that do not allow a synchronous of contraction; it can simply due to varied stiffness/thickness in the myocardium that does not allow a uniform relaxation, to cite a few examples. On the other hand, it can develop as a primary disease following poor medical conditions. In any case, heart failure is the terminal stage of a progressive disease associated with impaired cardiac function. The clinical syndrome of heart failure is associated with the development of ventricular remodeling: a modification of ventricular geometry that progressively alters its functional parameters whose final stage is the LV dilatation, known as dilated cardiomyopathy (DCM). Remodeling represents a physiologic adaptation feedback that often does not lead to a stable configuration rather to a progressively worsening of the cardiac function and eventually to failure. Despite modern treatments, hospitalization and death rate remains high, with nearly 50% of people diagnosed with heart failure dying within 5 years. The physiological causes leading to LV remodeling (as exemplarily sketched

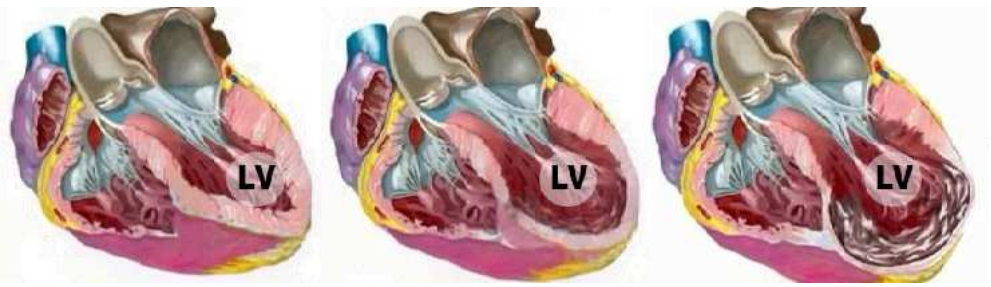

Figure 7: Progression of left ventricular (LV) remodelling after an ischemic event. Left side: a ventricle with normal geometry and a regional reduced contractility. Centre: a moderately dilated ventricle. Right: a dilated cardiomyopathy at the late stage of heart failure.

in Figure 7 for a case of ischemia) are mainly ascribed to an increase of

stress on the myocardial fibers, which stimulates the growth and multiplication of cells giving rise to an increase of muscular thickness (hypertrophy) or extension (local dilatation). However this picture is unable to differentiate patients exhibiting differences in LV structure and function, it is not consistently predictive of the future risk of cardiac remodeling and does not clarify how a regional disease rapidly remodels the LV as whole. The availability of predictive models that can forecast progression or reversal of LV remodeling following initiation of therapeutic interventions would be invaluable for overall risk stratification, improvement of preventive healthcare, and reduction of the perspective social burden. Progressive disease and heart failure have

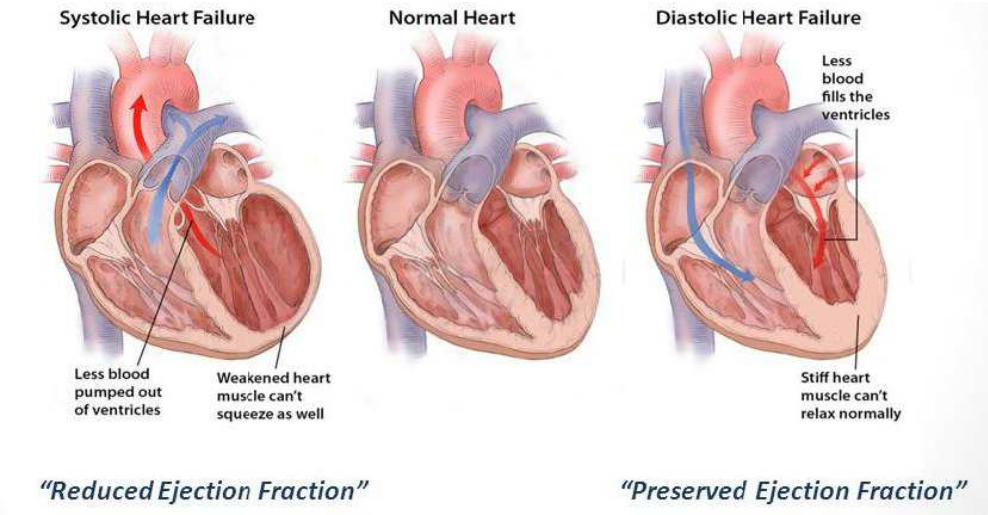

Figure 8: Types of remodeling and heart failure.

numerous possible causes and can also develop in different ways, as shown in figure 8. Heart failure is most commonly associated to ventricular dilatation (DCM). In this case, the myocardium is stretched and thinner. The heart muscle contract very little and is able to eject a sufficient SV with small contraction because of the large volume. The EF is well reduced, and we talk about HF with reduced ejection fraction (HFrEF), also referred to as systolic heart failure. In HFrEF, the intraventricular fluid dynamics is very weak; the SV is a small percentage of the chamber volume. Typically, blood flow takes either a continuous weak rotary motion, when the inflow is aligned to feed the central vortex, or it presents a weak turbulence. In both cases, flow is featured by stasis and thrombus risk. Intraventricular hemodynamic forces are reduced and incoherent. Another type of HF is associated with thickening and/or stiffening of the myocardium. The ventricular volume is about normal and the pumping parameters are also normal

but the ventricle does not relax properly during ventricular filling because of its stiffness. The EF is thus preserved, usually because the ventricle is hypertrophic and the inward thickening helps supporting systolic ejection. volume reduction. In this case, that is more difficult to recognize, we talk about HF with preserved ejection fraction (HFpEF), also referred to as diastolic heart failure. Intraventricular blood flow in this case is more similar to normal; however, dynamical difference reflecting the altered filling pattern are expected although not studied, yet. The causes leading to LV remodeling are still largely incomplete. During the progression there are changes in the pumping function. These can be noticed by changes in the relative intensity between E-wave and A-wave, with an extra-burst by atrial contraction when early filling is insufficient, or alteration of timing of acceleration and decays of E-wave. Clinicians use the combination of numerous indicators trying to figure out the specific pathological scenario; however a comprehensive mechanical picture is still missing. It has been recently shown that alteration in the intraventricular fluid dynamics are observable well before the tissue has undergone to noticeable often-irreversible changes. Given the incompressible nature of blood, in a cardiac chamber that is filled with blood, every segment is somehow in touch with the others and, as a result, the blood inertia associated with the rapid acceleration-deceleration about one region can instantaneously influence distant regions. The role of flow on cardiac remodeling has been considered in the past only through global indicators like volumetric changes, the inflow velocity of E- and A-wave, or combinations thereof. The absence of more specific fluid dynamics indicators is mainly due to the lack of technologies able to evaluate intraventricular fluid dynamics with sufficient ease and reliability. Normal intraventricular fluid dynamics is known to be associated to a physiologically stable cardiac function that does not lead to remodeling. Vice versa, a progressive disease corresponds to a physiologically unstable state that is expected to proceed further away from normality. As shown schematically in figure 9, an alteration of intraventricular fluid dynamics induces alteration of forces and shear stress on the tissue, these can trigger adaptation feedbacks and bring to progressive dysfunction. In an initial phase, the alteration of flow-mediated stresses may lead to stiffening of the myocardial tissue that sometime is associated to the increase of myocardial thickness (hypertrophy). This can be a condition going to HFpEF, or a quick passage toward progressive tissue dilatation with further reduction of LV function and eventually going to the more common HFrEF. Therapies for heart failure are complicated as they should go to the cause leading to remodeling. Moreover, HF often involves dysfunction in physiologically related organs and, therefore, precise guidelines are not available, and therapies are varied. Multipoint pace makers were shown to

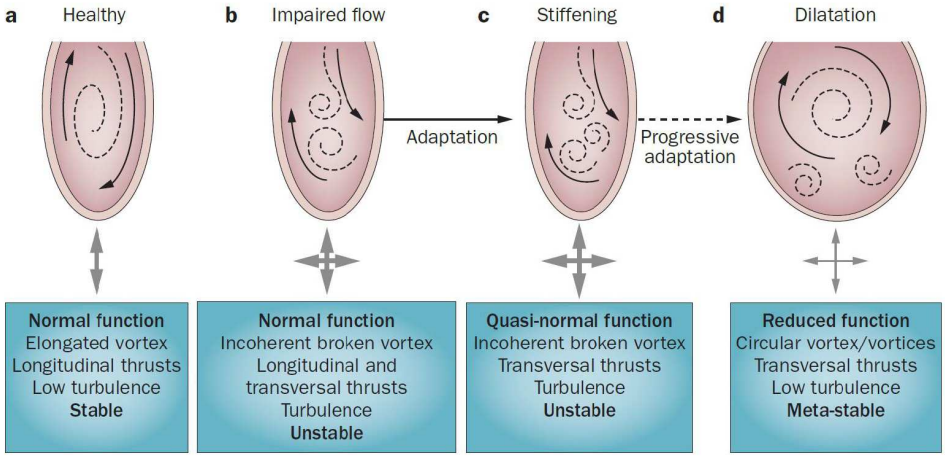

Figure 9: Flow-mediated path toward heart failure.

be one successful option in many cases, especially when HF is associated with a disturbed electrical activity (either as a cause or a consequence of HF), because they permit to restore a synchrony in LV contraction and relaxation. This approach, called cardiac resynchronization therapy (CRT), requires the definition of stimulation intervals in the pace-maker to ensure optimal therapeutic outcome. Typically, they can be chosen by electric conduction optimization or though synchronization of myocardial tissue motion. However, the rate of success is still low (nearly 40% patients do not benefit of CRT). Fluid dynamics offers a global perspective to define the proper contraction pattern, by ensuring that hemodynamic forces are maximized and properly aligned along the base-apex direction. However, studies are currently in progress to verify its effective clinical results. This concept can, however, be generalized to evaluate the normality of cardiac function after the acute cause that may, or may not, lead to heart failure. These include endovascular prosthesis, valvular repair or transplant, and so on. Intraventricular fluid dynamics appears as the first mechanical factor modified after, even minor, alteration of cardiac function. It appears a promising central element for the prediction of progressive disease or of therapeutic outcomes.

4. Mitral valve anatomy and disease

4.1. Mitral valve anatomy

The mitral valve is a bi-leaflet structure composed by annulus, commissures, leaflets, chordae tendineae and papillary muscles, and left ventricle is crucial for its functional integrity (figure 10). The mitral annulus is a fibro-

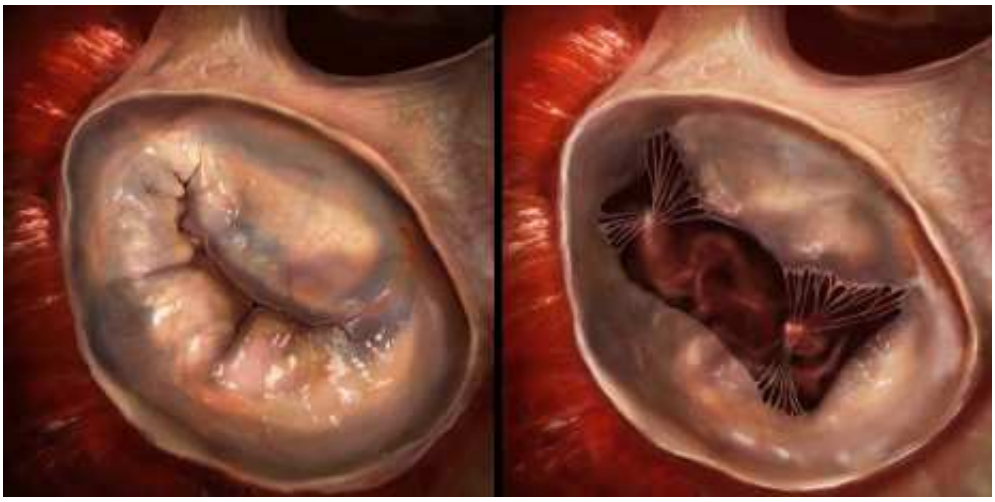

Figure 10: Mitral valve, close (left) and open (right) showing the chordae tendineae attaching the leaflets to the papillary muscles inside the ventricle

muscular ring to which the anterior and posterior mitral valve leaflets attach. The right trigone is a fibrous area situated between the membranous septum, the mitral valve, the tricuspid valve, and the noncoronary cusp at the aortic annulus. The left trigone is a fibrous area located at the nadir of the left coronary cusp of the aortic annulus and the left border of the aortic-mitral curtain. The aortic-mitral curtain is the fibrous tissue between the anterior mitral valve leaflet, the left and noncoronary cusps of the aortic valve, and the left and right trigone [10]. The posterior portion of the annulus is less developed owing to the discontinuity of the fibrous skeleton of the heart in this region. This difference explains why the posterior portion of the mitral annulus is more prone to pathologic dilation while the anterior portion is relatively resistant [62]. The annulus is a dynamic non-planar structure that undergoes deformation in its circumference, excursion, curvature, shape, and size for proper function, which makes it susceptible to ventricular remodeling [66, 49]. The atrial surface is free of any attachments whereas the ventricular surface connects to the papillary muscles via the chordae tendinae. The chordae tendinae are fibrous extensions originating from the heads of the papillary muscles and are responsible for determining the position and tension

on the anterior and posterior leaflets at LV end-systole. The two papillary muscles, the anterolateral and the posteromedial, originate from the area between the apical and middle thirds of the LV free wall. The anterior leaflet is the largest, positioned between the mitral orifice and the left ventricular outflow tract, while the smaller posterior leaflet is placed to the left of the mitral orifice close to the posterior-lateral wall.

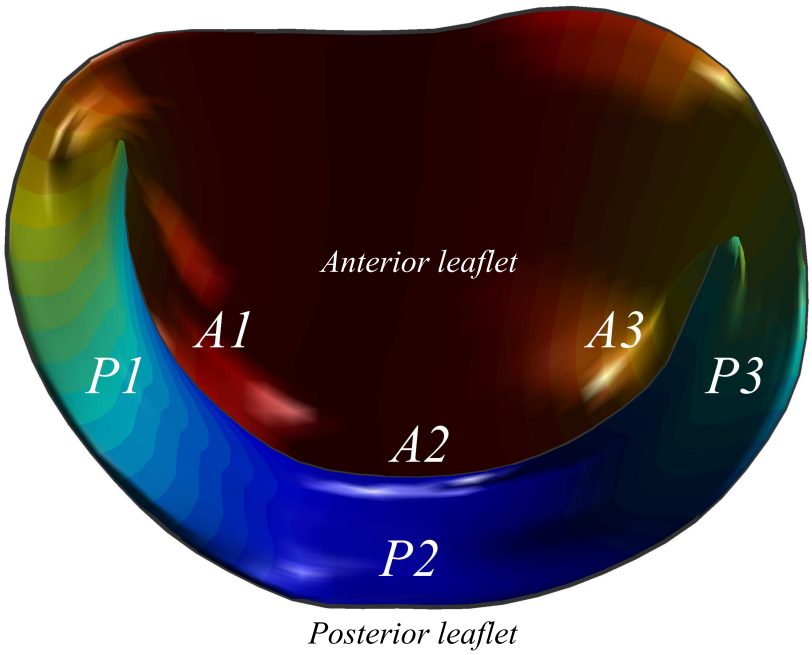

Figure 11: Schematic diagram of the mitral valve

Functional classification of valve dysfunction, is based Carpentier's [15] characterization of leaflet motion that identifies the anterolateral, medial and posteromedial scallops of the posterior leaflet as P1, P2 and P3, and the anterior leaflet as A1, A2 and A3, respectively [24]. The distinct area where the anterior and posterior leaflets coapt during systole is known as the rough zone.

4.2. Mitral valve prolapse

Mitral valve prolapse (MVP) is the common cause of the mitral regurgitation (MR) that affects approximately 2.4% of the population [41], which is typically caused by myxomatous degeneration of the valve [34]. Functional classification of MR is based Carpentier's pathophysiologic triad [15], it classifies MV dysfunction based on three types of leaflet motion. In type

I the leaflets have a normal movement and regurgitation is due to annular dilatation and incomplete coaptation of the leaflets from insufficient available surface of coaptation; in type II the leaflets are prolapsed or hypermobile, due to excess leaflet height, volume, elongation or rupture of chordae tendineae or by lengthening or rupture of the papillary muscles. Finally, in type III dysfunction the leaflets have a restricted movement caused by chordal tethering from chordal fibrosis, papillary displacement, and/or leaflet fibrocalcific or hypoplastic etiology. MVP results primarily from two distinctive types of degenerative disease: Barlow's disease and fibroelastic deficiency.

4.2.1. Barlow's disease

Barlow disease results from an excess of myxomatous tissue, which is an abnormal accumulation of mucopolysaccharides in one or both leaflets and chordae [5]. This myxoid infiltration results in thick, redundant, billowing leaflets and elongated chordae, which often lead to bileaflet, multisegmental prolapse (Figure 12 (a))and is seen often in younger patients.

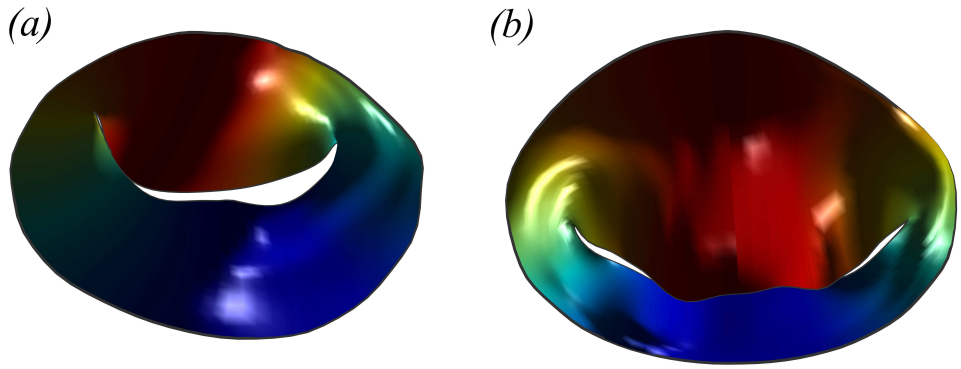

Figure 12: Pathological MV: (a) Barlow disease, (b) Fibroelastic deficiency.

4.2.2. Fibroelastic deficiency

Fibroelastic deficiency results in acute loss of mechanical integrity due to abnormalities in the connective and elastic fibrous elements of the leaflet extracellular matrix scaffold architecture [5]. It usually leads to either a localized or unisegmental prolapse due to chordal elongation or rupture (Figure 12 (b)). Fibroelastic deficiency is more prevalent in older patients over 65.

4.3. Ischemic mitral regurgitation

Ischemic MR is a pathophysiologic outcome of ventricular remodeling arising from ischemic heart disease. The adverse changes that occur in the

ventricle after an ischemic event commonly result in type IIIB dysfunction of the mitral valve with leaflet restriction during systole [15]. The resultant volume overload caused by MR worsens myocardial contractility, which in turn worsens LV dysfunction, eventually leading to heart failure and death [61, 48].

4.4. Mitral stenosis

The most prevalent cause of native mitral stenosis (MS) is rheumatic mitral valve disease [102], other causes including congenital, inflammatory, and infiltrative etiologies. These diseases result in lesions such as commissure fusion (in rheumatic disease), leaflet thickening and retraction, and chordae fusion, which lead to leaflet restriction primarily during diastole [56]. According to Carpentier's classification of mitral valve dysfunction, this constitutes a type IIIA dysfunction [15].

5. Mitral valve surgical approach

5.1. Mitral valve repair

Degenerative mitral valve disease is defined by a wide spectrum of lesions and therefore requires a wide variety of surgical techniques to be repaired [1]. Mitral valve repair is performed following a sequential approach as follows:

(1) Repair of all areas of valve pathology;
(2) Reestablishment of leaflet support and surface of coaptation;
(3) Creation of a posterior leaflet closure line away from the outflow tract;
(4) Stabilization of the repair with an annuloplasty device;
(5) Repair of any residual lesions following primary repair.

If posterior leaflet prolapse is due to fibroelastic disease, it is most commonly treated by a targeted triangular (Figure 13 (a)) resection of the segment affected [2]. The prolapsing segment is subsequently removed, and primary closure of the resection margins restores leaflet continuity. In the setting of limited leaflet tissue, a more conservative approach is preferred to avoid undue leaflet tension. Non resection strategies may involve leaflet resuspension and/or ventricular using using artificial chordae from expanded polytetrafluoroethylene (ePTFE) (loop technique, loop-in-loop technique, or single neochordoplasty) (Figure 13 (c)). If additional coaptation surface is required, free edge remodeling strategies may be used including division of primary and secondary restrictive chordae and mobilization of the remaining leaflet body and tethered clefts. In the presence of diffuse excess leaflet height and/or width a sliding leaflet- plasty may be used to correct the residual height (Figure 13 (b)). Reattachment of the leaflet to the annulus will reduce the leaflet height several millimeters, depending on the depth of suture bites. Any gaps in support, or any areas supported by thinned-out chordae (even in the absence of prolapse), are reinforced by transposition of previously detached secondary chordae, or artificial PTFE neochords. Correction of residual anterior leaflet dysfunction is usually addressed after the insertion of the annuloplasty device. The anatomic disposition of the anterior leaflet does not allow aggressive resection of the leaflet margins. Therefore, surgical strategy to correct opposing anterior leaflet prolapse includes targeted (limited to the rough area of the leaflet) or no resection. After saline testing with pressurization of the left ventricle, correction of the anterior leaflet prolapse using one or a combination of the following techniques might be performed:

(1) Chordal transfer of healthy secondary chordeae, or posterior leaflet flip, using a small segment of posterior leaflet free edge with its attached

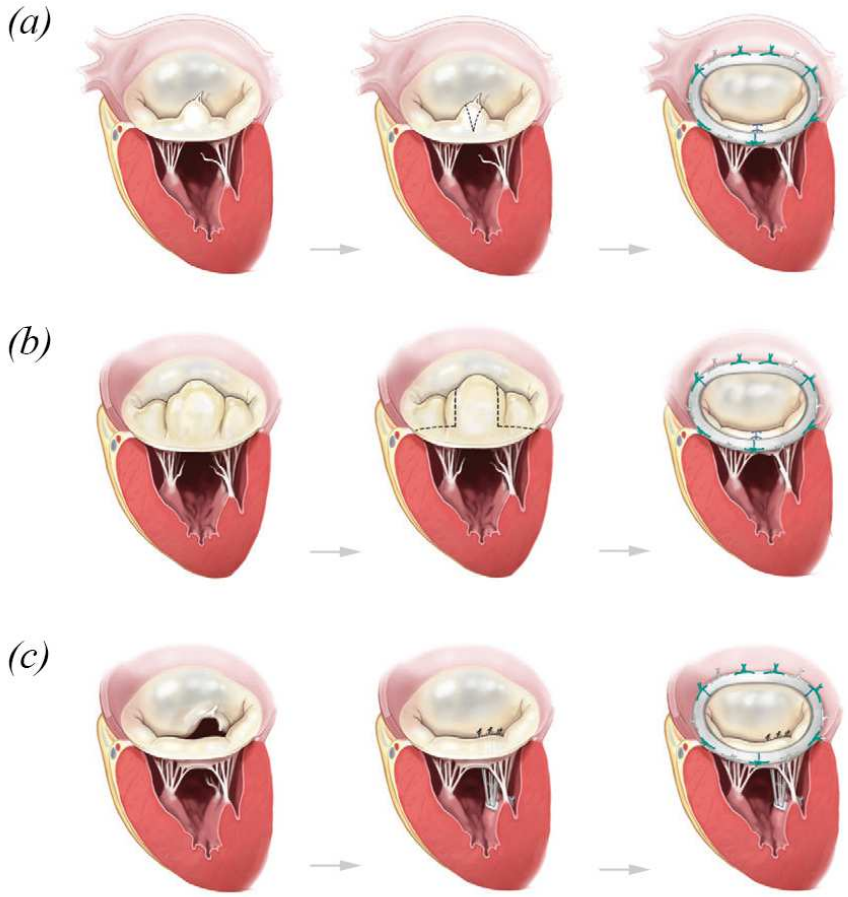

Figure 13: Different surgical approaches of MV reparation. (a) Triangular resection, (b) quadrangular resection and sliding leaflet plasty, (c) neochordoplasty with polytetrafluoroethylene sutures [16].

native chordae;
(2) Neochordoplasty with artificial PTFE chordae;
(3) Limited triangular resection of a prolapsing segment.

Finally, commissural prolapse can be addressed by placing one or two vertical mattress sutures to imbricate the opposing segments of A1/P1 or A3/P3 segments. PTFE neochords may be used to support the reconstructed commissure as needed [16]. The mitral annulus is also examined to assess the presence of annular dilation, which is very common in advanced mucoid degeneration, and should always be considered prior to committing to resection strategies as well as to assess the risk of systolic anterior motion of the an-

terior leaflet and/or chordae [14] (Figure 14). Because leaflet restriction in ischemic MR results in less leaflet tissue available for coaptation, it is necessary to use a complete remodeling ring [42] to ensure an adequate surface of coaptation after annuloplasty [26]. This method combines the principles of undersizing with the specific asymmetric deformation observed with type IIIb ischemic MR. In cases of severe leaflet tethering and moderate to severe LV dilation, several adjunctive techniques as well as alternative procedures have been advocated, including division of secondary chords, [13] posterior leaflet extension with a pericardial patch, repositioning of the papillary muscles, and mitral valve replacement with chordal sparing [12].

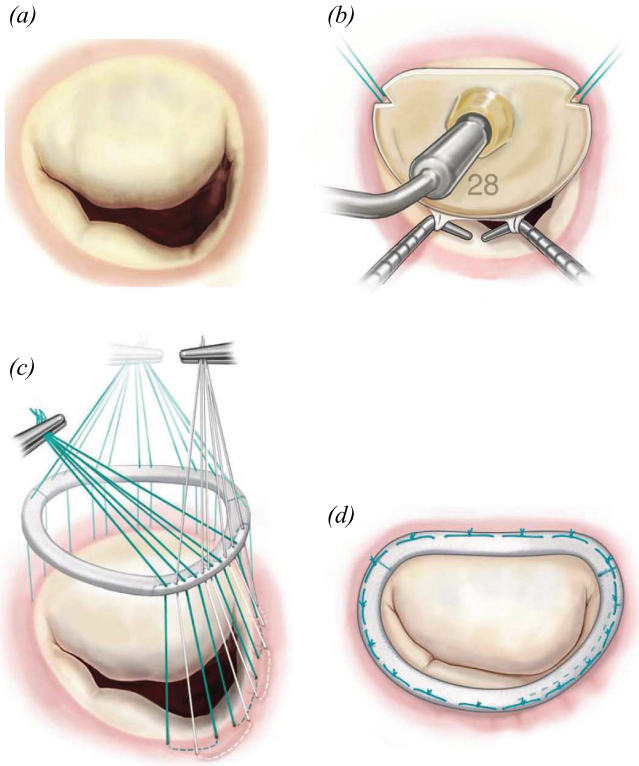

Figure 14: Ischemic mitral regurgitation repair. (a) typical findings with leaflet restriction predominantly in the P2-P3 region, (b) sizing of the annulus with a ring sizer, (c) the sutures in the annulus at the position of the anterior commissure and trigone are placed last, taking advantage of previously placed sutures to expose this area, (d) after placement of a full-remodeling ring, the surface of coaptation is restored (below the plane of the annulus) [16].

5.2. NeoChord procedure

The NeoChord procedure is a feasible alternative to conventional surgery for patients in the early stages of disease, when the lesions responsible for the mechanism of mitral regurgitation are limited to the mitral leaflets and/or chordae tendinae, including elongation or rupture, and do not include mitral annular or LV cavity dilatation [22]. This procedure allows placement of e-PTFE sutures as replacement neochordae on a beating heart without the need for cardiopulmonary bypass (CPB), while using 2D- and 3D-transesophageal echocardiography (TEE) guidance [97, 21]. Two concentric, round purse-string sutures with opposite closure points are placed using large custom-made, rectangular Teflon pledgets and 2-0 non-absorbable suture. Once the device enters the LV cavity, the apical purse-strings are gently tightened to minimize blood leakage and facilitate device insertion (Figure 15 (a)). The device is directed towards the mitral valve plane using 2D-TEE guidance (X-plane with ME LAX and MC views) avoiding interference with adjacent subvalvular structures.

Progression from the LV toward the MV is performed by advancing the device into the thorax perpendicular to the dome of the posterior leaflet and MV annular plane. Once the MV annular plane has been crossed, the TEE imaging mode should be switched from 2D to full 3D imaging, using a surgical or en face view of the mitral valve to demonstrate the tip of the device and to visualize movement of the device tip towards the target mitral leaflet segment. When an appropriate position has been achieved, the jaws of the device are opened and the leaflet edge is gently grasped by withdrawing the device slowly away from the left atrium. Once the leaflet capture is confirmed, is insered the device needle through the leaflet segment and made a loop of the suture through the leaflet (Figure 15 (b)). Once the suture loop has been retrieved from the device, the apical purse string sutures are loosened and the device is retracted from the ventricle with the jaws open and immediately after the two ends of the suture will be visualized and placed through the suture loop to form a girth hitch knot, which is advanced to the free edge of the captured leaflet while the two ends remain outside the chest for final fixation on the apex (Figure 15 (c)). The device is reloaded with a new suture and the procedure is repeated until enough neochordae have been implanted to achieve the desired level of valve competence and subsequent reduction in regurgitation (Figure 15 (d)). When the desired number of neochordae have been placed, the apical purse-strings are tied. A French-eye needle is used to pass all the neochordae through a round pledget which is fixed with a 4-0 Prolene suture over the ventriculotomy and tourniquets are placed over each of the neochordae. The respective length of each NeoChord is then adjusted to achieve optimal leaflet apposition with the lowest degree

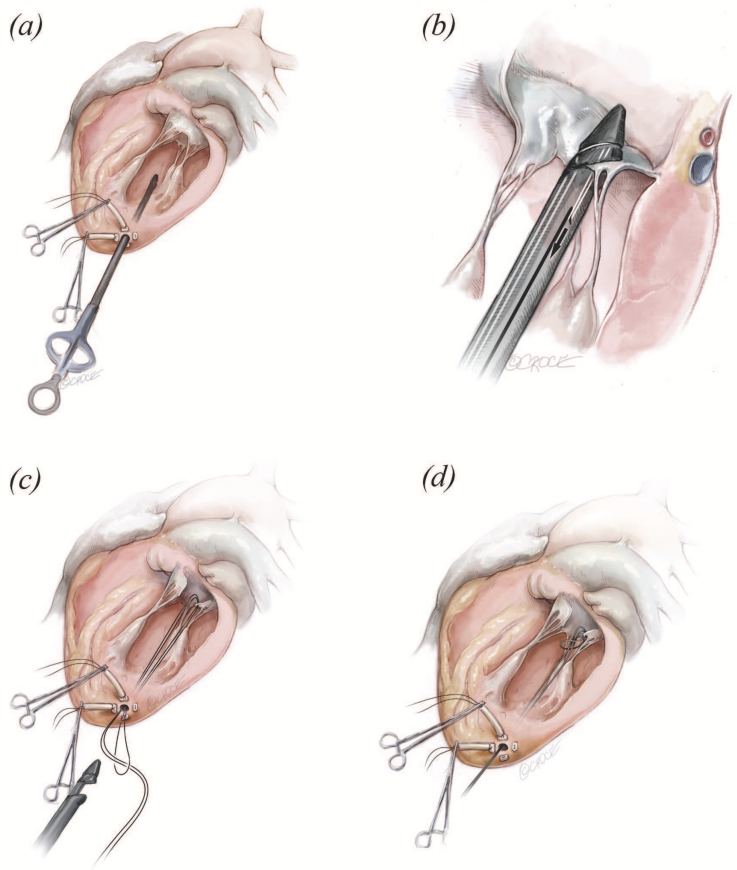

Figure 15: NeoChord procedure: (a) posterolateral LV access, (b) leaflet capture, insertion of the needle and loop of the suture through the leaflet, (c) performing of the girth hitch knot, (d) loop of the procedure with a new suture until a reduction in regurgitation [22].

of mitral regurgitation. Once the length of the neochordae is adjusted, each NeoChord is securely tied to the epicardial pledget.

5.3. MitraClip

A different solution useful for critical mitral regurgitation conditions and for patients that cannot undergo conventional open-heart surgery has been recently introduced. It consists of a "clip" (similar to a paper clip) introduced trans-catheter that sticks together the two leaflet thus transforming the wide prolapsed orifice in two small orifices, as shown in figure 16, that do not allow regurgitation when closed. This method is a trans-catheter version of a conservative surgical strategy called edge-to-edge repair [3]. After Mitral clip, regurgitations is normally reduced or eliminated.

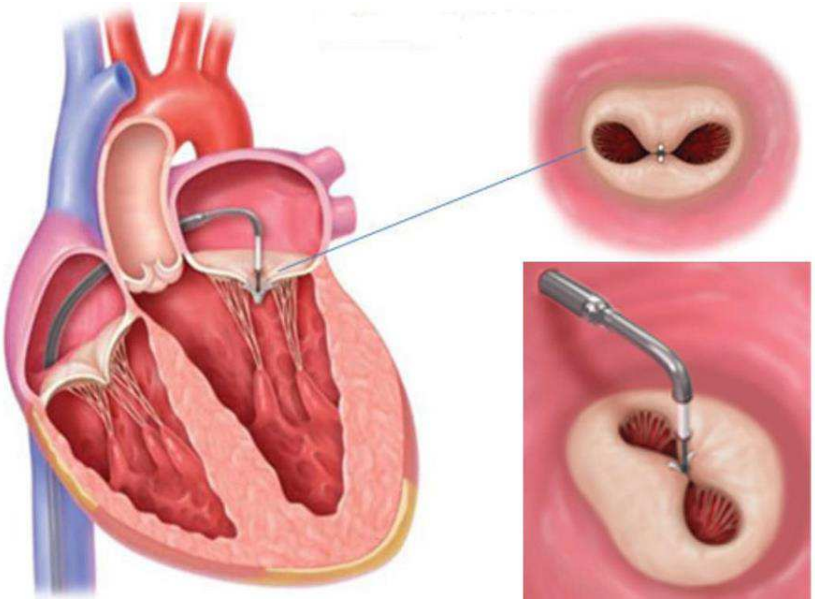

Figure 16: Mitral valve edge-to-edge repair with Mitral clip.

6. Cardiac fluid dynamics

Cardiac fluid dynamics is characterized by formation of vortices inside the heart chambers that interact with the surrounding tissues. The previously discussed electro-mechanical cycle is associated with the dynamics of blood flowing through the LV from mitral to aortic valve. The fluid dynamics inside the left ventricle is a very intense dynamical phenomenon and represents a fundamental element in cardiac function. The jet develops impulsively and within a few hundreds of second reaches speeds above the meter per second to enter a few centimeters long cavity. Then, the flow must reverse rapidly the direction of motion of 180° to re-direct toward the aorta where it will exit at the same high speed. The diastolic jet presents boundary layer separation from the tips of the mitral valve and immediately gives rise to a swirling motion within the cavity, as exemplified in figure 17.

The mitral orifice is slightly offset with respect to the ideal ventricular axis for which the jet redirects towards the lateral wall and gives rise to an asymmetrical swirling structure. The phenomenon is that of the formation of a vortex ring, both during the A-wave and during the E-wave, that then dissipates and stretched toward the outflow tract at the beginning of systole. The length of the jet, the development and dynamics of the vortex structure and the phenomena associated with its impact on the endocardial tissue depend on various physiological and pato-physiological factors. All these elements can make the difference that makes the vortex a stable structure

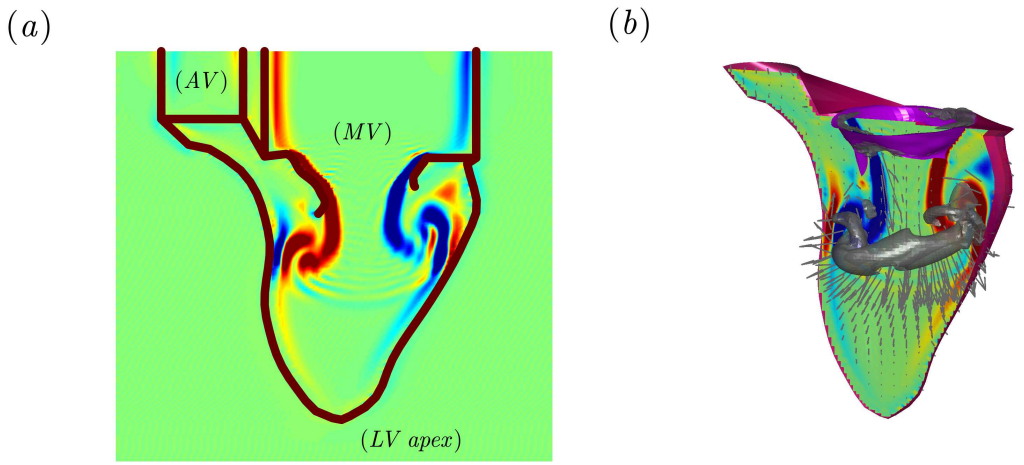

Figure 17: Numerical simulations during diastolic filling: (a) 2D vorticity formation, (b) 3D vorticity structure.

maintaining kinetic energy or an unstable structure that creates turbulence. All myocardial regions must work in harmonic synergy to push blood (considered as an incompressible medium) toward the aortic exit and for receive blood evenly, this because an incorrect timing of contraction or relaxation in one region of the wall it makes that the blood is pushed toward the other region, thus creating intraventricular pressure gradients that are not appropriate to create blood motion. Blood motion in the left atrium is driven by the pulmonary veins that enter the atrium transversally and when the mitral valve opens this possibly rotary motion flows down into the left ventricle in a funnel-like patters. To date there are only few inforations of right ventricular (RV) fluid dynamics, although RV function has been shown to be a major determinant of clinical outcome in numerous cardiac dysfunction. This few informations explain how the evaluation of RV geometry and blood motion is extremely challenging because of the anatomic and functional complexities of this chamber, which is difficult to visualize by two-dimensional imaging. The flow inside the RV is expected to form a complex three-dimensional (3D) vortex formation from the tricuspid valve as well as redirection of the jet towards the lateral pulmonary outflow; because the circulation system is a closed one, the volume of blood ejected from the RV must be equal to that ejected by the LV. During diastole, a vortex ring develops past the tricuspid valve and, given the transversal shape of the RV, one side of the vortex ring is close to the interventricular septum where it rapidly dissipates. During systole, the remaining portion of the vortex ring gets stretched toward the converging pulmonary outflow giving rise to a highly swirling outflow that may promote

proper mixing of the blood in the RV, thus prevents blood stagnation. The fluid dynamics inside the LV has a two fundamental aspects, the kinematic and the dynamic aspect.

6.1. Kinematic aspects

6.1.1. Flow transit analysis

The analysis of flow transit allows evaluating the properties of the washout and/or stagnation inside the LV chamber and to identify the origin of the regurgitant blood [24]. This analysis is performed here by solving a transport-diffusion equation for a passive scalar. Call *C(x,t)* the concentration of a passive marker of particles, the diffusion-transport equation is

$$\frac{\partial C}{\partial t} + \nu \cdot \nabla C = D\nabla^2 C; \tag{3}$$

that can be solved in parallel to the Navier-Stokes equation starting from the initial condition *C(x,0)=1*, in this way the individual blood particles present in the LV at end-systole are marked. The time evolution of C allows to verify the washout of the LV and if the blood ejected or regurgitated is made of blood that was previously present in the LV (marked by *C=1*) or that just arrived from the atrium *(C=0)*. In order to create a link with existing literature in 4D Flow MRI, we compute the LV wash-out in terms of the residual volume [39], this is defined by the blood volume that was present in the LV before diastole and that is not expelled during systole. The residual volume, normalized with the end-systolic volume (ESV), can be evaluated as

$$V_{residual} = \frac{1}{ESV} \int_{ESV} C dV. \tag{4}$$

The increase of residual volume corresponds to an increased possibility of blood aggregation.

6.2. Dynamic aspects

6.2.1. Hemodynamic forces

Hemodynamic forces are the forces that acting on blood to produce acceleration and depend on the details of intraventricular flow [82]. The global hemodynamic force vector was evaluated by computing the integral balance of momentum

$$\mathbf{F}(t) = \int_{V(t)} \rho \left(\frac{\partial \boldsymbol{v}}{\partial \mathbf{t}} + \boldsymbol{v} \cdot \nabla \boldsymbol{v} \right) dV, \tag{5}$$

where V(t) indicates the 3D LV flow domain and the integral is computed as the sum of values on each slice multiplied by the slice thickness; ***v(x,t)***

is the velocity vector field and ρ is the blood density [6]. The two terms inside the integral (5) represent the inertial and convective terms, respectively. They can be rewritten expressing the second term as momentum flux at the boundaries

$$\mathbf{F}(t) = \int_{V(t)} \rho \frac{\partial \boldsymbol{v}}{\partial \mathbf{t}} dV + \int_{S(t)} \rho \boldsymbol{v} \left(\boldsymbol{v} \cdot \boldsymbol{n} \right) dS = \boldsymbol{I}(t) + \boldsymbol{M}(t), \tag{6}$$

where *S(t)* is the boundary surface of the fluid domain, *V(t)*, and $\boldsymbol{n}$ is the outward unit normal vector. The two terms are synthetically indicated by the symbols $\boldsymbol{I}$*(t)* and $\boldsymbol{M}$*(t)*. Consider Cartesian coordinates with the z-axis directed from the LV apex (set at z = 0) to the center of the LV basal surface, the x-axis directed from the center of aortic outflow to that of the mitral orifice, the z-coordinate ranges from 0 to the LV height *H(t)* and *A(z,t)* indicates the transversal LV area at each level z such that the ventricular volume is

$$V(t) = \int_0^{H(t)} V(z,t) dz. \tag{7}$$

The inertial term on the right hand side of (6) can be computed exactly as

$$\boldsymbol{I}(t) = \rho V(t) \frac{dU(t)}{dt}; \tag{8}$$

where $\boldsymbol{U}$*(t)* is the velocity vector averaged in the entire LV cavity whose estimation allows one for $\boldsymbol{I}$*(t)*. For the z-component, at each level z, the balance of mass is

$$\frac{d}{dz}(V_z(z,t)A(z,t)) = -\frac{dA(z,t)}{dt}, \tag{9}$$

where $V_z(z,t)$ is the average velocity at level z. Eq. (9) can be immediately integrated to provide the z-component of the LV-averaged velocity to be inserted in (8)

$$U_z(t) = \frac{1}{V_t} \int_0^{H(t)} \left\{ \int_0^z -\frac{dA(s,t)}{dt} ds \right\} dz. \tag{10}$$

The x-component of the LV averaged velocity is due to the transfer of momentum along x from the mitral inflow to the outflow tract. The average longitudinal velocity, $V_z(z,t)$, that appears in (9) is associated to a purely radial velocity on the transversal plane,

$$V_r(t) = -\frac{r}{2} \frac{dV_z}{dz}, \tag{11}$$

that has no average component along x. The inflow/outflow fluid velocity is predominantly oriented along the z-direction and approximately symmetric with respect to the xz-plane, then the vertical velocity is expressed as the sum of its mean value $V_z(z,t)$ and an asymmetric component $V_z^{(1)}(z,\vartheta,t)$ such that $v_z(x,y,z,t) \approx V_z(z,t) + V_z^{(1)}(z,\vartheta,t)$, where ϑ is the circumferential coordinate, defined by $x = r\ cos\vartheta$, $y = r\ sin\vartheta$ with $r = \sqrt{x^2+y^2}$ and therefore $V_z^{(1)}(z,\vartheta,t)$=$V_z^{(1)}(z,t)cos\vartheta$, using the function $cos\vartheta$ as asymmetry-weighting function.
The conservation of mass can be recast in terms of asymmetric components only

$$\frac{\partial V_x^{(1)}}{\partial x} + \frac{\partial V_y^{(1)}}{\partial y} = -\frac{\partial V_z^{(1)}}{\partial z} cos\vartheta; \tag{12}$$

where the superscript (1) is used to indicate all components associated with the nonsymmetric velocity $V_z^{(1)}$. The simplest in-plane velocity field that satisfies (12) is

$$\begin{aligned} V_x^{(1)}(r,\vartheta\, z) &= \left(\frac{2}{3}R - \frac{1}{2}r - \frac{1}{6}r\cos 2\vartheta)\right)\frac{dv_z^{(1)}}{dz}; \\ V_y^{(1)}(r,\vartheta\, z) &= -\frac{r}{6}\sin 2\vartheta \frac{dv_z^{(1)}}{dz}. \end{aligned} \tag{13}$$

The solution (13) included the integration constant to have zero radial velocity at the boundary, assumed approximately circular of radius $R(z,t) = \frac{3}{2A}\int_A r dA$, and its integration over the cross-section and along the LV axis allows estimating the x-component of the velocity averaged in the LV

$$\begin{aligned} U_x(z,t) = &\frac{1}{3V(t)}\int_0^{H(t)} A(z,t)R(z,t)\frac{dv_z^{(1)}}{dz}dz \\ &+ \frac{1}{V(t)}\int_0^{H(t)} V_{xw}(z,t)A(z,t)dz; \end{aligned} \tag{14}$$

the last term in (14) was added to account for the possible net translation of the LV boundary where $\mathbf{V}_w(z,t)$ is the average velocity of the LV boundary at level z. Formula (14) requires the evaluation of the term $\frac{dv_z^{(1)}}{dz}$. Assume the simplest case of a linear decrease of the flux, from the basal profile to the null value at the apex, writing a relation formally analogous to (9)

$$\frac{d}{dz}(v_z^{(1)}A(z,t)) = \frac{v_z^{(1)}(H)A(H)}{(H)(t)}, \tag{15}$$

from which

$$\begin{aligned}\frac{dv_z^{(1)}}{dz}(t) &= v_z^{(1)}(H,t)\frac{A(H,t)}{H(t)}\frac{d}{dz}\left(\frac{z}{A(z,t)}\right)\\ &= \frac{v_z^{(1)}(H,t)}{H(t)}\frac{A(H,t)}{A(z,t)}\left(1-\frac{z}{A(z,t)}\frac{dA}{dz}\right),\end{aligned} \tag{16}$$

Equation (16) into (14) gives the estimate of the x-component of the velocity averaged in the LV

$$\begin{aligned}U_x(t) = \frac{1}{3V(t)}v_z^{(1)}(H)\frac{A(H)}{H(t)}\int_0^{H(t)} R(z,t)\left(1-\frac{z}{A(z,t)}\frac{dA}{dz}\right)dz + \frac{1}{V(t)}\\ \times\int_0^{H(t)} V_{xw}(z,t)A(z,t)dz.\end{aligned} \tag{17}$$

This equation requires only the knowledge of the asymmetric velocity at the basal level, $z = H$, at every instant. Both the average velocity V_z and the asymmetric component $V_z^{(1)}$ at the LV base can be obtained by measurements of inflow and outflow. For completeness, we consider the y-component $U_y(t)$, which is only due to the transversal motion of the wall

$$U_y(t) = \frac{1}{V(t)}\int_0^{H(t)} V_{yw}(z,t)A(z,t)dz. \tag{18}$$

The convective term $\boldsymbol{M}(t)$ in (6) is evaluated from the knowledge of the velocity distribution on the lateral wall surface, S_{lat} , and on the basal surface.The normal vector $\boldsymbol{n}$ is computed from the instantaneous surface geometry to give the flux of momentum on the lateral wall. On the valvular plane, assumed in first approximation with normal $\boldsymbol{n} = [0\ 0\ 1]$, the z-component of the velocity is approximated by

$$v_z(x,y,H,t) \approx V_z(H,t) + v_z^{(1)}(H,t)cos\vartheta. \tag{19}$$

In the same approximation, the x-component of the velocity is given by (11) and (13)

$$v_z(x,y,H,t) \approx -\frac{r}{2}\frac{dV_z}{dz}cos\vartheta + \left(\frac{2}{3}R - \frac{1}{2}r - \frac{1}{6}r\cos 2\vartheta)\right)\frac{dv_z^{(1)}}{dz} + V_\Gamma(t), \tag{20}$$

where the last term is included to account for the circulation given by the diastolic vortex formation in the LV; this term is zero on average but is

normally present at the base. Eq. (20) can be recast using (9) and (18) as

$$v_x(x,y,H,t) \approx \frac{r}{2}\frac{1}{A}\left(V_z\frac{dA}{dz}+\frac{dA}{dt}\right)cos\vartheta + \frac{1}{A}\left(\frac{2R}{3}-\frac{1}{2}r-\frac{1}{6}r\cos 2\vartheta\right)\left(\frac{A}{H}-\frac{dA}{dz}\right)v_z^{(1)}+\frac{\Gamma(t)}{2R} \tag{21}$$

where $\Gamma(t)$ is the vortex circulation. The circulation obeys the vortex formation process due to the roll-up of the mitral shear layer, of intensity $2v_z^{(1)}$, and a linear decay process,

$$\frac{d\Gamma}{dt} = \begin{cases} 2{v_z^{(1)}}^2 & -\frac{\Gamma}{\tau}, \quad \frac{dV(t)}{dt} > 0 \\ 0, & \frac{dV(t)}{dt} < 0 \end{cases} \quad ; \tag{22}$$

where the dissipation decay time is taken $\tau = 0.1T$ to ensure a complete vortex dissipation within less than one third of the heartbeat in normal subjects as commonly observed. Performing the integral in (6) involving (19) and (21) provides the following

$$\mathbf{M}(t) = \rho\int_{S_{lat}} \boldsymbol{v}\, v_n dS + \rho \begin{bmatrix} V_z v_z^{(1)}\frac{R}{3}\left(\frac{A}{H}-\frac{1}{2}\frac{dA}{dz}\right)+\frac{R}{6}\frac{dA}{dt}v_z^{(1)}+V_zV_{xw}A+V_z\Gamma(t)\frac{A}{4R} \\ V_zV_{yw}A \\ \left(V_z^{(1)}+\frac{1}{2}{v_z^{(1)}}^2\right)A. \end{bmatrix}; \tag{23}$$

where the first term on the right hand side is the flux of momentum on the lateral wall and the second terms represent that through the base with all quantities.

6.2.2. Intraventricular pressure gradients

The intraventricular pressure gradient field (IVPG), ∇p, plays an fundamental role in LV function [85]. The ∇p field is the dynamic counterpart of the intraventricular velocity field, *v(x,t)*. The Navier–Stokes equation can be rearranged as

$$\nabla p = -\rho\left(\frac{\partial v}{\partial t}+\boldsymbol{v}\cdot\nabla\boldsymbol{v}\right)+\mu\nabla^2\boldsymbol{v}, \tag{24}$$

this equation is essentially equivalent to (5) and differs only for the viscous friction (last term) that is usually nearly negligible along the short intra-chamber paths. IVPG is therefore essentially made of the sum of the inertial (local) acceleration and the convective term.

It is sometime suggested to directly compute the relative pressure field p by solving the Poisson's equation

$$\nabla^2 p = -\rho\nabla\cdot(\boldsymbol{v}\cdot\nabla\boldsymbol{v}). \tag{25}$$

obtained by taking the divergence of (24), although care must be taken in imposing appropriate boundary conditions [19, 33, 47] because (25) is second order and the average pressure gradient (tri-linear terms in pressure) is solution of the homogeneous Laplace operator and its value follows from the boundary conditions only.

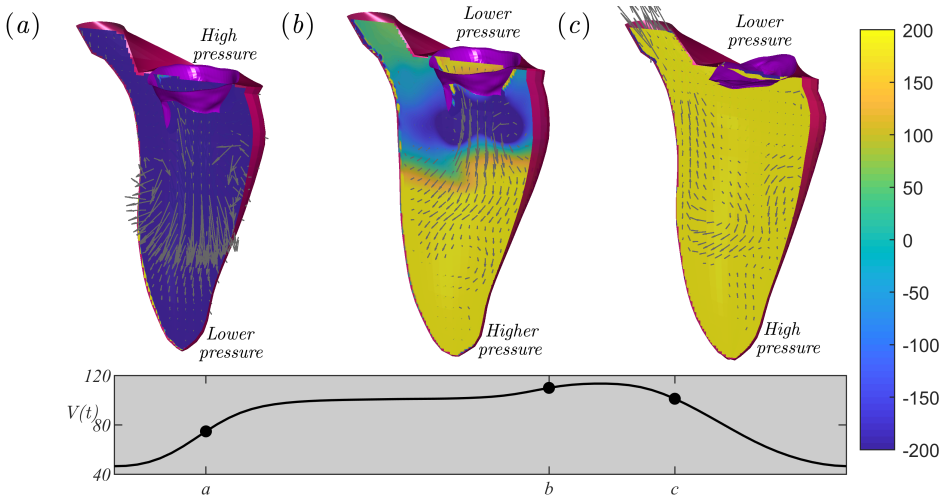

Figure 18: Relationship between relative pressure field and flow acceleration, shown by the direction of the arrows, during: (a) Early diastole, (b) Late diastole, (c) Early systole. Each picture shows the color-map of the pressure as by the color scale on the right (notice the natural scale for kinematic pressure is cm2=T , T is the heartbeat; 200 units correspond approximately to 20Pa or 0:15mmHg).

IVPGs drive blood motion during both ventricular ejection and ventricular filling as shown in figure 18. They represent the ultimate result of LV deformation and play a central role in cardiac function that governs blood flow. Moreover, flow-mediated forces influence and participate to cardiac adaptation in presence of pathologies.
The usage of hemodynamic forces has been recently renewed with the introduction of methods able to estimate them non-invasively by medical imaging and with much promising results as described in this recent publications[27, 28].

7. Computational model

7.1. Geometric descriptions

The LV is a closed cavity bounded by the lateral LV wall and by the basal surface that contains the mitral and aortic orifices representing the flow inlet and outlet, respectively. The geometry of the lateral LV wall can be obtained from several imaging technologies like CT, MRI or Echocardiography. Different modalities differ for the time and spatial resolution, for providing multi-slice or full 3D acquisitions, and for the availability in the clinical environment. Different software solutions are usually available in the different modalities that help to identify the LV internal surface by user-assisted interactive procedures. Whatever the technology, the typical results is a dynamic cast of the moving LV cavity that we eventually described by the positions vector $\mathbf{X}(\vartheta, s, t)$, where the structured parametric coordinates, (ϑ, s), run along the circumference and from base to apex, respectively, t is time. The usage of structured coordinates here was preferred for easier manipulation; however, unstructured (e.g. triangular) descriptions could be equally used. The position vector marks LV material points and their velocity is obtained by time differentiation.

The MV geometry can also be extracted from the same imaging technologies relying on dedicated software tools for valvular delineation. Commonly, the time resolution does not allow to reliably visualize and extract the MV geometry other than in the fully-open (peak diastole) and fully-closed (during early systole) configurations. The geometry of a normal MV, in closed and open configurations, is shown in figure 19 as extracted from CT [108]. Whatever the imaging technology adopted, the 3D mesh of the leaflets' surface in the two configurations was reorganized in terms of an analogous set of structured parametric coordinates, (ϑ, s), along the circumference and extending from the annulus to the trailing edge. Additional reference measurement must then be obtained for placing the extracted MV geometry in the proper position relative to LV. This step is simplified when both LV and MV geometries are extracted from the same image set such that they are described with a common system of coordinates ensuring their automatic relative positioning. The most feasible imaging solution to this aim is given by Trans-Esophageal 3D Echocardiography (3D TEE), that is commonly used for visualization of valvular diseases, although image quality is not always optimal. However, imaging technology is rapidly evolving and segmentation options -that are out of the scope of this work- are continuously growing and improving the feasibility of reliable geometric reconstructions.

When the valve shape is recorded at two instants corresponding to the closed and the open configurations, say at $\varphi = 0$ and $\varphi = \pi/2$, respectively,

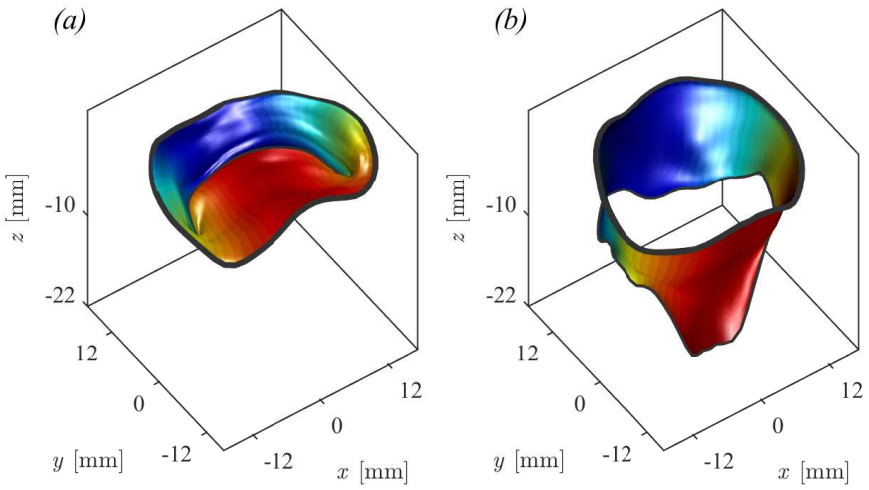

Figure 19: Normal mitral valve surface: (a) closed systolic configuration, (b) fully open diastolic configuration; the color (red=anterior leaflet, blue=posterior leaflet) indicates the local influence of individual opening angles in a model with two degrees of freedom.

where φ is the generic degree of local opening, the valve geometry at intermediate positions must be reconstructed. This is performed here as follows, at an intermediate degree of opening, φ, the position of the annulus ($s = 0$) is evaluated by linear interpolation between the closed and open configurations; then, starting from the annulus, the local metrics and the local normal is estimated from linear interpolation and integrated along the radial direction s. This simple approach can be improved when the valve geometry or other information is available at additional intermediate stages.

The MV geometry is eventually described as $\mathbf{X}_v(\vartheta, s, \varphi)$, where φ is a time-varying function that corresponds to the degree of opening. It is important to remark that at this stage there is not limitation on the number of degrees of freedom allowed for valvular movement because, theoretically, the degree of opening can be a function $\varphi(\vartheta, s, t)$. In the application presented in §9, we first described the valve with one degree of freedom assuming $\varphi(t)$ to be a constant over the valvular surface, then we considered the two leaflets moving independently with two degrees of freedom by modulating the function as

$$\varphi(\vartheta, s, t) = \varphi_2(t) + (\varphi_1(t) - \varphi_2(t))\frac{(1 + cos\vartheta)}{2}, \tag{26}$$

where $\varphi_1(t)$ is the opening angle of the long (anterior) leaflet and $\varphi_2(t)$ the short (posterior) leaflet. The function (26) is displayed in figure 19 to show the relative influence of the two leaflets in the valvular geometry.

The aortic valve at the outlet is modeled by a simple open/close behavior with no leaflets. The annulus of the MV and that of the aortic valve are then connected to the annulus of the LV valve by an automatic linear connection procedure to close the basal surface of the LV around the valves. The overall geometry of the normal LV is shown in figure 20.

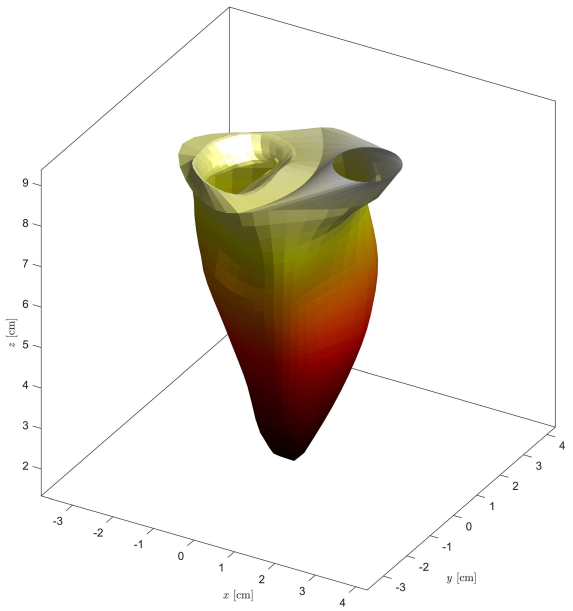

Figure 20: Complete geometry of ventricle, mitral valve (with open leaflets) and basal surface including the open aortic orifice. Color is modulated with the vertical coordinate.

7.2. Fluid dynamics

The fluid dynamics is evaluated by numerical solution of the Navier-Stokes and continuity equations

$$\frac{\partial \boldsymbol{v}}{\partial t} + \boldsymbol{v} \cdot \nabla \boldsymbol{v} = -\nabla p + \nu \nabla^2 \boldsymbol{v}, \tag{27}$$

$$\nabla \cdot \boldsymbol{v} = 0; \tag{28}$$

where $\boldsymbol{v}(t, \mathbf{x})$ is the velocity vector field, $p(t, \mathbf{x})$ is the kinematic pressure field and ν is the kinematic viscosity (assumed $0.04 cm^2/s$). Blood is intentionally assumed as a Newtonian fluid. Indeed, blood is a mixture of elastic corpuscular elements in an aqueous solution and either Newtonian or non-Newtonian models are approximate. However, the influence of corpuscular or non-Newtonian behavior is very small in the heart chambers [70] and it is

negligible when compared with the limited accuracy of the clinical data used as input.

The numerical solution is based on an immersed boundary method previously used in numerous studies [32, 31, 67, 68], which is briefly recalled here. Equations are solved numerically in a rectangular domain using a staggered, face-centered regular Cartesian grid where spatial derivatives are approximated by second-order centered finite differences. Time advancement is achieved using a fractional step method as follows. Velocity is preliminarily advanced in time by the Navier-Stokes equation (27) using a low-storage, third-order Runge-Kutta explicit scheme. This preliminary velocity, say $\hat{\boldsymbol{v}}$, that does not satisfy the incompressibility constraint (28), is corrected by adding a potential field $\delta\boldsymbol{v} = \nabla q$, such that $\boldsymbol{v} = \hat{\boldsymbol{v}} + \delta\boldsymbol{v}$ satisfies the continuity and the boundary conditions. The correction potential is found by solution of the Poisson equation

$$\nabla^2 q = -\nabla \cdot \hat{\boldsymbol{v}}; \tag{29}$$

and pressure is updated with q accordingly. Boundary conditions at the edge of the computational box are set periodic in the x and y directions, while they are zero pressure and normal velocity on the upper and lower ends along z, respectively. The 2D Fourier decomposition permits fast solution of the Poisson equation (29) as a sequence of tridiagonal systems for each harmonic.

Boundary conditions are also set on the moving immersed boundaries. These comprise the LV lateral wall, the basal wall and the MV leaflets, as defined above in §7.1. In addition, two cylindrical regions are added extending from a region around the mitral valve (bounded by the LV edge on the mitral side and the curve separating MV and aortic valve) and from around the aortic valve to the upper edge of the computational domain; these additional boundaries represent surrogates of atrium and aorta. They are included for numerical convenience to avoid interference between the outflow and the inflow outside the LV and to avoid nonphysical sharp corners at the edge of the LV basal plane; the potential influence of these on the intraventricular flow is evaluated in §8.1 dedicated to numerical verifications. Following the IBM approach, the boundary conditions are imposed on the intermediate velocity $\hat{\boldsymbol{v}}$ at the end of the Runge-Kutta time advancement before imposing the correction obtained by (29) [30].

Given that the immersed boundaries do not coincide with the computational grid, a local interpolation scheme is commonly used to transfer the precise boundary conditions at the surrounding computational points [70, 71]. However, in clinical applications, the position of the LV boundaries is extracted by semi-visual assessments from images whose resolution

is lower than the computational grid; therefore, the uncertainty regarding the boundary position is commonly larger than the grid-size. Anatomically, the LV endocardium presents small-scale elements that are not resolved in imaging and are not reproduced in the extracted geometry. Finally, living geometries present continuous physiological variations and any instantaneous measurement must be considered within a range of its natural variability. Thus, in the context of simulations based on images and finalized to clinical applications, the time-consuming interpolation scheme can be cut down by simply closing all the faces of the cell containing the immersed boundary and setting a velocity equal to the average of the points falling in that cell. A computational step that can be performed with extreme efficiency. Additionally, when computing the Navier-Stokes equation at the closed cells corresponding to soft tissue, the cell viscosity is artificially increased to its maximum stable value

$$\nu_{IB} = \frac{1}{2\Delta t}\left(\frac{1}{\Delta x^2}+\frac{1}{\Delta y^2}+\frac{1}{\Delta z^2}\right)^{-1}. \tag{30}$$

This simplification avoids unrealistic sharp-edge boundaries, and improves the numerical convergence by preventing from the creation of small scales of sub-grid size. Physically, the spatial accuracy is still well above the uncertainties and the variability of the boundaries that are somehow "blurred" about the closed cells. The influence of using the approximation (30) for a hypothetically smooth boundary is analyzed in §8.2 below.

7.3. Valve dynamics

The LV geometry obtained from imaging expands and contracts during the cardiac cycle and represents the driving force for blood motion. Differently, the dynamics of the mitral valve leaflets is driven by the interaction with flow. We consider here a simplified model of interaction between flow and MV that does not involve detailed tissue material properties. The valve is assumed as a membrane that opens with the flow with few degrees of freedom under the constraint of maintaining the shape consistent with that extracted from images as described in §7.1. In general, the valve geometry is described by its coordinates $\mathbf{X}_v(\vartheta, s, \varphi_i)$ where the parameters $\varphi_i(t)$, with $i = 1, 2 \dots N$, represent the N degrees of freedom modulating valvular dynamics. The valve geometry is thus known once the value of each parameter is known.

The statement that the valve opens with the flow translates mathematically in the congruence condition that the normal component of the valve

velocity matches that of the fluid

$$\boldsymbol{v} \cdot \boldsymbol{n} = \sum_{i=1}^{N} \left(\frac{\partial \mathbf{X}_v}{\partial \varphi_i} \cdot \boldsymbol{n} \right) \frac{\partial \varphi_i}{\partial t}; \tag{31}$$

where $\boldsymbol{n}$ is the local normal to the valvular surface. Equation (31) applies in general at every point of the continuous valvular surface. However, the valve contains only a finite number N of degrees of freedom whose dynamics, $\frac{\partial \varphi_i}{\partial t}$, describes the constrained leaflets' motion. In this case a solution in weak form of (31) can be obtained by minimization of its square root error integrated over the entire surface A_v of the valve

$$\iint_{A_v} \left\{ \boldsymbol{v} \cdot \boldsymbol{n} - \sum_{i=1}^{N} \left(\frac{\partial \mathbf{X}_v}{\partial \varphi_i} \cdot \boldsymbol{n} \right) \frac{\partial \varphi_i}{\partial t} \right\}^2 dA = min. \tag{32}$$

The least square minimization is recast in the form of a linear system

$$\sum_{j=1}^{N} \left[\iint_{A_v} \left(\frac{\partial \mathbf{X}_v}{\partial \varphi_i} \cdot \boldsymbol{n} \right) \left(\frac{\partial \mathbf{X}_v}{\partial \varphi_j} \cdot \boldsymbol{n} \right) dA \right] \frac{\partial \varphi_j}{\partial t} = \iint_{A_v} (\boldsymbol{v} \cdot \boldsymbol{n}) \left(\frac{\partial \mathbf{X}_v}{\partial \varphi_i} \cdot \boldsymbol{n} \right) dA, \tag{33}$$

on the N unknowns $\frac{\partial \varphi_i}{\partial t}$, $i = 1, 2 \ldots N$, that specify the motion of the valve due to the blood flow starting from the initial closed configuration $\varphi_i(0) = 0$. The matrix of the system (33)

$$M_{ij} = \iint_{A_v} \left(\frac{\partial \mathbf{X}_v}{\partial \varphi_i} \cdot \boldsymbol{n} \right) \left(\frac{\partial \mathbf{X}_v}{\partial \varphi_j} \cdot \boldsymbol{n} \right) dA, \tag{34}$$

represents the mutual influence of the different degrees of freedom, it is a diagonally-dominant and symmetric matrix and ensures that the system is well conditioned. The model (33) was introduced here with reference to the specific application for cardiac valves. Nevertheless, the mathematical framework is rather general and not bounded to this application. It works with an arbitrary geometry, here called $\mathbf{X}_v$, whose possible configurations are described by a finite number of degrees of freedom each one quantified by the corresponding parameter, that in this case are the φ_i's. These degrees of freedom may represent spatially distinct elements, as it is in this case, or they could represent parameters of a spectral representation or even mixed descriptions. In the limit of $N \to \infty$ this model represents a totally loose surface where all points moves as if they were independent particles. When N is small, this approach to valve dynamics represents a modal decomposition where the overall motion is simplified in a few modes (degrees of freedom). It

must be emphasized that the model (33) represents a drastic simplification with respect to a complete FSI approach because the equations governing the deformation of the tissue are not explicitly included. Thus this model neglects the forces due to elastic recall and reproduces the asymptotic behavior where the valve moves with the flow with no elastic resistance other than the constraint of moving in the prescribed set of geometrical configurations deducted from images, as shown in figure 21, and that agrees with that obtained from the clinical images. The approximation of this model with respect to a FSI is paid back by the advantage of allowing simulations solving a simple linear system and without requiring a detailed definition of tissue properties that cannot be measured in vivo.

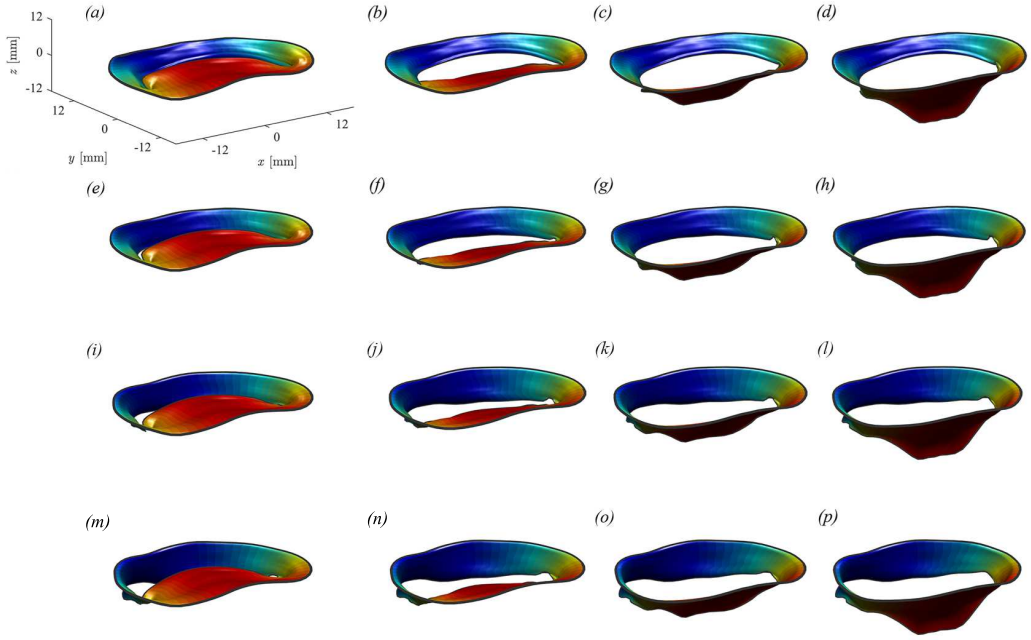

Figure 21: Geometry of a healthy MV for different degrees of opening of the two independent leaflets. (a) φ_1=0,φ_2=0; (b) φ_1=π/6,φ_2=0; (c) φ_1=π/3,φ_2=0; (d) φ_1=π/2,φ_2=0; (e) φ_1=0,φ_2=π/6; (f) φ_1=π/6,φ_2=π/6 ; (g) φ_1=π/3,φ_2=π/6; (h) φ_1=π/2,φ_2=π/6; (i) φ_1=0,φ_2=π/3; (j) φ_1=π/6,φ_2=π/3; (k) φ_1=π/3,φ_2=π/3; (l) φ_1=π/2,φ_2=π/3; (m) φ_1=0,φ_2=π/2; (n) φ_1=π/6,φ_2=π/2; (o) φ_1=π/3,φ_2=π/2; (p) φ_1=π/2,φ_2=π/2.

The dynamics described by the system (33) represents the asymptotic limit of the loosest MV within the prescribed set of geometric configurations. As such it can also represent a reference ground for the introduction of additional factors accounting for elastic resistance based on clinical observables. These could depend on the elastic deformation through global coefficients associated to each individual degree of freedom, similarly to what introduced

in [17] for a former model limited to one degree of freedom. The additional coefficients could then be calibrated to additional measurements when these are available.

The system (33), that gives $\frac{\partial \varphi_i}{\partial t}$, is evaluated in parallel to the Navier-Stokes equation (27), that gives $\frac{\partial \boldsymbol{v}}{\partial t}$ during the Runge-Kutta time advancement of fluid velocity and valve motion. At every time step, the fluid boundary conditions are imposed at all immersed boundaries including every point of the valve position based on the instantaneously computed valve motion, this feedback completes the interaction between tissue and blood flow.

Finally, the aortic valve, which is downstream of the LV flow field, is modeled as a simple orifice with a flat surface that is either open or closed. Aorta is considered open when the mitral valve is closed and the normal velocity, averaged over the position of the aortic valve surface, prior to setting the boundary conditions, is directed outwards. This way, it is not necessary to prescribe the open or closed state of the aortic valve by global considerations because the exact instants of start-end of systole and diastole can be difficult to define accurately in pathological conditions.

8. Verifications

8.1. Numerical verification

The overall numerical implementation was extensively validated in previous studies. However, simulations of coupled problems involving both fluid and solid elements are often challenging and results can be dependent on space and time resolution even when the convective and diffusive stability criteria are fulfilled. Therefore, we preliminarily performed an extensive validation of the numerical method to verify the sensitivity of results to specific numerical choices. To this aim we considered a single degree of freedom valve model and a simple LV geometry used in a previous study [31]. We show here the results for a same system simulated with a basic grid made of $128 \times 128 \times 160$ points and 2048 time steps in one heartbeat, a refined grid $192 \times 192 \times 240$ points and 3072 time steps, and the same eliminating the model for atrium and aorta thus allowing inflow/outflow to communicate in the space surrounding the LV. The coarser parameters were previously demonstrated to ensure convergence of flow solution with valves modeled as orifices without moving leaflets [32, 67, 68]. We monitored here the MV opening angle, that represents the result of the interaction between flow and solid elements, for which minor instantaneous differences can trigger progressively increasing discrepancies.

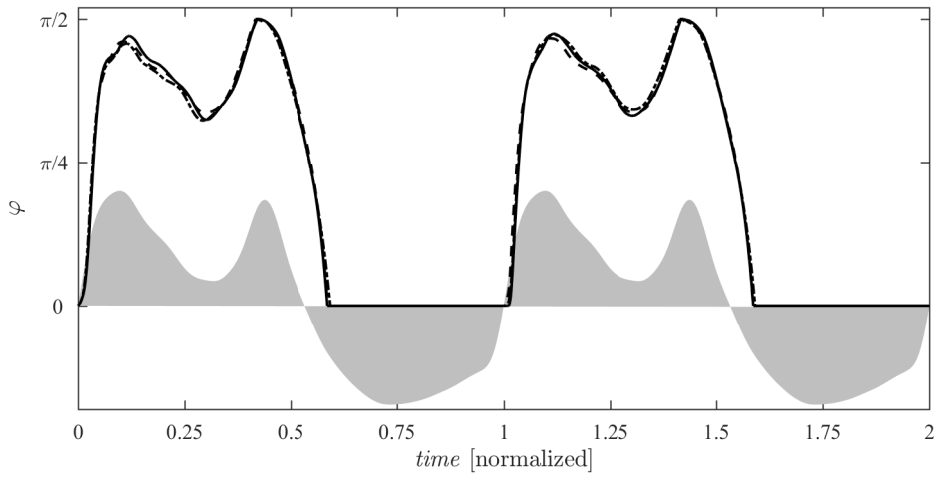

Figure 22: Time course of the valve opening angle in three cases with different resolution and removing the model of atrium and aorta upstream and downstream of the valvular plane, respectively. The continuous line represents basic grid made of $128 \times 128 \times 160$ points; the dashed line represents a refined grid $192 \times 192 \times 240$ points; and the dashed point line represents the same, only eliminating the model for atrium and aorta. The shaded gray area represents the volume rate for reference (not to scale).

The results of leaflet dynamics, reported in figure 22, are very similar within this range of spatial and temporal resolution and are not influenced by the presence of atrium/aorta models, which only reduces phenomena of vortex interaction outside the LV. These results demonstrate the robustness of the coupled computational model, possibly because it is based on integral balances. The flow fields are essentially identical in the three cases.

8.2. Effect of immersed boundary viscosity

The IBM method for flow simulation presented in §7.2 proposes to use an amplification of the viscosity coefficient, equation (30) when the fluid equations are evaluated in correspondence of the immersed solid elements. The appropriateness of such a method was suggested when the uncertainty in the boundary position is larger than the grid size because the method spreads the boundary condition over the computational cell.

We perform here a comparative analysis between numerical solutions obtained with and without the introduction of equation (30) to verify the influence of this assumption with respect to considering a smooth boundary. The comparison is carried out in the case of a normal LV (details about this case are described below in §9).

Results show that the flow is largely unaffected by the introduction of this artificial boundary viscosity, with the only difference limited to the presence of very small scales that are sometime smoothed out; as an example, figure 32 shows the flow fields at the peak of the E-wave in the two cases. The comparative analysis provides some support that this approach does not introduce non-physical phenomena other than smearing out grid-size fluctuations near the boundaries, a phenomenon that is meaningful when the position of the boundary is not known with accuracy.

In particular, it can be useful in presence of sharp boundaries that are a result of segmentation algorithms and whose details may not be physically realistic. In such case, the immersed boundary approach can give rise to similarly unrealistic small scales in fluid flow. To better describe this point, figure 23 shows three insets with the enlargement of the vorticity field near sharp boundaries computed with and without artificial viscosity at the solid cells. The zero thickness boundaries sometime produces fluctuations of length equal to the grid size that are a consequence of the jump across the solid cell. Such fluctuations are significantly reduced when the viscosity is enhanced at boundary cells. It must also be reminded that this artificial viscosity is applied only to those computational cells that contain the solid elements. Such cells are treated as fluid cells during the IBM solution and the flow equation are solved therein during the intermediate time-advancement steps when

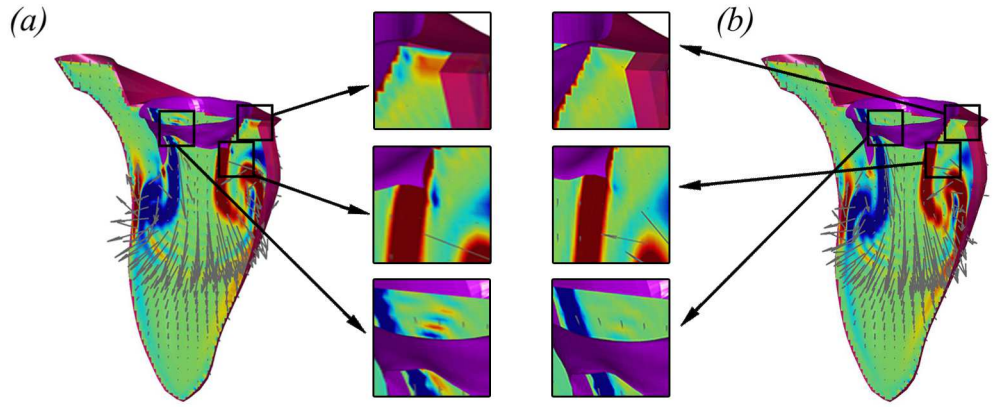

Figure 23: Details of the flow fields in a normal LV at peak E-wave computed (a) with regular viscosity, (b) with the enhanced viscosity at the immersed boundary using identical numerical parameters. Each picture shows the color-map of the normal vorticity (red to blue from -200 to 200, units equal to the inverse of the heartbeat period) and the velocity vectors (every 4 grid points) on a longitudinal plane crossing the center of MV, of aorta and LV apex. The three panels report enlarged views of specific regions next to edges of the immersed boundary.

discontinuities can influence nearby fluid cells. The enhanced viscosity essentially reduces this influence and has the main effect of spreading the presence of the solid to the entire cell. At the same time, this approach can improve the stability of the numerical solution in presence of sharp boundaries; therefore, it may reduce the need of smoothing procedures when preprocessing the borders obtained from image segmentation tools.

Therefore, the usage of equation (30) appears appropriate when the definition of the anatomical boundaries is available with a resolution that is comparable to the grid size or when such boundaries are described with unphysical sharp edges.

8.3. Comparison with a FSI solution

The computational model is preliminarily evaluated in an idealized geometry where a FSI solution is available from a study in literature for a healthy LV with a simplified natural MV made of two separate leaflets [70]. The LV presents a volumetric reduction of 60% with respect to its maximum size. This corresponds to a peak Reynolds number $Re = \frac{v_p D_a}{\nu} \simeq 4200$, where v_p is the maximum velocity averaged across the mitral annulus of diameter D_a, and a Strouhal number $St = \frac{D_a}{v_p T} \simeq 2.9 \times 10^{-2}$ and T is the heartbeat duration. It is worthwhile to remark that the peak velocity lasts lasts only for a small fraction of the cycle and the average value of the Reynolds number is about 660 and of Strouhal 0.18. The MV tissue properties are assumed in

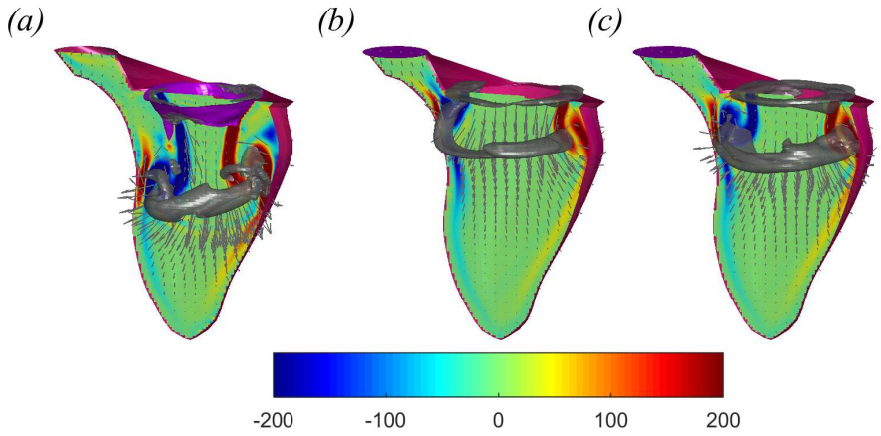

Figure 24: Flow fields in a normal LV at peak E-wave computed with (a) and without (b) the enhanced viscosity at the immersed boundary. Each picture shows the color-map of the normal vorticity (red to blue from -200 to 200, units equal to the inverse of the heartbeat period) and the velocity vectors (every 4 grid points) on a longitudinal plane crossing the center of MV, of aorta and LV apex; the three-dimensional gray surfaces represents iso-surfaces of the λ_2 parameter.

the FSI solution as those of an isotropic linearly-elastic membrane of uniform (small) thickness, which includes mass and bending stiffness [29, 70]. For the present comparison, mimicking the procedure proposed for application to clinical data, the LV geometry coming from the FSI numerical solutions and the MV geometry in the open and closed configurations are used as inputs for the present model. The MV geometry is here described by 2 degrees of freedom that exactly identify the individual leaflets.

It is important to remark that the two systems are not directly comparable. The FSI simulation is obtained with a specific set of values for the valvular tissue properties, whereas such elastic properties are not part of the present asymptotic model where the leaflets motion is not subjected to elastic resistance. Therefore, this comparative analysis aims to verify the consistency of the asymptotic model and cannot purse to a one-to-one comparison as the physical systems are different.

Computations are performed starting from rest in both models and are limited to the first diastole. Figure 25a-c shows the velocity fields obtained by the FSI solution corresponding to three time instants (peak of the E-wave, stasis between E and A waves, and peak of A-wave), and are compared with those obtained at the same instants with the present model (figure 25d-f). Both models show similar gross features, with the entering jet displaced towards the lateral wall (on the right side) in figure 25a,d, a weak downward flow pattern about the valve leaflets in figure 25b,e, and a straight jet in figure

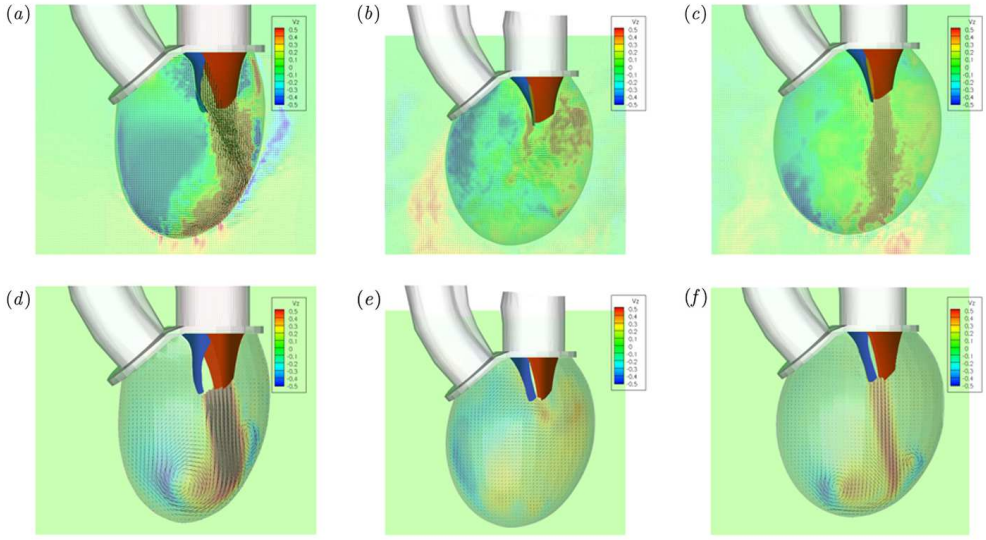

Figure 25: Snapshots of the velocity field in the central transversal plane, $y = 0$, for the idealized system introduced in [70]. Results from the FSI numerical study (a,b,c) and from the present model (d,e,f). The flow fields corresponds to peak E-wave (a,d), diastasis (b,e), peak A-wave (c,f); each picture reports the velocity vectors and the colormap of the vertical velocity. (Due to different graphical representations, the color pattern in (d,e,f) results smoother and cropped inside the valve.)

25*c,f*. The two numerical results differ mainly for the apparent different degree of smoothness. This is partly imputable to the different numerical techniques; moreover, in order to create the same graphical representation, the present results were resampled from the staggered grid with (2x2 filtering) and the flow field inside was cropped.

Some differences are also a consequence of differences in the valvular dynamics. A first comparison of the motion of the anterior leaflet in the two cases is reported in figure 27 using the same representation of the original FSI reference [70]; the motion of the posterior leaflet, not reported here, shows analogous behavior although with excursions that are about 20 times smaller. The curves suggest that the present model corresponds to a system with looser leaflets: the leaflet opens more rapidly during the E-wave, it present a slightly larger closure during diastasis, and opens completely during the E-wave when the elastic leaflets of the FSI model do not reach complete opening.

Another quantitative comparisons is reported in figure 26 in terms of metrics more directly related to valvular function like the projected opening

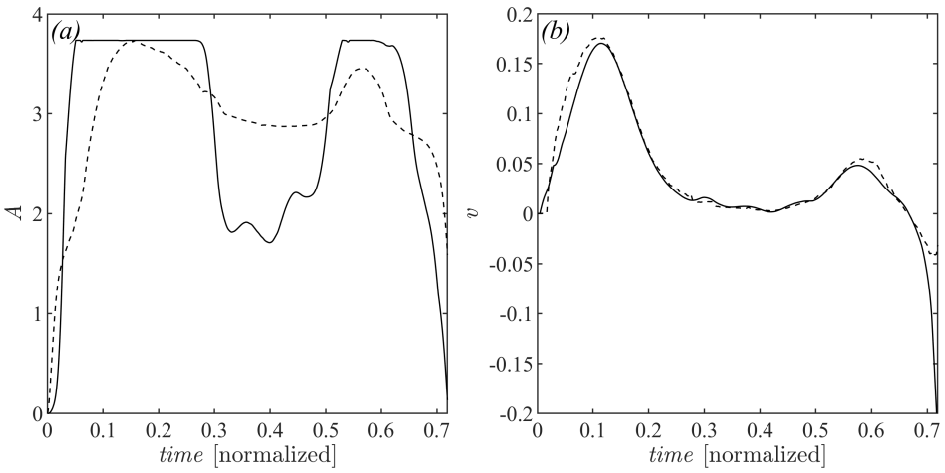

Figure 26: Time evolution of the projected valve opening area (a), and of the mean cross-valve vertical velocity (b): continuous line for the present asymptotic model, dashed line for the elastic FSI model.

area $A(t)$, and the average cross-valve velocity $v(t)$ (computed as Q_e/A, where Q_e is the effective volume rate across the valvular opening, as defined later in equation (35). The comparison between the opening areas in figure 26 confirms that the present model corresponds to a looser valve that responds more rapidly both during opening and closure.

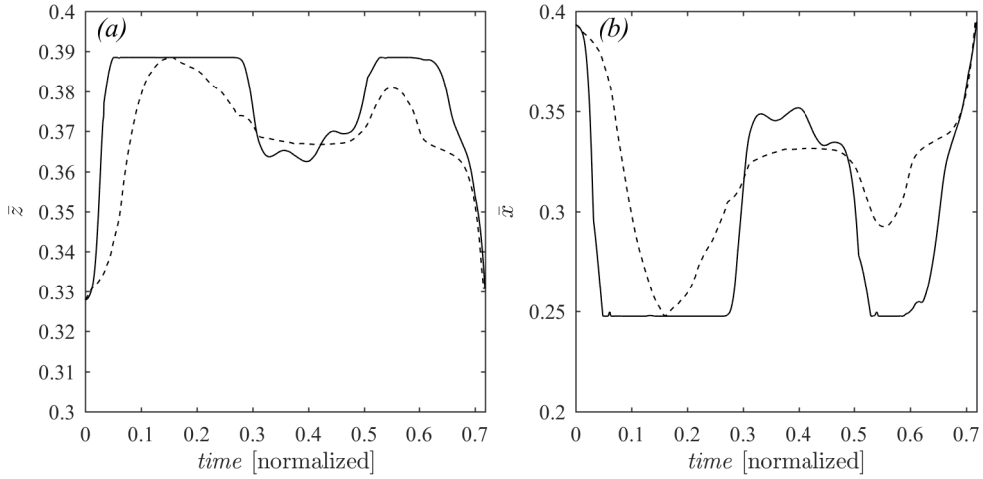

Figure 27: Time evolution of the mean z-coordinate (a), and of the mean x-coordinate (b) for the anterior leaflet: continuous line for the present asymptotic model, dashed line for the elastic FSI model.

This difference does not affect significantly the value of fluid velocity,

shown in figure 26; this is also due to the specific geometry of the leaflets for this valve, visible in figure 25, that are extended in length with a large lateral opening and a motion that is mainly transversal. The quicker opening in the asymptotic model gives rise to a lower velocity during acceleration and a peak flow that is reduced of about 6%, in this case, but that may become more significant in other situations.

In summary, considering the existing difference between the two systems, it was not expected that the asymptotic model results match very closely to the FSI results. The comparative analysis shows that the present model corresponds to MV dynamics where the leaflets movements are more rapid with respect to having elastic resistance with an overall congruence of the coupled MV-LV fluid dynamics. These results provide a further partial support that the model is compatible with the assumption of asymptotic behavior.

9. Healthy and pathological LV with healthy MV

9.1. Fluid dynamics with healthy MV

The computational model is here applied to a normal healthy LV extracted from images as described in §7.1. The cardiac function is characterized by an end-diastolic volume $EDV = 113ml$, end-systolic volume $ESV = 47ml$, stroke volume $SV = EDV - ESV = 67ml$, and ejection fraction $EF = \frac{SV}{EDV} = 59\%$. The specific volumetric curve, gives a velocity at peak diastole of approximately $v_p \simeq 46cm/s$ averaged across the annulus area (whose diameter is approximately $D_a \simeq 3.3cm$). These figures correspond to a peak Reynolds number $Re = \frac{v_p D_a}{\nu} \simeq 3800$ and a Strouhal number $St = \frac{D_a}{v_p T} \simeq 7.2 \times 10^{-2}$. However, the effective peak Re reaches about 1.7 times this value because the effective orifice area of the open mitral valve is smaller that the annulus; although such high values are found for a very limited period of time and the average Re during the entire diastole is about 940.

The flow field is shown in figure 28 at four instants during the cardiac cycle. The overall intraventricular fluid dynamics is qualitatively analogous to that previously described in literature with either orifice-like or different models of the mitral valve in various different geometries of normal LVs [85, 73, 100, 43]. During the early-filling an asymmetric vortex jet, whose head is a deformed vortex ring, enters the LV. The vortex structure interacts with the boundary layer of the lateral wall (right in the pictures) and partly dissipates in diastasis leaving a weak clockwise circulation occupying most of LV, while a second vortex ring follows during the atrial filling. It is worth to note that this second ring is more regular because it is released by the rapid closure of the MV mouth at the onset of systole, when a weak circulation drives the flow toward the outflow tract.

The corresponding time course of the two leaflets opening angle is reported in figure 29. The leaflets show a rapid opening during the acceleration phase of the E-wave reaching the complete opening before the maximum flow, which is in agreement with clinical observation. A small partial closure occurs during the diastasis period, between the E and A waves. At the end of diastole, closure starts at the deceleration phase of the A-wave, due to the adverse pressure gradient, and quickly completes during the acceleration of the systolic wave. The shorter, posterior leaflet is quicker in the early opening and the final closure while the longer anterior leaflet follows shortly after it. As a further check, the same picture reports the opening angle computed by the MV model with one degree of freedom, which presents a comparable valvular movement.

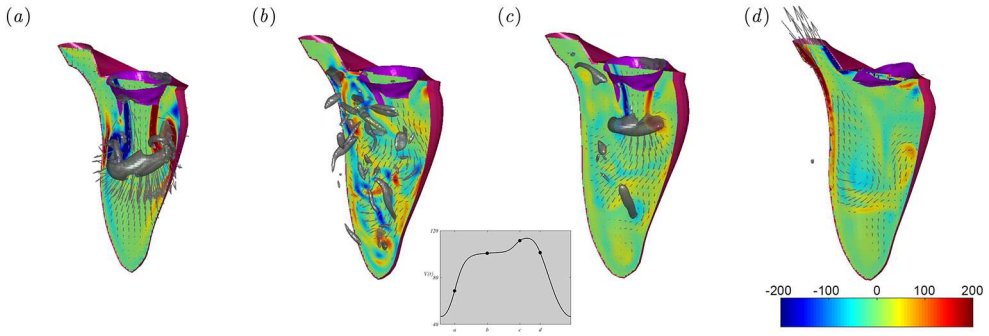

Figure 28: Flow fields in the normal LV , computed with the two degrees of freedom model, at four instants: (a) peak E-wave, (b) diastasis, (c) A-wave, (d) early systole; as indicated in the volume curve inset. Each picture shows the color-map of the normal vorticity (red to blue from -200 to 200 units equal to the inverse of the heartbeat period) and the velocity vectors (every 4 grid points) on a longitudinal plane crossing the center of MV, of aorta and LV apex; the three-dimensional gray surfaces represents one iso-surface of the λ_2 parameter.

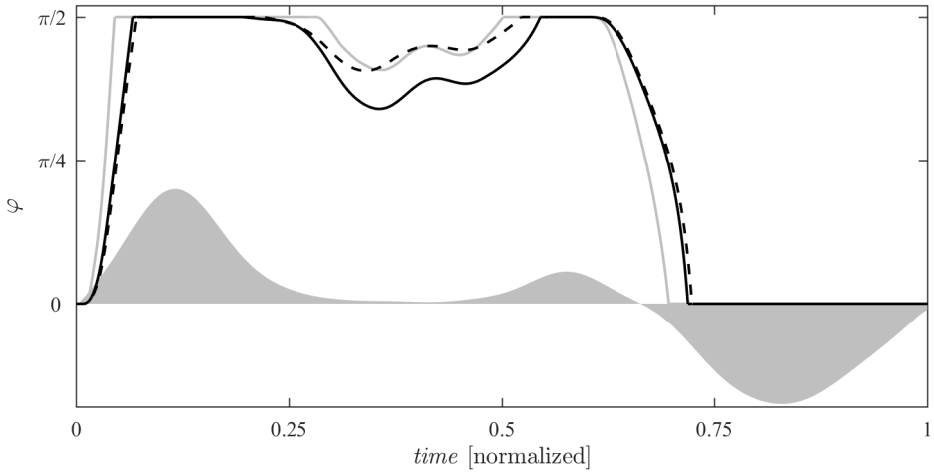

Figure 29: Time course of the mitral valve opening angles in a normal LV. Continuous lines are the anterior (black) and posterior (gray) leaflets opening angles in the 2 degrees of freedom model; the dashed line is the result for a single degree of freedom model. The shaded gray represents the volume rate for reference (not to scale).

In contrast, the pathological condition corresponds to a serious dilated cardiomyopathy. The LV geometry is characterized by an enlarged end-diastolic volume $EDV = 199ml$ and end-systolic volume $ESV = 142ml$, a reduced stroke volume $SV = 57ml$, and a depressed ejection fraction $EF = 29\%$. The flow field, computed by the two degrees of freedom MV

model, is shown in figure 30 at four instants during the heart cycle. The overall intraventricular fluid dynamics in dilated ventricles was previously described in literature [68, 99] and it is confirmed in these results. All dynamic phenomena are weaker because velocities are lower and a slow circulation persists during large part of the heart cycle. The early diastolic jet enters in a chamber with quasi-quiescent fluid, the ring propagates deeper in the large LV, where vortex dissipation and rotating, stagnating fluid is found. The formation of the second vortex ring during the A-wave brings an additional small contribution to the deep circulation that persists during a large part of the weak systole.

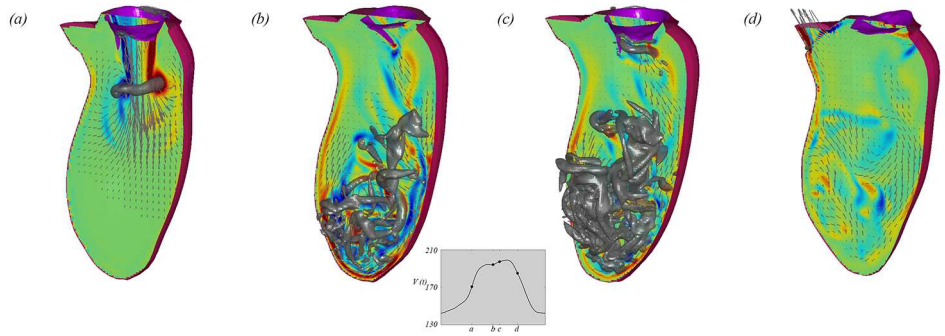

Figure 30: Flow fields in the the pathological, dilated LV, computed with the two degrees of freedom model, at four instants: (a) peak E-wave, (b) diastasis, (c) A-wave, (d) early systole; as indicated in the volume curve inset. Each picture shows the color-map of the normal vorticity (red to blue from -200 to 200 units equal to the inverse of the heartbeat period) and the velocity vectors (every 4 grid points) on a longitudinal plane crossing the center of MV, of aorta and LV apex; the three-dimensional gray surfaces represents one iso-surface of the λ_2 parameter.

The time course of the MV leaflets, whose opening angles are reported in figure 31, confirms the rapid opening at the acceleration of the E-wave and the beginning of closure at the end of diastole with a rapidly completed at the onset of the systolic wave. A remarkable difference from the healthy LV is the significant partial closure during diastasis, which brings the posterior leaflet to a temporary complete closure, and the incomplete opening during the second diastolic wave. The comparison with the result of the one degree of freedom model also corroborates the reliability of the approach.

9.2. Comparison with valveless mitral orifice

The intraventricular flow that develops in a normal LV in presence of the MV is here compared with the flow obtained when the valve is replaced by a circular orifice without leaflets, which is open in diastole and closed in systole

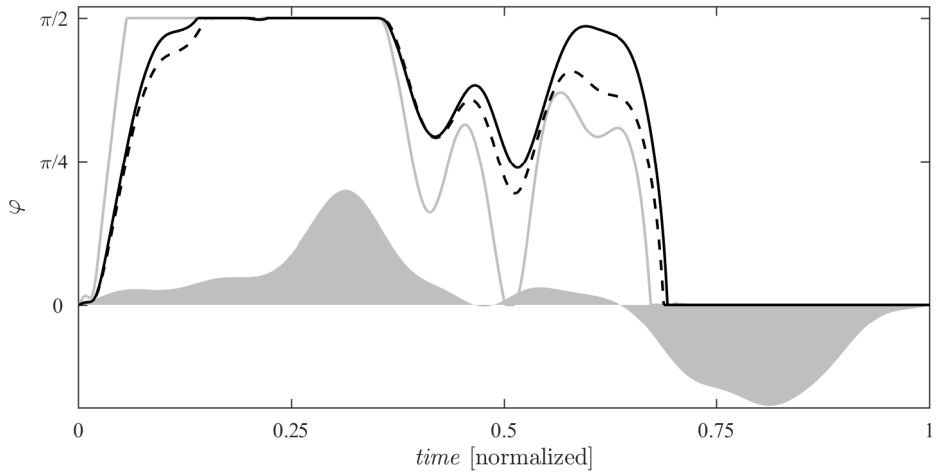

Figure 31: Time course of the mitral valve opening angles in a pathological LV with dilated cardiomyopathy. Continuous lines are the anterior leaflet (black) and posterior (gray) opening angles in the 2 degrees of freedom model; the dashed line is the result for a single degree of freedom model. The shaded gray area represents the volume rate for reference (not to scale).

(so-called diode model). In the comparison we first consider an orifice at the position of the annulus, whose effective area is larger than that of the actual MV, then we consider an orifice with an area that is equal to the MV area in the open configuration.

The flow fields are shown in figure 32 at the peak of the E-wave, one instant that is directly influenced by the MV opening phase. The vortex ring that develops from the larger orifice (figure 32b) is more regular, wider and remains closer to the base with respect to that found with the MV model (figure 32a). This result was expected because the circular orifice has a regular trailing edge and the velocity of the fluid crossing the mitral orifice is smaller. Interestingly, a similar result with a regular and basal vortex ring is also found when the valveless orifice has the same size of the open MV (figure 32c). Although the ring is stronger than before, it remains fairly regular being shed from a planar circular orifice, moreover it remains closer to the base despite the transvalvular fluid velocity is comparable to that in the MV model. This is first imputable to the fact that the boundary layer separation occurs from the LV base instead of the MV leaflets trailing edge that lay downstream. Moreover, the ring is stretched and enlarged by the background (initially irrotational) flow associated to the fixed orifice that expands rapidly behind a circular sharp edge facing the flow. This behavior is very different in presence of an opening valve that drives the flow in a

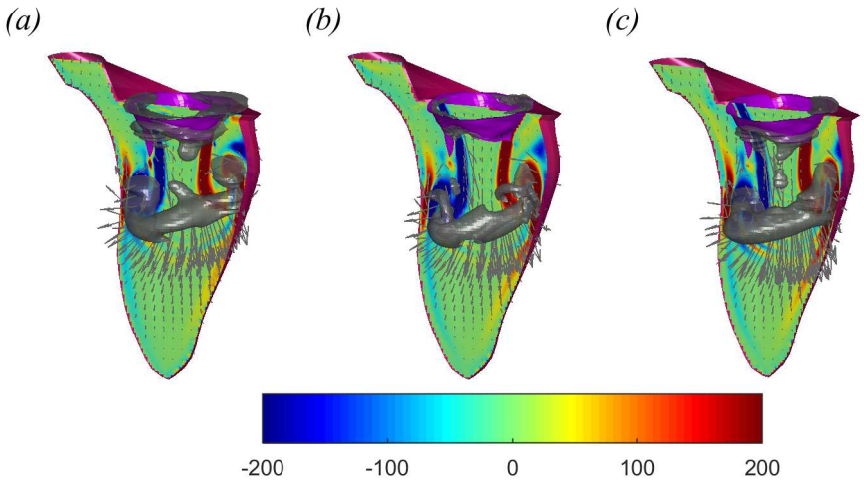

Figure 32: Flow fields in a normal LV at peak E-wave computed with (a) and without (b) the enhanced viscosity at the immersed boundary. Each picture shows the color-map of the normal vorticity (red to blue from -200 to 200, units equal to the inverse of the heartbeat period) and the velocity vectors (every 4 grid points) on a longitudinal plane crossing the center of MV, of aorta and LV apex; the three-dimensional gray surfaces represents iso-surfaces of the λ_2 parameter.

funnel-like stream with velocities that are initially higher and are directed downstream after the trailing edge.

9.3. Interpretation of MV dynamics

Physically, valvular opening is driven by the incoming transmitral flow when the LV pressure falls below the pressure in the left atrium and pressure difference is large enough for accelerating the entire fluid volume corresponding to the filling flow rate $\frac{dV}{dt}$. Valvular opening can thus be described with the aid of conservation of mass [84].

Consider a control volume bounded by the surface within the mitral annulus, the instantaneous valvular surface, and the orifice area inside the trailing edge, $\mathbf{X}_e = \mathbf{X}_v(\vartheta, 1)$, the expression of mass balance states that the total volume rate crossing the annulus is balanced by the volume allowed by the displaced valve surface plus the flow Q_e across the trailing edge orifice

$$\frac{dV}{dt} = \iint_{A_v} \boldsymbol{v} \cdot \boldsymbol{n} dA + Q_e. \tag{35}$$

When elastic resistance can be neglected, it can be hypothesized that the valve opens with the flow without developing significant vortex shedding from the trailing edge [81]. This means that an estimation of the velocity across

the orifice does not differ significantly from that of the trailing edge $\frac{\partial \mathbf{X}_e}{\partial t}$. Within this assumption, the discharge Q_e can be estimated by integrating along a line, L, separating the anterior and posterior trailing edges, taking the area between the facing edges and using the component normal to such area of the mean velocity between them

$$Q_e \cong \int_L \frac{1}{2}\left(\frac{\partial \mathbf{X}_{e_{post}}}{\partial t} + \frac{\partial \mathbf{X}_{e_{ant}}}{\partial t}\right) \cdot \boldsymbol{n} \left|\mathbf{X}_{e_{post}} - \mathbf{X}_{e_{ant}}\right| dL. \tag{36}$$

Equations (35), with Q_e given by 36, provides a relationship between the LV volumetric variation and valvular motion under the assumption of negligible vortex shedding.

This relationship can be made more explicit when valve motion is described by a single degree of freedom, $\varphi(t)$. Using (31) with $N = 1$ to rewrite the time derivatives, equation (35) can be rewritten

$$\frac{dV}{dt} = \left[\iint_{A_v} \frac{\partial \mathbf{X}}{\partial \varphi} \cdot \boldsymbol{n} dA + \hat{Q}_e\right] \frac{\partial \varphi}{\partial t}; \tag{37}$$

where

$$\hat{Q}_e \cong \int_L \frac{1}{2}\left(\frac{\partial \mathbf{X}_{e_{post}}}{\partial \varphi} + \frac{\partial \mathbf{X}_{e_{ant}}}{\partial \varphi}\right) \cdot \boldsymbol{n} \left|\mathbf{X}_{e_{post}} - \mathbf{X}_{e_{ant}}\right| dL. \tag{38}$$

For a given flow rate $\frac{dV}{dt}$, equation (37) represents a first order ordinary differential equation for the opening angle $\varphi(t)$. It can be integrated with initial condition $\varphi(0) = 0$, to provide an estimate of the initial phase of valvular opening.

The valvular motion obtained by (37) is shown in figure 33 and compared with that obtained from the numerical results for both the normal and the pathological cases. The overall agreement is satisfactory for short times, the difference increases as the valve approaches its maximum opening when some shedding develops and the formula (36), or (38), becomes increasingly approximated. Some discrepancy in the pathological LV is imputable to the non-monotonic flow rate presenting a weak deceleration phase during early diastole.

This result supports the interpretation that the asymptotic model in §7.3 corresponds to a valvular opening driven by the fluid crossing the MV without resistance, such that the loose trailing edge moves in close accordance to the fluid velocity and vortex shedding is initially negligible. In this case, valvular opening is essentially a kinematic effect following mass conservation and it does not depend on the geometric properties of the LV other than the flow rate.

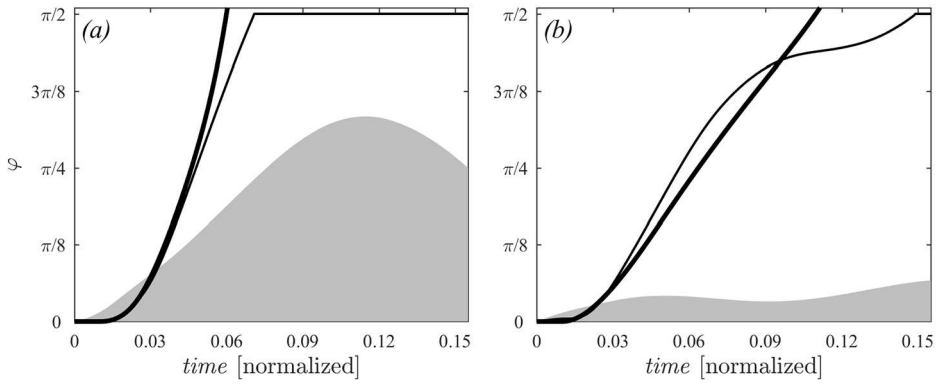

Figure 33: Valvular opening at the onset of diastole as computed by the limiting model (thick line) and obtained from the numerical simulation (think line). (a) normal and (b) pathologic cases. The shaded gray are represents the volume rate for reference (not to scale within the picture but equally scaled between (a) and (b)).

Analogous arguments can be applied to the description of the valvular closure at the transition between diastole and systole. Physically, MV closure starts for the large adverse pressure gradient associated with the deceleration of the late diastolic transmitral flow and continues rapidly during the acceleration of the backward directed systolic wave with no significant role played by the vortices in the LV [65, 94]. Indeed, the vortex-induced velocities are low (few cm/s) and the associated pressure are negligible with respect to the intracardiac pressure differences at the onset of systole. In agreement with the normal physiology, result show that MV closure completes during the beginning of systole. This effect is associated to the phenomenon of false back flow when the blood contained inside the MV cup returns into the atrium when leaflets close. During this phase, a possible elastic recall may facilitate valvular closure although this effect is expected to be small.

Differently, the ventricular vorticity might contribute to the partial valve closure during the diastasis when transvalvular flow rate is small or absent [94]. In this phase of the cardiac cycle, the vortex-induced rotational velocity pattern inside the LV may creates a weak overpressure over the downstream face of the leaflets (especially the longer anterior leaflet) and support partial closure.

For further verification, we perform a numerical experiment and create an artificial LV, which is characterized by the dilated geometry of the pathological case but presents the volume rate identical to the normal case. This artificial modified-dilated LV is obtained by starting with the enlarged end-diastolic volume and modulating its original wall motion to ensure the normal volume rate. The modified-dilated geometry is thus characterized by the

pathological end-diastolic volume $EDV = 199ml$ and a normal stroke volume $SV = 67ml$, resulting to $ESV = 132ml$ and pathological $EF = 34\%$. This model will be used here and in the following subsections to differentiate the phenomena driven by the volume rate from those influenced by the absolute volume size.

The flow field obtained with this modified-dilated model is shown in figure 34 at four instants corresponding to the same phase of the cardiac cycle previously selected for the normal case. The overall intraventricular fluid dynamics presents significant analogies to that found in the regular pathological case with the diastolic vortex ring that propagates deeply in the LV. A difference is the higher intensity of the MV jet and of the E- and A-wave vortex ring developing a higher circulation in the chamber.

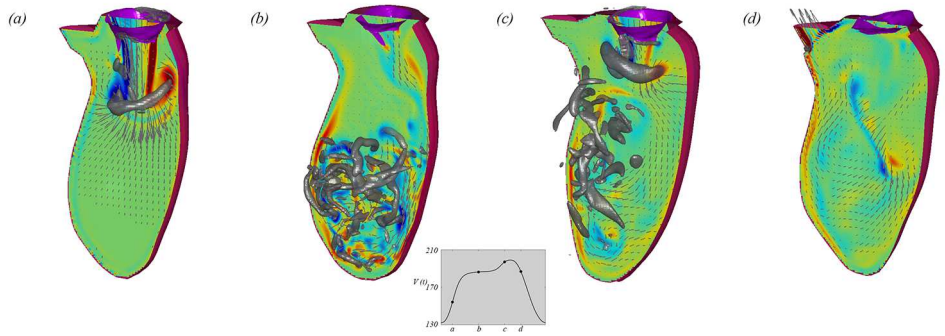

Figure 34: Flow fields in the modified-dilated LV , computed with the two degrees of freedom model, at four instants: (a) peak E-wave, (b) diastasis, (c) A-wave, (d) early systole; as indicated in the volume curve inset. Each picture shows the color-map of the normal vorticity (red to blue from -200 to 200 units equal to the inverse of the heartbeat period) and the velocity vectors (every 4 grid points) on a longitudinal plane crossing the center of MV, of aorta and LV apex; the three-dimensional gray surfaces represents one iso-surface of the λ_2 parameter.

The evolution of corresponding valvular opening angles, φ_1 and φ_2, is shown in figure 35. We want to underline here that the MV leaflets dynamics during the initial opening phase is essentially identical to the one of the normal case (shown in figure 29 and reported here with dashed lines for comparison). This result confirms that the dynamics of valvular opening is dominated by the early acceleration of the transmitral flow and does not depend on the details of the downstream vessel geometry.

9.4. Mitral valve closure at the transition from diastole to systole

Analogous arguments can be applied to the description of the valvular closure at the transition between diastole and systole. MV closure starts

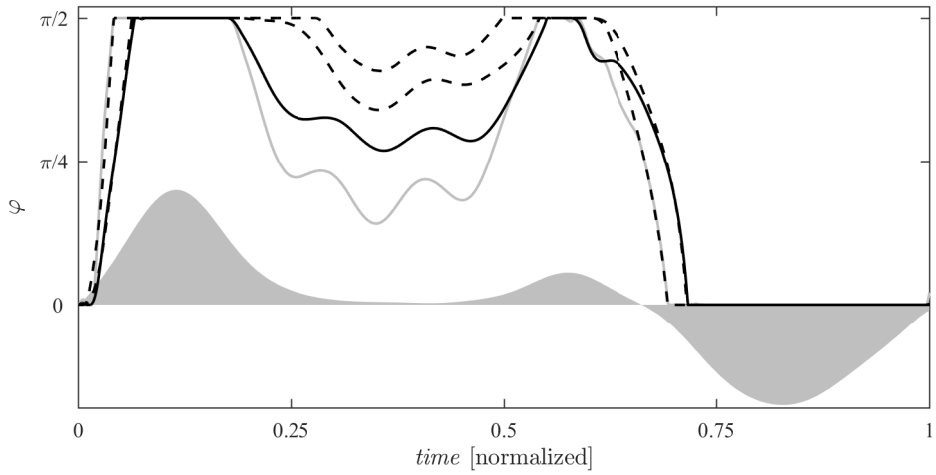

Figure 35: Time course of the mitral valve opening angles in the artificial modified-dilated. Continuous lines are the anterior leaflet (black) and posterior (gray) opening angles in the 2 degrees of freedom model; the dashed lines are the corresponding angles in the normal LV that has the same mitral volume rate. The shaded gray area represents the (normal) volume rate for reference (not to scale).

for the adverse pressure gradient associated with the deceleration of the late diastolic wave (A-wave) and continues rapidly during the acceleration of the backward directed systolic wave.

This is confirmed by the same figure 35 that shows how the eventual final phase of LV closure does not differ significantly between the normal and the modified-dilated LV. This suggests that the physical mechanism is analogous to that described above for the early opening. Although a precise model cannot be easily developed for the absence of a reference starting time.

This observation supports the idea that closure is dominated by the adverse pressure gradient at the end of diastole and the development of the systolic flow, with no role played by the vortices in the LV [65, 94]. On the other hand, the same picture 35 also shows that the early phase of closure at the end of diastole, differs in the two cases indicating that the incipient closure can be influenced by LV flow rotation as repeatedly suggested [9, 101]. However, this influence is limited and will not likely affect, other than to a negligible extent, the amount of back-flow into the atrium at the transition from diastole to systole.

9.5. Partial MV closure at mid-diastole

The ventricular vorticity might contribute to the partial valve closure during diastasis [94]. In this phase of the heart cycle, valvular motion cannot

be driven by the valvular flow rate, that is small or absent, and pressure gradients are equally small. Therefore, it is influenced by the small pressure differences associated with the flow pattern that develops inside the LV.

In diastasis, the time profile of mitral dynamics displays remarkable differences between the normal and the modified-dilated cases, despite the similarities previously discussed for the opening and closure dynamics. In this phase of the cardiac cycle, when the valvular flow is close to zero, the leaflets in the normal LV undergo a limited partial closure (figure 29); differently, those in the modified-dilated LV present a much larger partial closure that persists for a longer period (figure 35). A large closure in diastasis was also recorded in the pathological dilated ventricle (figure 31) corresponding to a different, weaker profile of the flow rate.

The generalized reduced valvular opening at peak flow and enhanced closure during phases of low flow is a common clinical observation in dilated LVs that was imputed to the weaker flow across the valve. These results suggest that the phenomenon of partial MV closure during phases of low flow is influenced by the dimension of the LV, with wider partial closures associated to larger LVs. Careful observations of the flow fields in the three cases, partially visible in figures 28, 30 and 34, evidenced that the intraventricular flow pattern in dilated LVs, either with pathologic or with normal flow rate, presents the common structure made of vorticity located in the deep region of the LV chamber. This differs from the normal case where flow circulation involves the entire ventricle and the vorticity has a higher tendency to stay in the anterior subvalvular region of the LV.

Figure 36 shows the distribution of pressure in the three cases during diastasis; pressures are relative to the average LV value assumed as reference zero (that is undefined in the numerical model). The pressure differences are very small, over one order of magnitude smaller than the values found during flow accelerations (that reach several thousands of the present units, or a few mm_{Hg}), however these small pressure gradients represent the only driving force in place. The normal case is characterized by a minimum of pressure slightly downstream behind the valve, which corresponds to core of the intraventricular vorticity pattern. This vortex structure represents the wake behind the solid element, influencing its dynamics with a small lift force helping to keep the leaflet open. Differently, in the large LVs, pressure reaches its minimum values deep in the chamber, where the vorticity of the incoming jet has accumulated and eventually dissipates. This pressure pattern does not provide any lift to the leaflet and may rather enhance the development of an adverse pressure gradient.

Therefore, in normal ventricles the confined natural circulation remains near the valve producing a lift that sustains the leaflets opening. This effect

is not present in enlarged ventricles when the vorticity travels to the apex away from the valve. In this case the leaflets have a higher tendency to close during diastasis and to anticipate closure at end diastole as shown in figure 35.

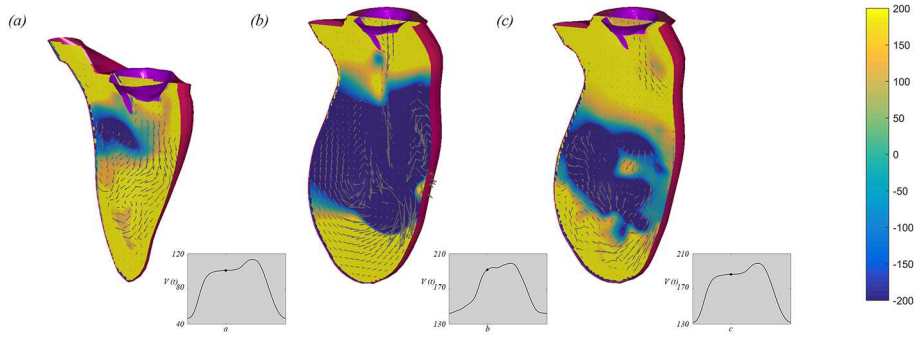

Figure 36: Relative pressure field during diastasis: (a) normal case, (b) pathological case, (c) modified-dilated case; the exact instants are indicated by the volume curve insets. Each picture shows the color-map of the pressure as by the color scale on the right (notice the natural scale for kinematic pressure is cm^2/T, T is the heartbeat; 200 units correspond approximately to $20Pa$ or $0.15mm_{Hg}$).

9.6. Slower deceleration of E-wave and mid-diastolic L-wave

The phenomenon of partial valvular closure described above may have an impact on parameters commonly measured for diagnostic purposes. The flow across the mitral valve is routinely measured in echocardiography by pulsed-wave Doppler; this technique evaluates the time profile of the longitudinal component of blood velocity averaged over a sample volume at the outlet of the mitral valve leaflets. This time profile is then used to extract a few indexes of diastolic function, like the ratio between the peaks of E- and A-wave or the deceleration time (DT) of the E-wave [77]. Although the motion of the mitral leaflet cannot be monitored directly, it directly influences the velocity at the exit of the MV because it varies the size of the trailing edge orifice.

A partial valvular closure during diastasis can give rise to a slower decrease of the velocity at the end of E-wave (longer DT), which is a first indication of the so-called diastolic dysfunction. In particular, the development of one additional peak of velocity between the E- and the A-wave, commonly called L-wave, is considered an evidence of dysfunction [50, 60]. A dysfunction that is often associated with the dilatation of the LV (unless it is accompanied with an alteration of the LV stiffness and hypertension).

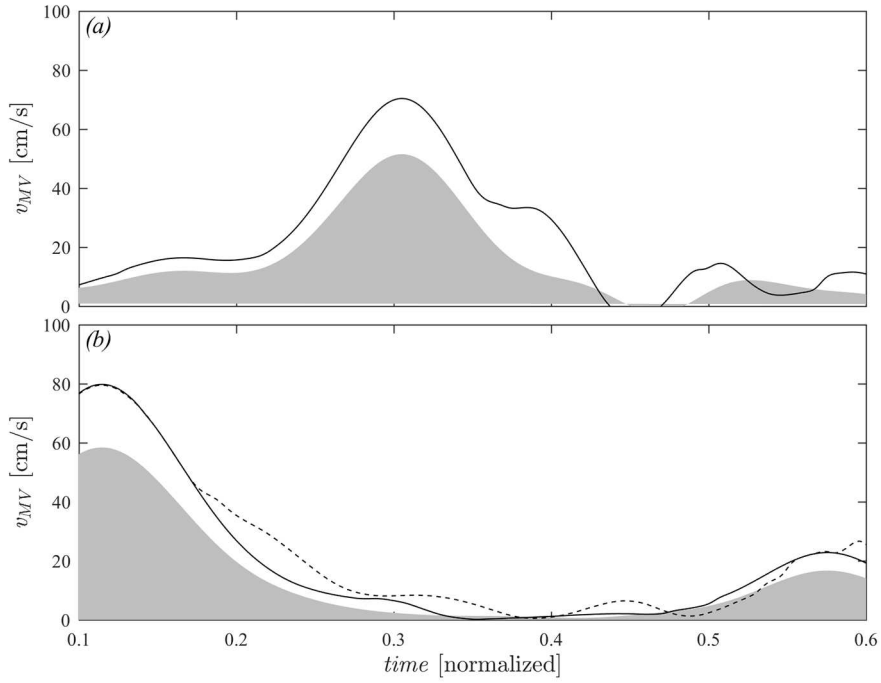

Figure 37: Time profile, during diastasis, of the downward component of blood velocity at the outlet of the mitral valve. (a) pathological case, (b) normal case and modified-dilated case (dashed line). The mean velocity across the annulus is reported with shaded gray for comparison.

In our simulations the flow rate imposed by the volume change presents a regular profile in the normal case and a small persistence of the E-wave in the pathologic case. It is possible to include the influence of the leaflets' motion and measure the mean velocity at the outlet of the MV to mimic the clinical measurement of mitral flow. This is achieved by evaluating the outflow discharge $Q_e(t)$ using equation (35), divided by the orifice area $A_e(t)$

$$A_e \cong \int_L \left| \mathbf{X}_{e_{post}} - \mathbf{X}_{e_{ant}} \right| dL, \tag{39}$$

and taking the downward directed component $v_{MV}(t) = -\frac{Q_e}{A_e} n_z$, where n_z is the z-component of the average normal to the orifice surface of area A_e.

The mitral outlet velocity, reported in figure 37, shows evidence of the delayed deceleration (longer DT) with appearance of a L-wave in the pathological case. This observation, that does not occur in the normal case, also appears in weaker form in the modified-dilated case in correspondence of a normal flow rate.

This result provides a physical explanation for observation commonly performed in clinical cardiology. The larger DT due to a slower deceleration of the diastolic E-wave and the possible emergence of mid-diastolic L-wave represent an increase of the velocity at the MV outlet during diastasis, which can be partially imputable to the closure of the mitral leaflets. This demonstrates how the MV dynamics may have a potential impact on the existing clinical indicators representing an explanation or a confounding factor to be considered for proper clinical validations.

10. Healthy and pathological LV with prolapsed MV

10.1. MVP geometries

The analysis is performed on a series of MVs with different degrees and types of prolapse. On the one end, a normal geometry (called healthy-1) is used for reference, figure 38 (a). MVP in figure 38 (b) is a prolapse P3 of type I MR with incomplete coaptation of the leaflet and insufficient surface of coaptation of the leaflet and consequent reduction of the mitral valve area MVA. The MVP in figure 38 (c) is a prolapse P2 of type II MR with leaflet prolapsed caused by elongation of the chordae tendineae.

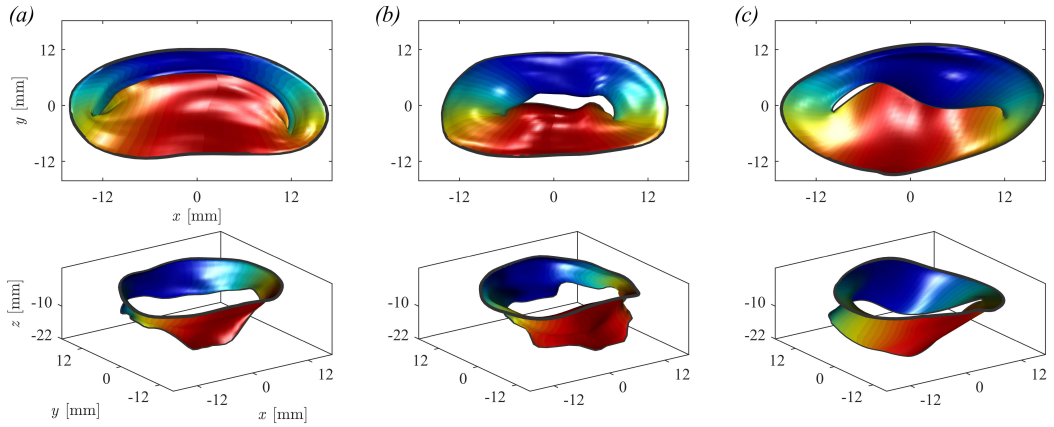

Figure 38: Closed and open configuration of (a) Healthy MV, (b) P3 Prolapse, (c) P2 Prolapse.

In addition, in order to evaluate intermediate conditions, we have artificially modified the dimension of the P3 prolapse by stretching the leaflets to let facing edges approach each other. Figure 27 shows the MV geometry at end-systole with original prolapse (P3, figure 39 (a), equal to figure 38 (b)), a reduction of 25% of the original prolapse (P3-25%, figure 39 (b)), of 50% (P3-50%, figure 39 (c)) and the 100% correction to non regurgitating geometry (P3-Healthy, figure 39 (d)).

Numerical simulations are performed with six different MVs in both healthy and pathological LVs, this allows to compile an initial general picture of fluid dynamics properties associated to the evaluation of the regurgitation. Table 1 summarizes the different conditions analyzed in the present study.

10.2. Regurgitation analysis

This section describes the methods used for the numerical calculation of the MR properties. The effective area of the MV orifice area is computed by

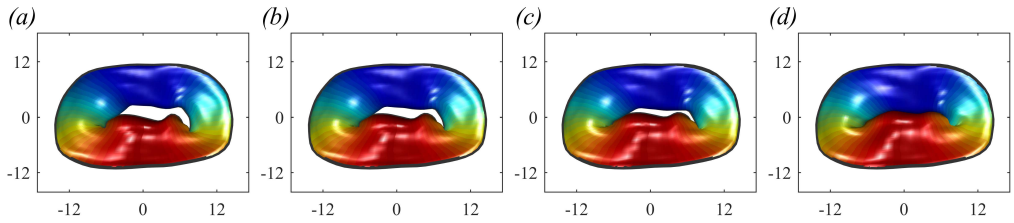

Figure 39: Original MV with P3 prolapse (a), modified MV with P3 prolapse reduced by 25% (b), reduced by 50% (c), reduced by 100% (d).

MV	**LV**	**LV**
Healthy	Healthy	Dilated
P3	Healthy	Dilated
P2	Healthy	Dilated
P3-25%	Healthy	Dilated
P3-50%	Healthy	Dilated
P3-Healthy	Healthy	Dilated

Table 1: List of numerical simulations with different MVs and LVs

measuring the space between the leaflets trailing edge

$$MVO(t) = \int_0^L \left|\mathbf{X}_{e_{ant}} - \mathbf{X}_{e_{post}}\right| dL; \tag{40}$$

where $\mathbf{X}_e$=$\mathbf{X}_v(\vartheta, 1)$, is the trailing edge that is subdivided in the anterior and posterior leaflets, and L is the length of a curve running along the mid-point between the two edges. The EOA of a regurgitant orifice is the MVO evaluated from equation (40) during systole when the MV is in the closed configuration. The calculation of the blood flow rate effectively crossing the MV orifice is computed by

$$Q_{MV}(t) = \int_0^L \boldsymbol{v}_{rel} \cdot \boldsymbol{n} \left|\mathbf{X}_{e_{ant}} - \mathbf{X}_{e_{post}}\right| dL, \tag{41}$$

where the relative velocity, $\boldsymbol{v}_{rel} = \bar{v} - \frac{\partial}{\partial t}\frac{\mathbf{X}_{e_{ant}} - \mathbf{X}_{e_{post}}}{2}$, is the difference between the fluid velocity averaged along the line between the two facing edges and the velocity of the edges themselves, and $\boldsymbol{n}$ is the local normal. From this, the regurgitating blood volume is the flow crossing the MVO during systole

$$V_{reg} = \int_{sys} Q_{MV}(t)dt. \tag{42}$$

It will be useful, for comparison, also to compute the blood volume crossing the MV annulus (MVa) to separate the contribution due to leaflets motion

$$Q_{MVa}(t) = \int_{A_{MVa}} (v_{rel_{MVa}} \cdot \boldsymbol{n})\, dA, \tag{43}$$

where A_{MVa} is the area of MVa, the relative velocity $\boldsymbol{v}_{rel_{MVa}} = \bar{v}_{MVa} - \frac{\partial \bar{X}_{MVa}}{\partial t}$ is the difference between the fluid velocity averaged over the MVa and the average velocity of the annulus, where $\bar{X}_{MVa}$ is the average position vector of the MV annulus. Then, the regurgitating blood volume measured across the MVa is

$$V_{reg_{MVa}} = \int_{sys} Q_{MVa}(t)dt. \tag{44}$$

For further reference, we have also considered the flow crossing the LV annulus

$$Q_{LV}(t) = \int_{A_{LVa}} (v_{rel_{LVa}} \cdot \boldsymbol{n})\, dA, \tag{45}$$

where A_{LVa} is the area of LVa, the relative velocity $\boldsymbol{v}_{rel_{LVa}} = \bar{v}_{LVa} - \frac{\partial \bar{X}_{LVa}}{\partial t}$ is the difference between the fluid velocity averaged over the LVa and the average velocity of the annulus, where $\bar{X}_{LVa}$ is the average position vector of the LV annulus. Then, the blood volume measured across the LVa is

$$V_{LVa} = \int_{dia} Q_{LV}(t)dt. \tag{46}$$

These same evaluations introduced above, can be extended to define the quality of blood present in these volumes. The knowledge of the concentration field, computed by (3), allows recognizing the amount of flow that is composed of blood that was present in the LV before the beginning of diastole (hereafter indicated as *old*) or, by difference, that entered the LV during last diastole (*fresh*). The old blood volume regurgitated by MV orifice is obtained by extending (41) as

$$Q_{MV_{old}}(t) = \int_0^L \boldsymbol{v}_{rel} \cdot \boldsymbol{n} \left| \mathbf{X}_{e_{ant}} - \mathbf{X}_{e_{post}} \right| C\, dL\, A_{MVa}, \tag{47}$$

where C is the concentration measured at the MV orifice; the corresponding volume is

$$V_{reg_{old}} = \int_{sys} Q_{MV_{old}}(t)dt. \tag{48}$$

10.3. Fluid dynamics with MVP

In this section, we describe the fluid dynamics that develops in normal and dilated LV geometry in presence of the different MV morphologies described in §10.1. The normal LV is characterized by $EDV = 113.47ml$, $ESV = 47.52ml$, $ESV = 66.95ml$, and ejection-fraction $EF = \frac{SV}{EDV} = 59\%$.

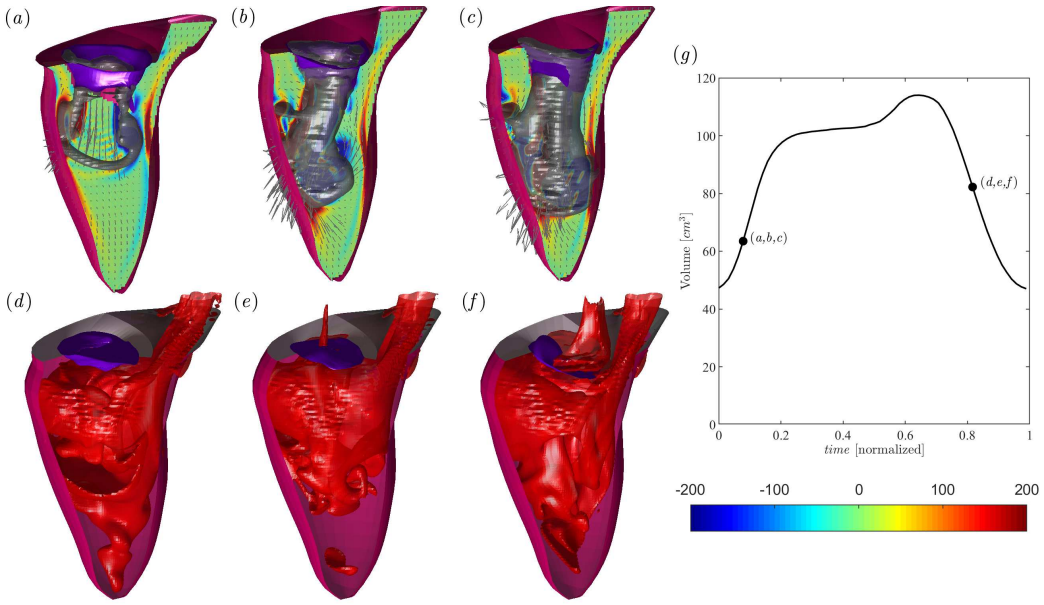

Figure 40: Flow field in the normal LV in presence of a healthy MV (a,d), MV with P3 Prolapse (b,e) and P2 Prolapse (c,f). Diastolic flow at peak E-wave (a), (b), (c); as indicated in the volume curve inset (black line in (g)); the normal vorticity is shown by red to blue color from -200 units to 200 units equal to the inverse of the heartbeat period and the velocity vector (every 4 grid points) on a longitudinal plane crossing the center of MV, of aorta and LV apex; the three-dimensional grey surfaces represents one iso-surface of the λ_2 parameter. The lower side is the three-dimensional flow field in the normal LV calculated with the passive scalar iso-surface method at the same instants of early systole at value C=0.4; as indicated in the volume curve inset. The inset (g) reports the volume curve and the instant of the case analyzed.

The flow field in the normal LV at peak diastole is shown in figure 40 (a-c) in correspondence of (a) Healthy, (b) P3 and (c) P2 MVs. The flow with healthy MV presents the typical asymmetric vortex ring that enters into the LV, the P3 case shows a vortex ring that deviates and breaks down when impacting the posterior wall, finally the mitral jet in the P2 MV is characterized by an irregular flow that enters in depth in the center of the LV probably because of the slightly reduced dimension of the MVO. Figure 40 (d,e,f) reports the corresponding concentration field at peak systole. The healthy case evidences blood that is well mixed between old and fresh blood

in the entire chamber; differently, the prolapse MVs are associated with a greater presence of old blood near the apex and displays regurgitation in atrium.

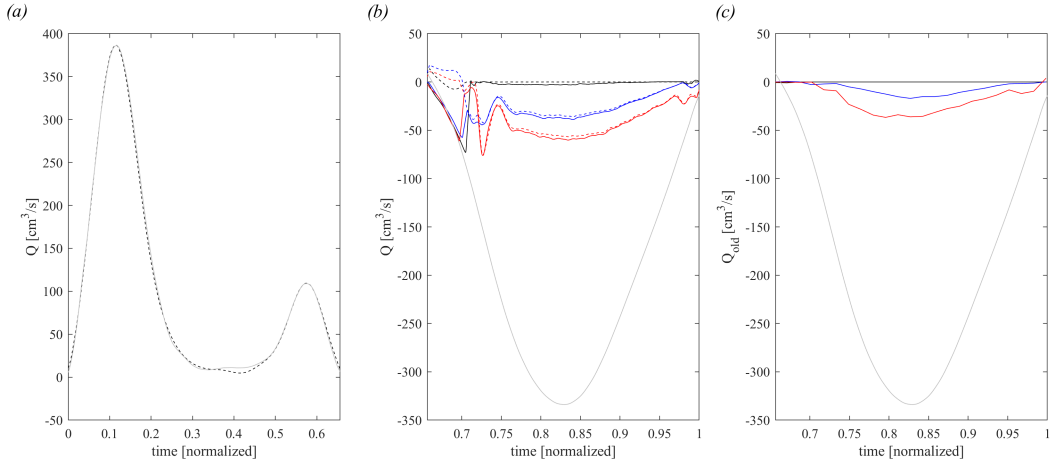

Figure 41: Flow balance in diastole. (a): comparison between diastolic dV/dt (dashed dark line) and diastolic Q_{LV} (continuous grey line) in healthy LV. In systole, (b): comparison of the Q_{MV_a} (continuous line) and Q_{MV} (dashed line) respectively for healthy-1 MV (dark line), P3 MVP (blue line), P2 MVP (red line) and the grey continuous line is the systolic dV/dt, (c): Old blood flow regurgitated in atrium, computed by $Q_{MV_{old}}$ respectively for healthy MV (dark line), P3 MVP (blue line), P2 MVP (red line) and the grey continuous line is the systolic dV/dt.

The flow profile, dV/dt, for the healthy LV is shown in figure 41 (a) during diastole and in figure 41 (b) during systole (light grey curves), their integral represents the stroke volume $66.95cm^3$. For comparison, Figure 41 (a) also reports the time profile of Q_{LV} computed by equation (45), that gives and integral $V_{LV} = 67.25cm^3$. Such agreement between volume change and measured flow rate represents an indirect agreement of the reliability of the present IBM calculation.

The systolic outflow in aorta in figure 41 (b) is plotted together the blood flow that crosses the LV annulus and returns to the atrium, Q_{MVa} computed by (43) (continuous lines), and with the blood flow that crosses the MV orifice, Q_{MV} computed by (41) (dashed lines), respectively for normal (healthy: black color) and prolapsed MVs (P3: blue, and P2: red). The first part of systole corresponds to the closing period of the MV, here the continuous and dashed curves differ because Q_{MVa} includes the volume of blood contained in the MV pool above the orifice that returns back to the atrium during MV closure; afterwards the curves come together along a common path. The initial difference represents the so-called false regurgitation that identifies the

physiological blood flow returning in the atrium during the closure of the MV leaflets, which is estimated by the difference $V_{reg_{false}} = V_{reg_{MVa}} - V_{reg}$ computed with (44) and (42). The same curves of regurgitating flow are shown in figure 41 (c) limiting the calculation to the old blood only, computed by equation (47). The overall entity or old blood regurgitations is nearly proportional to the total regurgitations; nevertheless, it is evident that the old blood enters the atrium mainly during the second half of systole when ejection has involved the entire LV volume. The initial regurgitation is mainly composed of fresh blood that reached the region just behind the behind the valve and is the first involved in the back flow.
The integral results relative to all the different MVs are reported in Table 2. The healthy valve is a physiologic MV that presents a non-zero $EOA = 0.06cm^2$, corresponding to a tiny hole 1% the valve size that is not caused by pathological valvular deformation, or imputable to minor inaccuracy in image segmentation. Results show how the increase of the EOA corresponds to an increase of V_{reg}, whose correlation will be analyzed later. Regurgitation reaches about 10% of the SV in the present P3 prolapse and about 20% in P2. It is noticed that a small non-zero regurgitation is also found in healthy valves, indicating that MV velocity during closure is slightly lower than blood velocity. The false regurgitation, $V_{reg_{false}} = V_{reg_{MVa}} - V_{reg}$, represents the fresh atrial blood that does not cross the MV orifice and returns into the atrium at the beginning of systole. This does not depend on the EOA and is more a consequence of the MV shape.

	$\boldsymbol{MVA}$ $[cm^2]$	$\boldsymbol{EOA}$ $[cm^2]$	$\frac{\boldsymbol{EOA}}{\boldsymbol{MVA}}$ $[\%]$	$\boldsymbol{SV}$ $[cm^3]$	$\boldsymbol{V_{reg_{MVa}}}$ $[cm^3]$	$\boldsymbol{V_{reg_{false}}}$ $[cm^3]$	$\boldsymbol{V_{reg}}$ $[cm^3]$	$\frac{\boldsymbol{V_{reg}}}{\boldsymbol{SV}}$ $[\%]$
Healthy	**6.20**	**0.06**	1	66.95	2.07	1.64	0.43	0.65
P3	**4.83**	**0.52**	11	66.95	8.87	2.58	6.29	9.40
P2	**4.26**	**0.87**	20	66.95	13.42	0.66	12.76	19.07
P3-25%	**4.83**	**0.39**	8	66.95	4.57	2.49	2.08	3.11
P3-50%	**4.83**	**0.26**	5	66.95	2.58	1.00	1.58	2.37
P3-Healthy	**4.83**	**0**	0	66.95	1.70	0.80	0.80	1.20

Table 2: Global results in healthy LV. MVA=Mitral Valve Area, EOA=Effective orifice area in MV closed position, $\frac{EOA}{MVA}$=EOA normalized with MVA, SV=Stroke Volume, $V_{reg_{MVa}}$=Total Regurgitation, $V_{reg_{false}}$=False Regurgitation, V_{reg}=Regurgitation from orifice, $\frac{V_{reg}}{SV}$=$Vreg$ regnormalized with SV.

Table 3 shows the volume of residual old blood stagnant into the LV at end systole and the volume of old blood regurgitated in atrium. These results show that the residual volume $V_{residual}$ is only moderately influenced by the MV regurgitation that, therefore, does not directly influence the LV wash-

out. On the other hand, the increase of regurgitation is associated with a larger percentage of old blood regurgitated that reaches a value as high as 50% in the most diseased case.

	$\boldsymbol{EOA}$ $[cm^2]$	$\boldsymbol{V_{residual}}$ $[\%]$	$\boldsymbol{V_{reg_{old}}}$ $[cm^3]$	$\frac{\boldsymbol{V_{reg_{old}}}}{\boldsymbol{V_{reg}}}$ $[\%]$
Healthy	0.06	28.50	0.03	6.98
P3	0.52	26.07	2.36	37.52
P2	0.87	30.67	6.42	50.31
P3-25%	0.39	25.28	0.70	33.65
P3-50%	0.26	25.60	0.09	5.70
P3-Healthy	0	26.12	0.01	1.25

Table 3: Global transit results in healthy LV. EOA=Effective orifice area in MV closed position, $V_{residual}$ is the LV residual volume at end-systole, $Vreg_{old}$ is the quantity of the old blood regurgitated in atrium, $\frac{Vreg_{old}}{Vreg}$ is the old blood regurgitated normalized with $Vreg$, $V_{residual}$=Residual volume.

The same analysis is repeated in correspondence of a pathological ventricular geometry corresponding to a severe dilated cardiomyopathy. The dilated LV is characterized by an enlarged end-diastolic volume $EDV = 199.31ml$, end-systolic volume $ESV = 142.50ml$, $SV = 56.82ml$, and ejection-fraction $EF = 29\%$.
The flow field in the dilated LV at peak diastole is shown in figure 42 (a-c) in correspondence of (a) Healthy, (b) P3 and (c) P2 MVs. The overall intraventricular fluid dynamics in dilated ventricles was previously described in literature [68, 99] and it is qualitatively confirmed by the present results. All dynamic phenomena are weaker because velocities are lower, and a slow circulation persists during a large part of the heart cycle. In the dilated LV with healthy MV (figure 42 (a)) the early diastolic jet enters in a chamber with quasi-quiescent fluid, the ring propagates deeper in the large LV before it interacts with the walls and partly dissipates. In presence of pathological MV (figure 42 (b, c)), the mitral jet and the vortex ring at the jet's head presents the same deviation previously noticed in the normal LV, which is caused by the arrangement of the MVO. Figure 42 (d-f) reports the corresponding concentration field at peak systole. Blood is well mixed between old and fresh blood but with more marked presence of old blood in the entire chamber caused by a larger size of the pathological ventricle and reduced wash-out.

The flow profile, dV/dt, for the dilated LV is shown in figure 43 (a) during diastole and in figure 43 (b) during systole (light grey curves), their integral represents the stroke volume $56.82cm^3$. For comparison, Figure 43

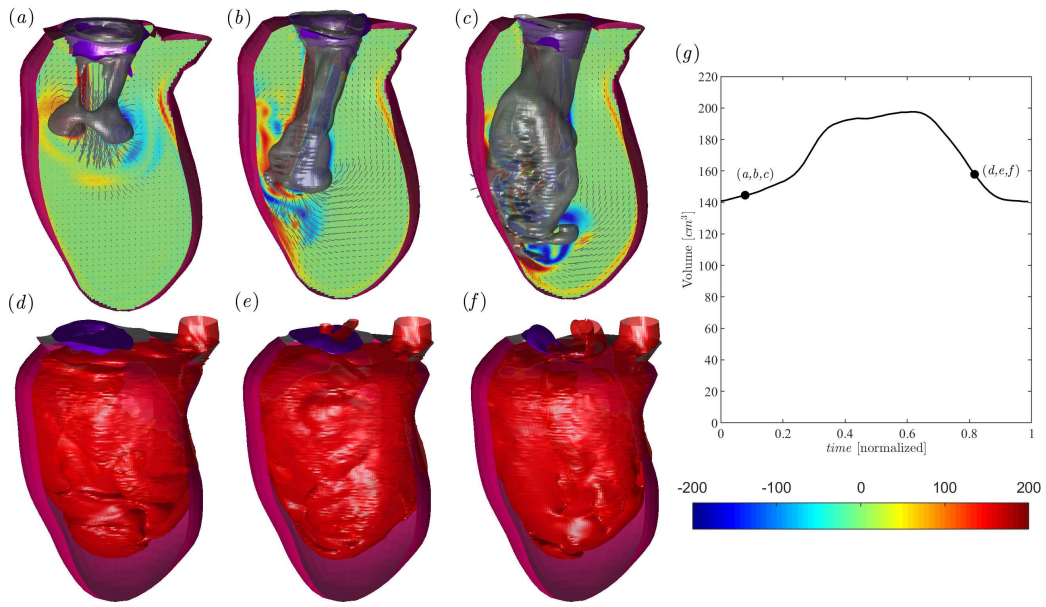

Figure 42: Flow field in the dilated LV in presence of a healthy MV (a,d), MV with P3 Prolapse (b,e) and P2 Prolapse (c,f). Diastolic flow at peak E-wave (a), (b), (c); as indicated in the volume curve inset (black line in (g)); the normal vorticity is shown by red to blue color from -200 units to 200 units equal to the inverse of the heartbeat period and the velocity vector (every 4 grid points) on a longitudinal plane crossing the center of MV, of aorta and LV apex; the three-dimensional grey surfaces represents one iso-surface of the λ_2 parameter. The lower side is the three-dimensional flow field in the dilated LV calculated with the passive scalar iso-surface method at the same instants of early systole at value C=0.4; as indicated in the volume curve inset. The inset (g) reports the volume curve and the instant of the case analyzed.

(a) reports the time profile of Q_{LV} computed by equation (45), that gives and integral $V_{LV} = 56.82cm^3$. The systolic outflow in Figure 43 (b) is computed and reported with the same procedure described above for the normal LV, and confirms the presence of false regurgitation at the beginning of systole. Similarly, the quantity of old blood regurgitated, shown in figure 43 (c), presents a trend that is similar to the normal case.

Quantitative evaluations are obtained by the integral results reported in table 4 and table 5 (to be compared with previous tables 2 and 3 relative to normal LV). The values of regurgitation are comparable between normal and dilated conditions in correspondence of the save MV. This is true both in absolute and relative terms, considering that the two LVs have a similar SV. A remarkable difference is found in terms of wash-out, where the dilated LV presents a much larger residual volume, independently from the MV. Also, the quantity of old blood regurgitated is partially increased, indicating that some larger amount of old blood returns back to the atrium and further re-

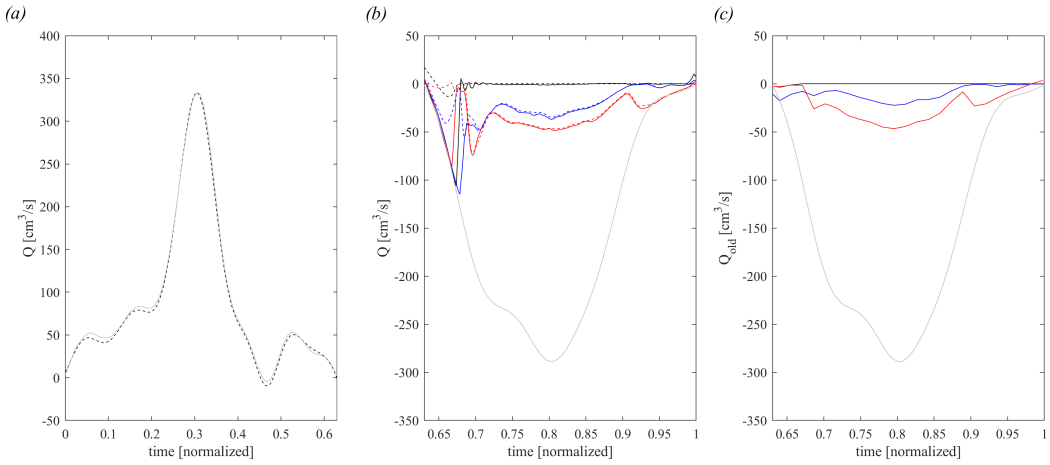

Figure 43: Flow balance in diastole. (a): comparison between diastolic dV/dt (dashed dark line) and diastolic Q_{LV} (continuous grey line) in dilated LV. In systole, (b): comparison of the Q_{MVa} (continuous line) and Q_{MV} (dashed line) respectively for healthy-1 MV (dark line), P3-3 MVP (blue line), P2 MVP (red line) and the grey continuous line is the systolic dV/dt, (c): Old blood flow regurgitated in atrium, computed by $Q_{MV_{old}}$ respectively for healthy-1 MV (dark line), P3-3 MVP (blue line), P2 MVP (red line) and the grey continuous line is the systolic dV/dt.

duces the overall washout of the entire left heart thus theoretically increasing the risk of platelet activation and thrombus formation.

	$\boldsymbol{MVA}$ $[cm^2]$	$\boldsymbol{EOA}$ $[cm^2]$	$\frac{\boldsymbol{EOA}}{\boldsymbol{MVA}}$ $[\%]$	$\boldsymbol{SV}$ $[cm^3]$	$\boldsymbol{V_{reg_{MVa}}}$ $[cm^3]$	$\boldsymbol{V_{reg_{false}}}$ $[cm^3]$	$\boldsymbol{V_{reg}}$ $[cm^3]$	$\frac{\boldsymbol{V_{reg}}}{\boldsymbol{SV}}$ $[\%]$
Healthy	**6.20**	**0.06**	1	56.82	2.41	2.40	0.10	0.18
P3	**4.83**	**0.52**	11	56.82	9.27	2.01	7.26	12.77
P2	**4.26**	**0.87**	20	56.82	11.74	0.04	11.70	20.60
P3-25%	**4.83**	**0.39**	8	56.82	5.78	1.96	3.82	6.73
P3-50%	**4.83**	**0.26**	5	56.82	3.53	2.05	1.48	2.61
P3-Healthy	**4.83**	**0**	0	56.82	3.02	2.01	1.01	1.77

Table 4: Global results in dilated LV. MVA=Mitral Valve Area, EOA=Effective orifice area in MV closed position, $\frac{EOA}{MVA}$=EOA normalized with MVA, SV=Stroke Volume, $V_{reg_{MVa}}$=Total Regurgitation, $V_{reg_{false}}$=False Regurgitation, V_{reg}=Regurgitation from orifice, $\frac{V_{reg}}{SV}$=$Vreg$ normalized with SV.

Figure 44 (a) reports the correlation between the functional measure of valvular insufficiency, given by the regurgitant volume, and the structural measure, given by the EOA. Once these values are properly normalized the

	$\boldsymbol{EOA}$ $[cm^2]$	$\boldsymbol{V_{residual}}$ $[\%]$	$\boldsymbol{V_{reg_{old}}}$ $[cm^3]$	$\frac{\boldsymbol{V_{reg_{old}}}}{\boldsymbol{V_{reg}}}$ $[\%]$
Healthy	0.06	68.50	0.01	10
P3	0.52	69.79	3.74	51.51
P2	0.87	70.90	8.33	71.70
P3-25%	0.39	69.70	1.88	49.21
P3-50%	0.26	69.49	0.57	38.51
P3-Healthy	0	69.02	0.61	60.4

Table 5: Global transit results in dilated LV. EOA=Effective orifice area in MV closed position, $V_{residual}$ is the LV residual volume at end-systole, $Vreg_{old}$ is the quantity of the old blood regurgitated in atrium, $\frac{Vreg_{old}}{Vreg}$ is the old blood regurgitated normalized with $Vreg$, $V_{residual}$=Residual volume.

two quantities present a direct proportionality

$$\frac{Vreg}{SV} \cong \frac{EOA}{MVA}. \tag{49}$$

with good accuracy without evident differences for the different type of prolapse or the LV size. Figure 44 (b) shows a good correlation between the total regurgitation and the portion made of old blood; however, some difference is noticeable between normal and dilated LVs as previously underlined.

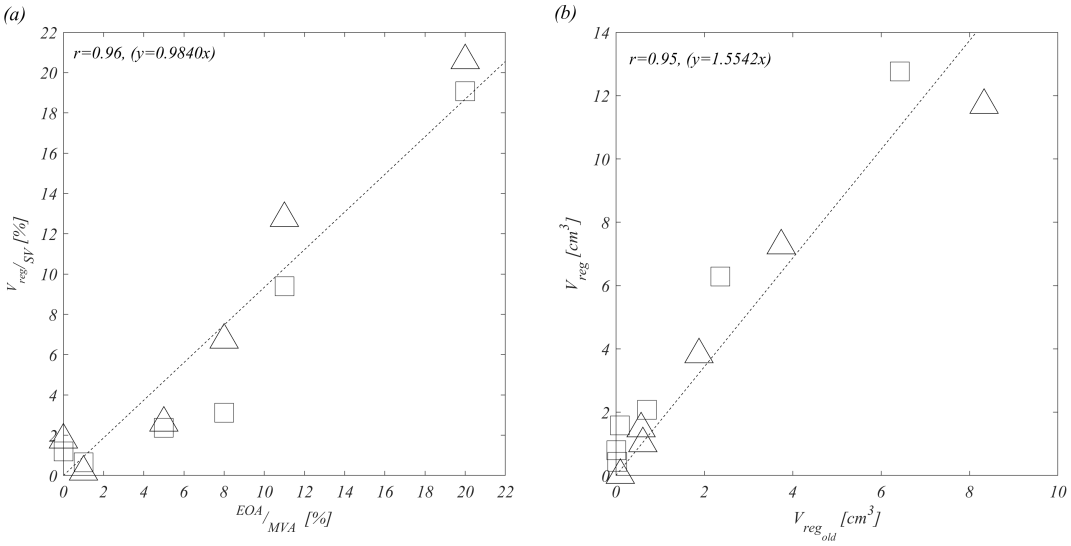

Figure 44: Correlation between: $\frac{V_{reg}}{SV}$ and $\frac{EOA}{MVA}$ considering all MV cases and healthy LV (square) and dilated LV (triangle) (a), V_{reg} and $V_{reg_{old}}$ considering all MV cases and healthy (square) and dilated LV (triangle) (b).

11. Discussion of model limitations

The computational model introduced here should not be confused with a FSI model, primarily because it does include the elastic properties of the tissues that would be required to solve the momentum equation for the solid elements. Therefore, it describes an asymptotic behavior only and was designed to provide a relatively straightforward application of LV flow simulations in clinical conditions when the mechanical properties of tissue are not available or cannot be extrapolated. To reach this objective, the model includes a number of simplifications that correspond to a series of limitations that are briefly summarized here.

First of all, the set of possible valve configurations is given a-priori as a function of few evolutionary parameters (degrees of freedom). Hence, there is no guarantee that the effective deformation of the tissue elements belongs to such a pre-defined set of configurations; the actual reliability depends on the reliability and completeness of the information used to create such configurations and to the associated degrees of freedom. Secondly, the fluid-tissue interaction describing MV motion represents an asymptotic behavior where the valve moves with the flow with no resistance given by an internal anatomic structure other than the constraint of moving inside the set of predefined configurations. Therefore, the model corresponds to the loosest tissue dynamics within those geometric configurations. In perspective, the system (33) may be integrated with elastic terms dependent on the deformation through global coefficients that could be calibrated to additional measurements [17]. Finally, the model also neglects the influence of chordae tendineae that ensure unidirectional flow by constraining the valve from opening toward the atrium. In this regard, this study did not consider additional effects imputable to the chordae, such as their tethering that may influence MV dynamics in dilated LVs. It also neglects the possible impact of leaflets with surrounding tissues, that are simply anticipated by limiting the allowed configurations.

As discussed in the introduction, a complete FSI approach is the only methodology for ensuring complete reproduction of the dynamics for both fluid and solid phases [45, 70, 59, 63, 43, 109, 11]. On the other hand, the development of FSI in living biological systems presents exceptional difficulties in the definition of tissue properties, including constitutive equation and elastic parameters which may be space-varying and non-isotropic [92, 18, 64], that cannot be easily estimated in vivo. In general, in the perspective of a clinical application, we are left with a dichotomy between simplified approximated models, that may agree with limited measurable information but may not be generally valid, and complete FSI models based on an approximation

of the effective set of tissue parameters that may not be realistic for the specific case under analysis. Aware of these limited options, the present model follows the first route introducing a clinical imaging-based approach, with the objective of providing one additional possible approach.

12. Conclusion

This study presented a numerical approach to the LV fluid dynamics that includes the interaction with MV leaflets. The method is designed for integration with medical imaging in compliance with the accuracy of information effectively available in clinical applications. This model of valvular dynamics corresponds to an asymptotic description of leaflet motion when information about tissue properties are not available or cannot be extrapolated. It represents an improvement with respect to using valveless orifice and provides a more realistic reproduction of the flow below the valve. This numerical study provides some insights into the fluid dynamics of mitral valve regurgitations. The calculation employed a simplified model of MV deformation, based on clinical images, which was found to be appropriate for flow modeling purposes. The analysis has been performed for different prolapsed MVs inserted in both a normal and a dilated LV. First, the study evidenced the presence of a false regurgitation made of blood that was in the MV cup and returned the atrium during MV closure. In small prolapses, this false volume can be comparable to the real regurgitation and should be considered in clinical measurements. The amount of regurgitation is principally due to the effective insufficiency of the MV without a significant influence of the geometry of the LV. The amount of regurgitating volume, expressed in percentage of the stroke volume, is found to be an equivalent measure of the effective orifice area, expressed in percentage of the MV area. The dimensions of the LV enter into play in terms of the quality of the regurgitant blood; larger LVs present a reduced wash-out that reflects in a larger percentage of old blood returning to the atrium, thus increasing the risk of blood aggregation and thrombus. This non-invasive method is useful for the assessment of blood flow, to improve early detection of cardiac dysfunctions and for provide a concrete helpful in clinical routines.

References

[1] Adams, D.H. & Anyanwu, A.C., Rahmanian P.B. & Filsoufi F. 2006 Current concepts in mitral valve repair for degenerative disease. *Heart Fail. Rev.* **11**, 241-257.

[2] Adams, D.H. & Rosenhek, R. & Falk V. 2010 Degenerative mitral valve regurgitation: Best practice revolution. *European Heart Journal* **31**, 1958–1966.

[3] Alfieri, O., Maisano, F., De Bonis, M., Stefano P.L., Torracca, L., Oppizzi, M. & La Canna G. 2011 The double-orifice technique in mitral valve repair: a simple solution for complex problems. *J. Thorac. Cardiovasc. Surg.* **122**, (4):674-81.

[4] Andres-Delgado, L. & Mercader, N. 2016 Interplay between cardiac function and heart development. *Biochim. Biophys. Acta - Mol. Cell Res.* **1863**, 1707–1716.

[5] Anyanwu, A.C., Adams, DH. 2007 Etiologic classification of degenerative mitral valve disease: Barlow's disease and fibroelastic deficiency. *Sem Thorac Cardiovasc Surg.***6**, 19-90.

[6] Arvidsson, P.M., Töger, J., Carlsson, M., Steding-Ehrenborg, K. Pedrizzetti, G., Heiberg, E. & Arheden, H. 2016b Left and right ventricular hemodynamic forces in healthy volunteers and elite athletes assessed with 4D flow magnetic resonance imaging. *Am. J. Physiol. – Hear. Circ. Physiol.*

[7] Baccani, B., Domenichini, F. & Pedrizzetti, G. 2003 Model and influence of mitral valve opening during the left ventricular filling. *J. Biomech.* **36**, 355–361.

[8] Baumgartner, H., Falk, V. & Bax, JJ. 2017 ESC/EACTS Guidelines for the management of valvular heart disease. *Eur Heart J.* **38**, 2739–91.

[9] Bellhouse, B.J. 1972 Fluid mechanics of a model mitral valve and left Ventricle. *Cardiovasc. Res.* **6**, 199-210.

[10] Berdajs, D., Zund, G., Camenisch, C. 2007 Annulus fibrosus of the mitral valve: reality or myth. *J Cardiac Surg***9**, 11-406.

[11] Boilevin-Kayl, L., Fernández, M.A. & Gerbeau, J.F. 2018 Numerical methods for immersed FSI with thin-walled structures. *Computers and Fluids*, DOI:10.1016/j.compfluid.2018.05.024.

[12] Borger, MA. 2006 Chronic ischemic mitral regurgitation: insights into pandora's box. *Circulation.* **6**, 126:2674.

[13] Borger, MA., Murphy, PM., Alam, A. 2006 Initial results of the chordal-cutting operation for ischemic mitral regurgitation. *J Thorac Cardiovasc Surg.* **92**, 133:1483.

[14] Braun, J., van de Veire, NR., Klautz, RJ. 2008 Restrictive mitral annuloplasty cures ischemic mitral regurgitation and heart failure. *Ann Thorac Surg* **6**, 85-430.

[15] Carpentier, A. 1983 Cardiac valve surgery–the "French correction". *J Thorac Cardiovasc Surg.*

[16] Carpentier, AC., Adams, DH., Filsoufi, F. 2010 Carpentier's reconstructive valve surgery. *Maryland Heights: Saunders Elsevier.*

[17] Celotto, C., Zovatto, L., Collia, D. & Pedrizzetti, G. 2019 Influence of mitral valve elasticity on flow development in the left ventricle. *Eur. J. Mech. B/Fluids***75**, 110–118.

[18] Chen, L., Yin, F.C. & May-Newman, K. 2004 The structure and mechanical properties of the mitral valve leaflet-strut chordae transition zone. *J. Biomech. Eng.* **126**, 244–251.

[19] Cimino, S., Pedrizzetti, G., Tont, G., Canali, E., Petronilli, V., De Luca, L., Iacoboni, C. & Agati, L. 2012 In vivo analysis of intraventricular fluid dynamics in healthy hearts. *Eur. J. Mech. B/Fluids* **46**, 35–40.

[20] Cobey, F.C., Ferreira, R., Ursprung, W.W., Karhausen, J., Swaminathan, M., Mackensen, G.B. 2017 A Novel Approach to Assess the Three-Dimensional Anatomy of a Mitral Valve Regurgitant Jet Orifice. *Eur J Cardiothorac Surg.*

[21] Colli, A., Bizzotto, E., Bizzotto, D., Gerosa, G. 2017 Beating heart mitral valve repair with neochordae implantation: real-time monitoring of haemodynamic recovery. *Eur J Cardiothorac Surg.* **2**, 52:991.

[22] Colli, A., Adams, DH., Fiocco, A., Pradegan, N., Longinotti, L., Nadali, M., Pandis, D., Gerosa, G. 2018 Transapical NeoChord mitral valve repair. *Annals of cardiothoracic surgery.* **7**, 812:820.

[23] Collia, D., Vukicevic, M.,Meschini, V.,Zovatto, L. & Pedrizzetti, G. 2019 Simplified mitral valve modelingfor prospective clinical application of left ventricular fluid dynamics. *Journal of Computational Physics* **398**, 108895.

[24] Collia, D., Zovatto, L. & Pedrizzetti, G. 2019 Analysis of Mitral Valve Regurgitation by Computational Fluid Dynamics. *APL Bioengineering* **3**, 036105.

[25] Culver, J.C. & Dickinson, M.E. 2010 The effects of hemodynamic force on embryonic development. *Microcirculation* **17**, 164–178.

[26] Daimon, M., Fukuda, S., Adams, DH. 2006 Mitral valve repair with Carpentier-Mccarthy-Adams IMR Etlogix annuloplasty ring for ischemic mitral regurgitation: early echocardiographic results from a multi-center study. *Circulation.* **114**, (Suppl 1):I588–93.

[27] Dal Ferro, M., Stolfo, D., De Paris, V., Lesizza, R., korcova, R., Collia, D., Tonti, G., Sinagra, G. & Pedrizzetti, G. 2018 Cardiac fluid dynamics meets deformation imaging. *Cardiovascular Ultrasound* **16:4**.

[28] Dal Ferro, M., De Paris, V., Collia, D., Stolfo, D., Caiffa, T., Brabati, G., Korcova, R., Pinamonti, B., Zovatto, L., Zecchin, M. & Pedrizzetti, G. 2019 Left Ventricular Response to Cardiac Resynchronization Therapy: Insights From Hemodynamic Forces Computed by Speckle Tracking. *Frontiers in Cardiovascular Medicine.*

[29] De Tullio, M.D. & Pascazio, G. 2016 A moving least-squares immersed boundary method for simulating fluid-structure interaction of elastic bodies with arbitrary thickness. *J. Comp. Phys.* **235**, 201–225.

[30] Domenichini, F. 2008 On the consistency of the direct forcing method in the fractional step solution of the navier-stokes equations. *J. Comput. Phys.* **227**, 6372–6384.

[31] Domenichini, F. & Pedrizzetti, G. 2015 Asymptotic model of fluid–tissue interaction for mitral valve dynamics. *Cardiovasc. Eng. Technol.* **6**.

[32] Domenichini, F. & Pedrizzetti, G. 2016 Hemodynamic forces in a model left ventricle. *Phys. Rev. Fluids* **1**, 83201.

[33] Ebbers, T., wigstorm, L., Bolger, A.F., Engvall, J. & Karlsson, M. 2001 Estimation of relative cardiovascular pressures using time-resolved three-dimensional phase contrast MRI. *Magn. Reson. Med.* **879**, 45–872.

[34] El Oakley, R. & Shah, A. 2011 Management-Oriented Classification of Mitral Valve Regurgitation. *ISRN Cardiology* **858714**, 6.

[35] Enriquez-Sarano, M., Seward, J.B., Bailey, K.R., Tajik, A.J. 2001 Effective regurgitant orifice area: A noninvasive Doppler development of an old hemodynamic concept. *J. Am. Coll. Cardiol.* **94**, 0735-1097.

[36] Enriquez-Sarano, M., Akins, C.W. & Vahanian, A. 2009 Mitral regurgitation. *The Lancet* **373**, (9672):1382-94.

[37] Eriksson, J., Bolger, A.F., Ebbers, T. & Carlhall, C.J. 2013 Four-dimensional blood flow-specific markers of LV dysfunction in dilated cardiomyopathy. *EHJ Cardiovasc. Imaging.* **14**, 417-424.

[38] Eriksson, J., Zajac, J., Alehagen, U., Bolger, A.F., Ebbers, T. & Carlhall, C.J. 2017 Left ventricular hemodynamic forces as a marker of mechanical dyssynchrony in heart failure patients with left bundle branch block. *Sci. Rep.* **7**, 2971.

[39] Eriksson, J., Dyverfeldt, P., Engvall, J., Bolger, A.F.,Ebbers, T. & Carlhall, C.-J. 2010 Quantification of presystolic blood flow organization and energetics in the human left ventricle. *AJP Hear. Circ. Physiol.*

[40] Eriksson, J., Carlhall, C.-J., Dyverfeldt, P., Engvall, J., Bolger, A.F. & Ebbers, T. 2010 Semi-automatic quantification of 4D left ventricular blood flow. *J. Cardiovasc Magn. Res.* **12**, 9.

[41] Freed, L.A., Levy, D., Levine, R.A., Larson, M.G.,Evans, J.C.,Fuller, D.L.,Lehman, B. & Benjamin, E.J 1999 Prevalence and Clinical Outcome of Mitral-Valve Prolapse. *N. Engl. J. Med.*.

[42] Filsoufi, F., Castillo, JG., Rahmanian, PB. 2007 Remodeling annuloplasty using a prosthetic ring designed for correcting type-iiib ischemic mitral regurgitation. *Rev Esp Cardiol.* **8**, 60-1151.

[43] Gao, H., Femnga, L., Qi, N., Berry, C., Griffith, B.E. & Luo, X. 2017 A coupled mitral valve-left ventricle model with fluid-structure interaction *Medical Engineering and Physics* **47**, 128–130.

[44] Garcia, D., Alamo, J.C., Tanne, D., Yotti, R., Cortina, C., Bertrand, E., Antoranz, J.C., Perez-david, E., Rieu, R., Fernández-avilés, F. & Bermejo, J. 2010 Two-dimensional intraventricular flow mapping by digital processing conventional color-doppler echocardiography images. *IEEE Trans. Med. Imaging* **29**, 1701–1713.

[45] Gilmanov, A., Le, T.B. & Sotiropoulos, F. 2015 A numerical approach for simulating fluid structure interaction of flexible thin shells undergoing arbitrarily large deformations in complex domains. *J. Comput. Phys.* **300**, 814–843.

[46] Grayburn, P.A., Fehske, W., Omran, H., Brickner, M.E. & Luderitz, B. 2007 Multiplane transesophageal echocardiographic assessment of mitral regurgitation by Doppler color flow mapping of the vena contracta. *Am. J. Cardiol.* **74**, (9):912-7.

[47] Gresho, P.M. & Sani, L. 1987 On pressure boundary conditions for the incompressible Navier–Stokes equations. *Int. J. Numer. Methods Fluids* **7**, 1111–1145.

[48] Grigioni, F., Detaint, D., Avierinos, JF. 2007 Contribution of ischemic mitral regurgitation to congestive heart failure after myocardial infarction. *J Am Coll Cardiol.***7**, 45-260.

[49] Gorman, J.H., Gupta, K.B., Streicher, J.T. 1996 Dynamic three-dimensional imaging of the mitral valve and left ventricle by rapid sonomicrometry array localization. *J Thorac Cardiovasc Surg***26**, 112-712.

[50] Ha, J., Oh, J., Redfield, M., Ujino, K., Seward, J. & Tajik, A. 2004 Triphasic mitral inflow velocity with middiastolic filling: clinical implications and associated echocardiographic findings. *J. Am. Soc. Echocardiogr.* **17**, 428–431.

[51] Habash, F., Vallurupalli, S. 2017 Challenges in management of left ventricular thrombus. *doi:10.1177/1753944717711139*.

[52] Harfi, T.T., hee Seo, J., Yasir, H.S., Welsh, N., Mayer, S.A., Abraham, T.P., George, R.T. & Mittal, R. 2016 The E-wave propagation index (EPI): A novel echocardiographic parameter for prediction of left ventricular thrombus. Derivation from computational fluid dynamic modeling and validation on human subjects. *Int. J. Cardiol.*.

[53] Henry, W.L., Griffith, J.M., Michaelis, L.L., McIntosh, C.L., Morrow, A.G. & Epstein, S.E. 1996 Measurement of mitral orifice area in patients with mitral valve disease by real time, two dimensional echocardiography. *Circulation.*

[54] Hong, G.R., Pedrizzetti, G., Tonti, G., Li, P., Wei, Z., Kim, J.K., Baweja, A., Liu, S., Chung, N., Houle, H., Narula, J. & Vannan, M.A. 2008 Characterization and quantification of vortex flow in the human left ventricle by contrast echocardiography using vector particle image velocimetry. *JACC Cardiovasc. Imaging.* **1**, 705–717.

[55] Hove, J.R., Köster, R.W., Forouhar, A.S., Acevedo-Bolton, G., Fraser, S.E. & Gharib, M. 2003 Intracardiac fluid forces are an essential epigenetic factor for embryonic cardiogenesis. *Nature* **421**, 172–177.

[56] Iung, B., Vahanian, A. 2009 Rheumatic mitral valve disease. In: Otto CM, Bonow RO, editors. Valvular heart disease *3rd ed. Philadelphia: Saunders Elsevier.* 221-42.

[57] Iwakura, K., Ito, H., Kawano, S., Okamura, A., Kurotobi, T., Date, M., Inoue, K. & Fujii, K. 2006 Comparison of Orifice Area by Transthoracic Three-Dimensional Doppler Echocardiography Versus Proximal Isovelocity Surface Area (PISA) Method for Assessment of Mitral Regurgitation. *Am. J. Cardiol.*.

[58] Kheradvar, A., Houle, H., Pedrizzetti, G., Tonti, G., Belcik, T., Ashraf, M., Lindner, J.R., Gharib, M. & Sahn, D. 2010 Echocardiographic particle image velocimetry: A novel technique for quantification of left ventricular blood vorticity pattern. *J. Am. Soc. Echocardiogr.* **23**, 86–94.

[59] Kunzelman, K.S., Einstein, D.R. & Cochran, R.P. 2007 Fluid-structure interaction models of the mitral valve: function in normal and pathological states. *Philos. Trans. Roy. Soc. B* **362**, 1393–1406.

[60] Lam, C., Han, L., Ha, J., Oh, J. & Ling, L. 2005 The mitral L wave: a marker of pseudonormal filling and predictor of heart failure in patients with left ventricular hypertrophy. *J. Am. Soc. Echocardiogr.* **18**, 336–341.

[61] Lamas, GA., Mitchell, GF., Flaker, GC. 2007 Clinical significance of mitral regurgitation after acute myocardial infarction. Survival and Ventricular Enlargement Investigators. *Circulation.***33**, 96-827.

[62] Lang, R.M., Adams, D.H. 2009 3D Echocardiographic quantification in functional mitral regurgitation. *JACC Cardiovasc Imaging.* 5:346–7.

[63] Lau, K.D., Diaz, V., Scambler, P. & Burriesci, G. 2010 Mitral valve dynamics in structural and fluid-structure interaction models. *Med. Eng. Phys.* **32**, 1057–1064.

[64] Lee, C.H., Amini, R., Gorman, S.C., Gorman III, J.H. & Sacks, M.S. 2014 An inverse modeling approach for stress estimation in mitral valve anterior leaflet valvuloplasty for in-vivo valvular biomaterial assessment. *J. Biomech.* **47**, 2055–2063.

[65] Lee, C.S.F. & Talbot, L. 1979 A fluidmechanical study of the closure of heart valves. *J. Fluid Mech.* **91**, 41–63.

[66] Levine, R.A., Handschumacher, M.D., Sanfilippo, A.J. 1989 Three-dimensional echocardiographic reconstruction of the mitral valve, with implications for the diagnosis of mitral valve prolapse. *Circulation***98**, 80-589.

[67] Mangual, J.O., Domenichini, F. & Pedrizzetti, G. 2012 Three dimensional numerical assessment of the right ventricular flow using 4d echocardiography boundary data. *Eur. J. Mech. B/Fluids* **35**, 25–30.

[68] Mangual, J.O., Kraigher-Krainer, E., De Luca, A., Toncelli, L., Shah, A., Solomon, S., Galanti, G., Domenichini, F. & Pedrizzetti, G. 2013 Comparative numerical study on left ventricular fluid dynamics after dilated cardiomyopathy. *J. Biomech.* **46**, 1611–1617.

[69] Markl, M., Kilner, P.J. & Ebbers, T. 2011 Comprehensive 4d velocity mapping of the heart and great vessels by cardiovascular magnetic resonance. *J. Cardiovasc. Magn. Reson.* **13**, 7.

[70] Meschini, V., De Tullio, M.D., Querzoli, G. & Verzicco, R. 2018 Effects of natural and prosthetic mitral valves on the flow structure in healthy and pathological left ventricles. *J. Fluid Mech.* **834**, 271–307.

[71] Mittal, R., Dong, H., Bozkurttas, M., Najjar, F.M., Vargas, A. & von Loebbecke, A. 2008 A versatile sharp interface immersed boundary method for incompressible flows with complex boundaries. *J. Comput. Phys.* **227**, 4825–4852.

[72] Mittal, R. & Iaccarino, G. 2005 Immersed boundary methods. *Annu. Rev. Fluid Mech.* **37**, 239–261.

[73] Mittal, R., Seo, J.H., Vedula, V., Choi, Y.J., Liu, H., Huang, H.H., Jain, S., Younes, L., Abraham, T. & George, R.T. 2016 Computational modeling of cardiac hemodynamics: Current status and future outlook. *J. Comput. Phys.* **305**, 1065–1082.

[74] Moore, M., Chen, J., Mallow, P.J. & Rizzo, J.A. 2016 The direct health-care burden of valvular heart disease: Evidence from US national survey data. *Clin. Outcomes Res.*.

[75] Moraldo, M., Cecaro, F., Shun-Shin, M., Pabari, P.A., Davies, J.E., Xu, X.Y., Hughes, A.D., Manisty, C. & Francis, D.P. 2013 Evidence-based recommendations for PISA measurements in mitral regurgitation: Systematic review, clinical and in-vitro study. *doi:10.1111/j.1399-3054.1992.tb04685.x*.

[76] Munoz, D.R., Markl, M., Mur, J.L.M., Barker, A., Fernández-Golfín, C., Lancellotti, P. & Gómez, J.L.Z. 2013 Intracardiac flow visualization: Current status and future directions. *Eur. Heart J. Cardiovasc. Imaging* **14**, 1029–1038.

[77] Nagueh, S.F., Smiseth, O.A., Appleton, C.P., Byrd, B.F., Dokainish, H., Edvardsen, T., Flachskampf, F.A., Gillebert, T.C., Klein, A.L., Lancellotti, P., Marino, P., Oh, J.K., Popescu, B.A. & Waggoner, A,D. 2013 Recommendations for the Evaluation of Left Ventricular Diastolic Function by Echocardiography: An Update from the American Society of Echocardiography

and the European Association of Cardiovascular Imaging. *J. Am. Soc. Echocardiogr.* **29**, 277–314.

[78] Nkomo, V.T., Gardin, J.M., Skelton T.N., Gottdiener J.S., Scott C.G. & Enriquez-Sarano, M. 2006 Burden of valvular heart diseases: a population-based study. *The Lancet* **368**, (9540):1005-11.

[79] Oh, J.K., Park, S.J. & Nagueh, S.F. 2011 Established and Novel Clinical Applications of Diastolic Function Assessment by Echocardiography. *Circ. Cardiovasc. Imaging* **4**, 444–455.

[80] Pasipoularides, A. 2015 Mechanotransduction mechanisms for intraventricular diastolic vortex forces and myocardial deformations: Part 2. *J. Cardiovasc. Transl. Res.* **8**, 293–318.

[81] Pedrizzetti, G. 2015 Kinematic characterization of valvular opening. *Phys. Rev. Lett.* **94**, 1–4.

[82] Pedrizzetti, G., Arvidsson, P.M., Toger, J., Borgquist, R., Domenichini, F., Arheden, H. & Heiberg, E. 2017 On estimating intraventricular hemodynamic forces from endocardial dynamics: A comparative study with 4D Flow MRI. *J. Biomech.* **60**, 203–210.

[83] Pedrizzetti, G. & Domenichini, F. 2007 Asymmetric opening of a simple bileaflet valve. *Phys. Rev. Lett.* **98**, 1–4.

[84] Pedrizzetti, G. & Domenichini, F. 2006 Flow-driven opening of a valvular leaflet. *J. Fluid Mech.* **569**, 321.

[85] Pedrizzetti, G. & Domenichini, F. 2015 Left ventricular fluid mechanics: The long way from theoretical models to clinical applications. *Ann. Biomed. Eng.* **43**, 26–40.

[86] Pedrizzetti, G. & Domenichini, F. 2007 Nature Optimizes the Swirling Flow in the Human Left Ventricle. *Phys. Rev. Lett.* **95**, 108101.

[87] Pedrizzetti, G., La Canna, G., Alfieri, O. & Tonti, G. 2014 The vortex - an early predictor of cardiovascular outcome? *Nat. Rev. Cardiol.* **11**.

[88] Pedrizzetti, G., Martiniello, A.R., Bianchi, V., D'Onofrio, A., Caso, P. & Tonti, G. 2016 Changes in electrical activation

modify the orientation of left ventricular flow momentum: Novel observations using echocardiographic particle image velocimetry. *Eur. Heart J. Cardiovasc. Imaging* **17**, 203–209.

[89] Peskin, C.S. 1972 Flow patterns around heart valves: A numerical method. *J. Comput. Phys.* **10**, 252–271.

[90] Peskin, C.S. 2002 The immersed boundary method. *Acta Numer.* **11**, 479–517.

[91] Peskin, C.S. & McQueen, D.M. 1989 A three-dimensional computational method for blood flowin the heart i. immersed elastic fibers in a viscous incompressible fluid. *J. Comput. Phys.* **81**, 372–405.

[92] Pham, T. & Sun, W. 2014 Material Properties of Aged Human Mitral Valve Leaflets. *J. Biomed. Mater. Res. A.* **102**, 2692-2703.

[93] Poelma, C., Mari, J.M., Foin, N., Tang, M.X., Krams, R., Caro, C.G., Weinberg, P.D. & Westerweel, J. 2011 3d flow reconstruction using ultrasound piv. *Exp. Fluids* **50**, 777–785.

[94] Reul, H., Talukder, N. & Mueller, E.W. 1981 Fluid Mechanics of the Natural Mitral Valve. *J. Biomechanics* **14**, 361-372.

[95] Rushmer, R.F. & Sun, W. 2014 Initial Ventricular Impulse. A potential key to cardiac evaluation. *Circulation* 1964, **29**, 268-283.

[96] Schwammenthal, E., Chen, C., Benning, F., Block, M., Breithardt, G. & Levin, R.A. 1994 Dynamics of mitral regurgitant flow and orifice area. Physiologic application of the proximal flow convergence method: clinical data and experimental testing. *Circulation* **90**, (1):307-22.

[97] Seeburger, J., Rinaldi, M. & Nielsen, SL. 2014 Off-pump transapical implantation of artificial neo-chordae to correct mitral regurgitation: the TACT Trial (Transapical Artificial Chordae Tendinae) proof of concept. *J Am Coll Cardiol.* **9**, 63:914.

[98] Sengupta, P.P., Pedrizzetti, G., Kilner, P.J., Kheradvar, A., Ebbers, T., Tonti, G., Fraser, A.G. & Narula, J. 2012 Emerging trends in cv flow visualization. *JACC Cardiovasc. Imaging* **5**, 305–316.

[99] Seo, J.H., Abd, T., George, R.T. & Mittal, R. 2016 A coupled chemo-fluidic computational model for thrombogenesis in infarcted left ventricles. *Am. J. Physiol. - Hear. Circ. Physiol.* **310**, H1567–H1582.

[100] Seo, J.H., Vedula, V., Abraham, T., Lardo, A.C., Dawoud, F., Luo, H., & Mittal, R. 2014 Effect of the mitral valve on diastolic flow patterns effect of the mitral valve on diastolic flow patterns. *Phys. Fluids* **26**, 121901.

[101] Sherrid, M.V., Kushner, J., Yang, G. & Ro, R. 2014 Mitral valve coaptation and its relationship to late diastolic flow: A color Doppler and vector flow map echocardiographic study in normal subjects. *Echocardiography* **34**, 537-548.

[102] Steer, AC., Carapetis, JR. 2009 Prevention and treatment of rheumatic heart disease in the developing world. *Nature Rev Cardiol.***98**, 6-689.

[103] Thavendiranathan, P., Phelan, P.D., Collier, P., Thomas, J.D., Flamm, S.D. & Marwick, T.H. 2012 Quantitative assessment of mitral regurgitation: How best to do it. *doi:10.1016/j.jcmg.2012.07.013*.

[104] Toger, J., Arvidsson, P.M., Kanski, M., Steding-Ehrenborg, K., Pedrizzetti, G., Carlsson, M., Arheden, H. & Heiberg, E. 2016 Intracardiac hemodynamic forces using 4d flow: A new reproducible method applied to healthy controls, elite athletes and heart failure patients. *J. Cardiovasc. Magn. Reson.* **18**, 1–3.

[105] Tribouilloy, C., Shen, W.F., Quere, J.P., Rey, J.L., Choquet, D., Dufosse, H. & Lesbre, J.P. 1992 Assessment of severity of mitral regurgitation by measuring regurgitant jet width at its origin with transesophageal Doppler color flow imaging. *Circulation***85**, (4):1248-5.

[106] van der Geest, R.J. 2016 Advanced Analysis Techniques for Intracardiac Flow Evaluation from 4D Flow MRI. *Curr. Radiol. Rep.***4**, 38.

[107] Vukicevic, M., Mosadegh, B., Min, J.K. & Little, S.H. 2017a Cardiac 3d printing and its future directions. *JACC Cardiovasc. Imaging* **10**, 171–184.

[108] Vukicevic, M., Puperi, D.S., Grande-Allen, K.J. & Little, S.H. 2017b 3d printed modeling of the mitral valve for catheter-based structural interventions. *Ann. Biomed. Eng.* **45**, 508–519.

[109] Xu, F., Morganti, S., Zakerzadeh, R., Kamensky, D., Auricchio, F., Reali, A., Hughes, T., Sacks, M. & Hsu, M. 2018 A framework for designing patient-specific bioprosthetic heart valves using immersogeometric fluid–structure interaction analysis. *Int. J. Numer. Methods Biomed. Eng.* **34**, e2938.

[110] Zoghbi, W.A., Adams, D., Bonow, R.O., Enriquez-Sarano, M., Foster, E., Grayburn, P.A., Hahn, R.T., Han, Y., Hung, J., Lang, R.M., Little, S.H., Shah, D.J., Shernan, S., Thavendiranathan, P., Thomas, J.D. & Weissman, N.J. 2017 Recommendations for Noninvasive Evaluation of Native Valvular Regurgitation: A Report from the American Society of Echocardiography Developed in Collaboration with the Society for Cardiovascular Magnetic Resonance. *J. Am. Soc. Echocardiogr.* **30**, (4):303-371.